Effective theories of multimode cavity QED

Roberta Palacino

A thesis submitted for the degree of PhD
at the
University of St Andrews

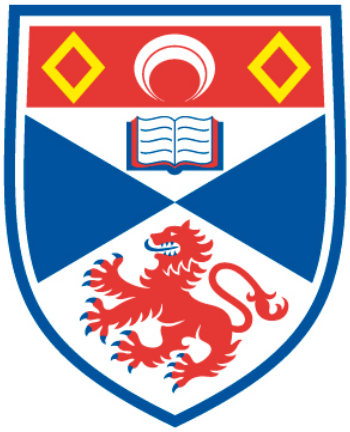

2022

Candidate's declaration

I, Roberta Palacino, do hereby certify that this thesis, submitted for the degree of PhD, which is approximately 31,000 words in length, has been written by me, and that it is the record of work carried out by me, or principally by myself in collaboration with others as acknowledged, and that it has not been submitted in any previous application for any degree. I confirm that any appendices included in my thesis contain only material permitted by the 'Assessment of Postgraduate Research Students' policy.

I was admitted as a research student at the University of St Andrews in August 2017.

I received funding from an organisation or institution and have acknowledged the funder(s) in the full text of my thesis.

Date Signature of candidate

14/01/2022

Supervisor's declaration

I hereby certify that the candidate has fulfilled the conditions of the Resolution and Regulations appropriate for the degree of PhD in the University of St Andrews and that the candidate is qualified to submit this thesis in application for that degree. I confirm that any appendices included in the thesis contain only material permitted by the 'Assessment of Postgraduate Research Students' policy.

Date Signature of supervisor

Permission for publication

In submitting this thesis to the University of St Andrews we understand that we are giving permission for it to be made available for use in accordance with the regulations of the University Library for the time being in force, subject to any copyright vested in the work not being affected thereby. We also understand, unless exempt by an award of an embargo as requested below, that the title and the abstract will be published, and that a copy of the work may be made and supplied to any bona fide library or research worker, that this thesis will be electronically accessible for personal or research use and that the library has the right to migrate this thesis into new electronic forms as required to ensure continued access to the thesis.

I, Roberta Palacino, have obtained, or am in the process of obtaining, third-party copyright permissions that are required or have requested the appropriate embargo below.

The following is an agreed request by candidate and supervisor regarding the publication of this thesis:

Printed copy

Embargo on all of print copy for a period of 1 year on the following ground(s):

- Publication would preclude future publication

Supporting statement for printed embargo request

Chapter 4 contains work which we intend to submit to a journal.

Electronic copy

Embargo on all of electronic copy for a period of 1 year on the following ground(s):

- Publication would preclude future publication

Supporting statement for electronic embargo request

Chapter 4 contains work which we intend to submit to a journal.

Title and Abstract

- I agree to the title and abstract being published.

Date
14/01/2022

Signature of candidate

Date

Signature of supervisor

Underpinning Research Data or Digital Outputs

Candidate's declaration

I, Roberta Palacino, understand that by declaring that I have original research data or digital outputs, I should make every effort in meeting the University's and research funders' requirements on the deposit and sharing of research data or research digital outputs.

Date
14/01/2022

Signature of candidate

Permission for publication of underpinning research data or digital outputs

We understand that for any original research data or digital outputs which are deposited, we are giving permission for them to be made available for use in accordance with the requirements of the University and research funders, for the time being in force.

We also understand that the title and the description will be published, and that the underpinning research data or digital outputs will be electronically accessible for use in accordance with the license specified at the point of deposit, unless exempt by award of an embargo as requested below.

The following is an agreed request by candidate and supervisor regarding the publication of underpinning research data or digital outputs:

Embargo on all of electronic files for a period of 1 year on the following ground(s):

- Publication would preclude future publication

Supporting statement for embargo request

Chapter 4 contains work which we intend to submit to a journal.

Date
14/01/2022

Signature of candidate

Date

Signature of supervisor

Contents

Abstract

This thesis focuses on methods for the derivation of effective theories in models describing cold atoms in optical cavities. Among those models, the Dicke model and its generalisations are among the most representative and studied problems in quantum electrodynamics. It describes the coupling of matter in the form of two-level atoms to a quantised mode of light. The Dicke model has been realised in various physical platforms, such as N-V centers in diamond, molecules coupled to an optical mode, trapped ions, as well as in superconducting qubits coupled to microwave resonators. Extensions of the Dicke model have also been widely used in modelling exciton-polariton condensation with organic molecules. Another realisation involves laser-driven atoms coupled to light in a dissipative cavity. This thesis will focus on the latter type of physical system. When the coupling between light and matter reaches a critical point, the Dicke model predicts a phase transition to a superradiant state. Moreover, the onset of the superradiant phase transition coincides with the breaking of the discrete $\mathbb{Z}_2$ symmetry in the model.

Motivated by experimental advances in the field, there has been a growing interest in the realisation and analysis of generalised Dicke models such as those with continuous symmetry. In these models, the symmetry breaking phase transition is expected to allow for the observation of Goldstone modes. In order for the cavity QED system to be described by a Dicke model with continuous symmetry, one has to consider multimode extensions of the well characterised single mode experiments. Another extension made possible by multimode cavities is associative memory models, where cavity modes mediate interactions between ensembles of atoms.

In many body cavity QED models, the Hilbert space dimension grows according to the number of atoms and modes involved, therefore, solving and fully characterising these problems becomes a challenging task. This is why one has to move to effective descriptions in terms of a reduced number of degrees of freedom. The most widely used technique is

Redfield theory, an equation of motion describing the dynamics of the slowest part of the system, after elimination of the fast component. In our atom-cavity picture, the slow and fast components of the total system will be the atoms and the cavity light, respectively. There are cases where Redfield theory is inadequate to accurately capture dynamics and critical behavior. Given the approximations leading to the Redfield equation, this could be considered as the second order of a perturbative expansion in the light-matter coupling. By adopting a diagrammatic method, one could write a Redfield theory beyond its standard second order formula. In this thesis, these techniques will be employed to analyse a two-mode Dicke model with U(1) symmetry and a model of associative memory.

Chapter 1

Introduction to collective effects in Cavity QED

The Dicke model is a paradigmatic model in cavity quantum electrodynamics (cavity QED), describing the interaction of an ensemble of two-level atoms with a single quantised electromagnetic mode in a cavity. Such a concept developed from the seminal work by Robert Dicke [1] where he assumed N quantum emitters coupled to the electromagnetic field in its vacuum state and described the behavior of the light radiated by these initially excited emitters. If the cloud is localised within a fraction of the wavelength of light they interact with, the emission process will be the result of a constructive interference, leading to an amplitude of the emitted field which scales as the number of atoms N and accordingly, to an intensity scaling as N^2. Such a coherent behavior is known as *Superradiance* [1, 2].

In 1973, other works [3, 4, 5, 6] investigated the atomic ensemble coupled to the quantised mode of a cavity, unveiling another type of superradiant behavior and demonstrating that the Dicke model shows a phase transition from the normal state, where the number of photons is a non-extensive quantity, to the superradiant state of the system, where the number of photons becomes an extensive quantity, scaling with N, in the thermodynamic limit of a large number of atoms.

For several years since its prediction, the superradiant phase transition has remained experimentally elusive. There is still an open debate whether this missed observation involves a "no-go theorem" [7, 8, 9, 10, 11, 12, 13] inhibiting the transition but, even if not forbidden, it is challenging to observe due to the technical limits in reaching stronger

coupling strengths, needed in making the transition observable.
In recent times, theoretical and experimental methods to circumvent the no-go theorem have been brought to attention. One of them was proposed by Dimer and co-workers [14]: a scheme based on multi-level atoms and cavity-mediated Raman transitions reproducing an effective Dicke model. Another experimentally realised by Baumann and collaborators [15] exploits the self-organization process of atomic ensembles in an optical cavity. Both methods will be discussed in more detail in the following sections but we could start to note their common feature: the driven-dissipative nature of such systems.
As we will see, this non-equilibrium phase transition is controlled by the external manipulation of the light source which controls the effective coupling strength between atoms and photons, overcoming the no-go theorem and making the transition observable. In addition, because of the open-system nature of the cavity, dissipation must be taken into account and the combined effect of driving and losses makes the model an effective non-equilibrium Dicke system, as it will be discussed in the following.
The present chapter intends to provide a general background regarding the self-organization process of cold atoms in optical cavities, addressing the issue of continuous and discrete symmetry breaking in the model, associated to the emergence of such ordered phases. This discussion will pave the way for investigating the same questions and matter-light behaviors arisen in single-mode cavities but implementing cavities able to support many modes of the electromagnetic field.
The rest of this chapter will be organised as follows. Firstly I will review the single mode Dicke model, superradiance, and its experimental realization in sections 1.1 – 1.3. I will then discuss two extensions of this. First, to a two-mode model showing U(1) symmetry; this will be introduced and discussed in section 1.4. Secondly, to a multimode Dicke model, in section 1.5. The background discussed in this chapter, along with the methods reviewed in chapter 2, will serve as a basis for the original research themes addressed in chapter 3 and 4.

1.1 Dicke model and the superradiant phase transition

Let us begin by discussing the Dicke model and the mean field limit of the equations of motion of the cavity field and atomic ensemble which, as we will see, allow to obtain the collective mode spectrum depending on the atom-photon coupling rate g and observing

the evolution of the spectrum with increasing values of g will reveal the onset of the superradiant transition.

As mentioned above, a set of N two-level atoms interacts cooperatively with a bosonic mode of the cavity and this concept is encoded in the following Hamiltonian scheme [16]

$$H = \omega_c a^\dagger a + \omega_0 \sum_{i=1}^{N} \left(s_i^z + \frac{2g}{\sqrt{N}} \left(a + a^\dagger \right) s_i^x \right) \tag{1.1}$$

a and $a^\dagger$ are annihilation and creation operators of the bosonic mode, respectively, and s_i^α, with $\alpha = x, y, z$ spin operators related to the Pauli matrices by $s_i^\alpha = \sigma_i^\alpha/2$. ω_c, ω_0 and g are parameters that can be manipulated and correspond to cavity, atomic frequencies, and atom-field coupling constant respectively. The model displays a discrete symmetry under the transformation $a \to -a$ and $s^x \to -s^x$ leaving the Hamiltonian unaltered. This is commonly referred to as $\mathbb{Z}_2$ symmetry and it is associated to the conservation of the parity of the total number of excitations in the system [16]. In addition, in the absence of atomic losses or dephasing, the individual spin degrees of freedom can be replaced by the following operators $S^\alpha = \sum_{i=1}^{N} s_i^\alpha$ [16, 17] which yields

$$H = \omega_c a^\dagger a + \omega_0 S^z + \frac{2g}{\sqrt{N}} \left(a + a^\dagger \right) S^x. \tag{1.2}$$

Noting that Eq.(1.2) and the total spin operator S commute, with $\mathbf{S}^2 = S_x^2 + S_y^2 + S_z^2$, the atomic dynamics under the above Hamiltonian is restricted to a manifold of states $|SM\rangle$ identified by the same total spin S. Given a number N of atoms in the ensemble, $S = N/2$ and the magnetic moment M can span in the range $-S \leq M \leq S$. With this picture, the effective Hilbert space dimension of the atoms is reduced from 2^N to $N + 1$ states. However, this property breaks down when decay processes at single-atom level are included in the model. This reduction in the size of Hilbert space will reveal to be highly useful when computing the eigenspectrum assiociated with the atom-only dynamics for large atom numbers, as we will discuss in a later chapter.

Before entering an out-of-equilibrium context, let us briefly review the method to characterise the superradiant transition at equilibrium.

To localise the critical atom-photon coupling, which defines the boundary between the

normal and the superradiant state, we may start by assuming the cavity field to be in a coherent state so that, $\langle a \rangle = \alpha$, with α complex-valued number. This assumption corresponds to a mean field approximation. Each atom interacts with the cavity field according to the Hamiltonian

$$H(\alpha) = H_c(\alpha) + H_{ac}(\alpha) = \omega_c |\alpha|^2 + \sum_i \left(\omega_0 s_i^z + \frac{4g}{\sqrt{N}} \alpha s_i^x \right) \tag{1.3}$$

where $H_c(\alpha)$ describes the energy of the field and $H_{ac}(\alpha)$ refers to the two remaining terms. As for such a model, when the partition function $Z(\alpha)$ is evaluated

$$Z(\alpha) = \mathrm{Tr}\left[e^{-\beta H} \right] = e^{-\beta \omega_c |\alpha|^2} \left(\mathrm{Tr}\left[e^{-\beta H_{ac}(\alpha)} \right] \right)^N \tag{1.4}$$

one may compute the thermodynamic variables from Eq.(1.4) and its derivatives. One of these state variables is the free energy, defined by

$$F(\alpha) = -\frac{1}{\beta} \ln\left(Z(\alpha) \right) = \omega_c |\alpha|^2 - \frac{N}{\beta} \ln\left(2 \cosh \beta E \right) \tag{1.5}$$

where $\beta = 1/k_B T$ and diagonalisation of $H_{ac}(\alpha)$ yields $E = \sqrt{\frac{\omega_0^2}{4} + \frac{4g^2}{N} |\alpha|^2}$. The critical coupling g_c can be obtained by minimising the free energy with respect to an order parameter of the model, such as the mean value of the cavity field α, finding that for $g < g_c$ the free energy has a single minimum and the order parameter has a vanishing value, as depicted in Fig.(1.1)a). This configuration is associated with the normal phase of the Dicke model. Instead, when $g > g_c$ the energy landscape exhibits two minima, as shown in Fig.(1.1)b). The system thus undergoes a transition which spontaneously breaks the $\mathbb{Z}_2$ symmetry by choosing one of the two possible states corresponding to one of two values for the phase of the light emitted by the cavity. This configuration is the superradiant state of the model. The value g_c at which the instability occurs is given by the point where the derivative $dF(\alpha)/d\alpha$ calculated at $\alpha = 0$ changes sign:

$$g_c = \frac{1}{2} \sqrt{\omega_c \omega_0 \coth\left(\frac{\beta \omega_0}{2} \right)} \xrightarrow{\beta \to \infty} \sqrt{\omega_c \omega_0}/2 \tag{1.6}$$

where the arrow indicates the zero temperature limit of the coupling constant.

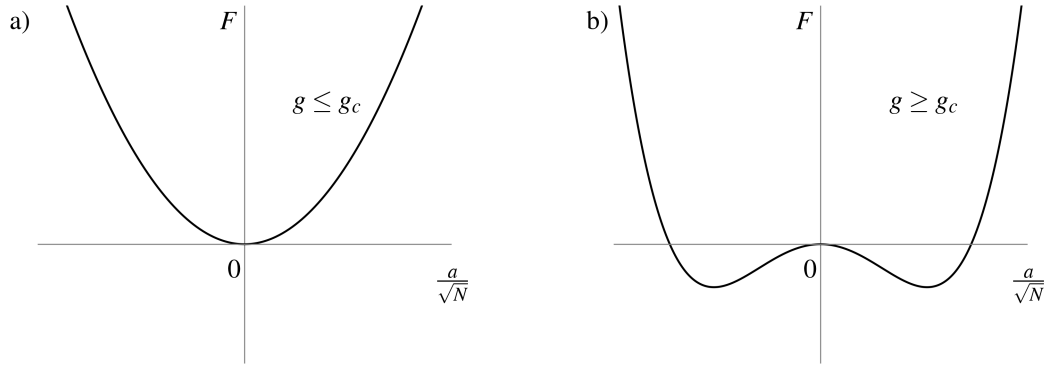

Fig. 1.1. Energy landscape as a function of the order parameter, here the cavity field amplitude, in the normal a) and superradiant phase b) of the $\mathbb{Z}_2$ Dicke model.

We may now consider the Dicke model from an open quantum system perspective by accounting for driving and dissipation and compute the threshold for the onset of the transition. The dynamics of the open system is governed by the Master equation [18, 19]:

$$\dot{\rho} = -i\,[H, \rho] + \kappa \mathcal{D}\,[a] \tag{1.7}$$

where the state evolves in time under the combined effect of unitary dynamics, represented by the commutator with the Hamiltonian Eq.(1.2), and dissipation, encoded by the superoperator $\mathcal{D}$. The latter is often referred to as the dissipator and it acts on a general operator x giving $\mathcal{D}\,[x] = 2x\rho x^\dagger - x^\dagger x\rho - \rho x^\dagger x$. We could in principle include other dissipative processes in the density matrix equation of motion such as single-spin decay and dephasing, treated in previous works [20, 21, 22] but let us consider only the cavity decay rate, as indicated by eq.(1.7). The critical value of atom-light coupling at which the superradiant transition occurs, is found by writing semiclassical equations of motion for the classical cavity field $\alpha = \langle a \rangle = Tr(\rho a)$ and spin components $S^{\pm,z} = \langle S^{\pm,z} \rangle = Tr(\rho S^{\pm,z})$ within a mean field treatment. The mean-field approximation consists in the factorization of higher order correlations into products of single-operator expectation values, $\langle ABC \rangle = \langle A \rangle \langle B \rangle \langle C \rangle$, when the number of atoms involved approaches the thermodynamic limit. Indeed, the number of atoms per ensemble usually employed in such experiments can exceed 10^5 atoms and the mean-field predictions have showed to be in satisfying agreement with the experimental results [15, 23]. Equations (1.2) and (1.7) are therefore

used to obtain the following dynamics of the joint atom-field system

$$\dot{\alpha} = -\left(i\omega_c + \kappa\right)\alpha - \frac{ig}{\sqrt{N}}\left(S^+ + S^-\right) \tag{1.8}$$

$$\dot{S^-} = -i\omega_0 S^- + \frac{2g}{\sqrt{N}}\left(\alpha + \alpha^*\right) S^z \tag{1.9}$$

$$\dot{S^z} = -\frac{ig}{\sqrt{N}}\left(\alpha + \alpha^*\right)\left(S^+ - S^-\right) \tag{1.10}$$

where the aforementioned mean-field decoupling rule is applied. To gain information about the stability of the solutions predicted by this model, the usual procedure consists in perturbing the classical expectations, i.e. writing $\alpha = \alpha^0 + \delta\alpha$, $S^- = S^{0-} + \delta S^-$ and $S^z = S^{0z} + \delta S^z$, with X^0 steady state solutions of the equations of motion and δX small fluctuations, parametrised as follows

$$\begin{aligned} \delta\alpha &= a e^{-i\eta t} + b^* e^{i\eta^* t} \\ \delta S^- &= c e^{-i\eta t} + d^* e^{i\eta^* t} \\ \delta S^z &= f e^{-i\eta t} + f^* e^{i\eta^* t} \end{aligned} \tag{1.11}$$

where $\{a, b, c, d, f, \eta\} \in \mathbb{C}$. As defined in Eq.(1.11), the sign of imaginary part of the complex parameter η determines whether the fluctuation grows/decays while spanning g. In particular, a negative imaginary part indicates a decaying perturbation, thus a stable stationary state. Once substituted the perturbed variables into equations (1.8-1.10), this provides a set of eigenvalue equations in η. In the normal state $\alpha = S^{\pm} = 0$, $S^z = -N/2$, the equation for f decouples and the 4×4 matrix, written using the vector $u = (a, b, c, d)^T$,

is

$$M-\eta I=\begin{pmatrix} \omega_c-i\kappa-\eta & 0 & -\frac{g}{\sqrt{N}} & -\frac{g}{\sqrt{N}} \\ 0 & -\omega_c-i\kappa+\eta & -\frac{g}{\sqrt{N}} & -\frac{g}{\sqrt{N}} \\ -ig\sqrt{N} & -ig\sqrt{N} & \omega_0-\eta & 0 \\ -ig\sqrt{N} & -ig\sqrt{N} & 0 & -\omega_0-\eta \end{pmatrix} \tag{1.12}$$

where I is the identity matrix. For $g < g_c$, the steady state $\alpha = S^{\pm} = 0$, $S^z = -N/2$ is stable. It becomes unstable once overcome the critical coupling strength $g > g_c$ where the superradiant state, corresponding to the steady state solutions of eqs.(1.8-1.10), now is stable. The threshold g_c indicating the phase transition is found by requiring that at least one of the eigenvalues of M vanishes. This condition marks the boundary between stability and instability. The critical value of the matter-light coupling rate is thus given by [16]

$$g_c=\frac{1}{2}\sqrt{\omega_0\frac{\omega_c^2+\kappa^2}{\omega_c}} \tag{1.13}$$

which for negligible cavity decay becomes $g_c = \sqrt{\omega_0\omega_c}/2$, recovering the result for the Dicke model at equilibrium. The method adopted here could be applied to analyse linear stability in effective Dicke models describing the interaction of a large number of spin ensembles with an equally high number of cavity modes. As we discuss in a later section of this chapter, the dimension of the linear system and, accordingly of the eigenvalue problem, scales with both the number of atomic and cavity degrees of freedom, introducing a key question to which the present thesis work will attempt to answer.

For what concerns the experimental realizations, the Dicke model has been realised in various physical platforms, such as N-V centers in diamond [24, 25, 26], molecules [27] coupled to an optical mode, trapped ions [28, 29], as well as in superconducting qubits coupled to microwave resonators [10, 12, 30, 31, 32, 33, 34]. Extensions of the Dicke model have also been widely used in modelling exciton-polariton condensation with organic molecules [35]. Another realisation involves laser-driven atoms coupled to light in a dissipative cavity. We will consider the latter category and discuss the types of atomic ordering, accompanying the superradiant phase transition, that occur in the atomic

ensembles confined in the cavity, which can be either magnetic, in the case of spin systems, or spatial, in the case of the motional states of a Bose-Einstein condensate [36, 37].

1.2 Self-organisation in Bose-Einstein Condensate

Dynamical versions of the Dicke model and its underlying superradiant transition deeply depend on the balanced interplay between energy-gain processes and dissipative effects. In such a framework, we now discuss one of the two techniques employed to realise this paradigmatic model and the phase transition that it describes.

To this aim, let us start by describing the physical system: a cloud of effective two-level ($|e\rangle, |g\rangle$) bosonic atoms are exposed to a coherent laser field, detuned from both the atomic transition ω_a and the cavity ω_c resonances, in the transverse direction to the cavity axis and interact with a single cavity electromagnetic field. The laser beam with Rabi frequency $\Omega_p(\mathbf{r}) = \Omega_0 \cos(k_c y)$ (Ω_0 being the maximum Rabi frequency and $k_c = 2\pi/\lambda_c$ the wave number depending on the wavelength of the cavity field) is reflected by a mirror back on the cloud and interferes with the standing wave of the electromagnetic field in the cavity, as shown in Fig.(1.2). The atom-photon interaction strength is expressed by $g(\mathbf{r}) = g \cos(k_c x)$ ($\mathcal{G}(\mathbf{r})$ in Fig.(1.2) where g_0 is the single atom-light coupling constant. The energy of this coupled light-matter system is encoded in the following Hamiltonian ($\hbar = 1$) [38]:

$$
\begin{aligned}
H = &-\Delta_c a^\dagger a + \sum_{\tau=g,e} \int \psi_\tau^\dagger(\mathbf{r}) \left[\frac{\mathbf{p}^2}{2m} + \mathrm{V_{ext}}(\mathbf{r}) \right] \psi_\tau(\mathbf{r}) d\mathbf{r} - \Delta_a \int \psi_e^\dagger(\mathbf{r}) \psi_e(\mathbf{r}) d\mathbf{r} + \\
&\int \left\{ \psi_e^\dagger(\mathbf{r}) \left[\Omega_p(\mathbf{r}) + g(\mathbf{r}) a \right] \psi_g(\mathbf{r}) + \mathrm{H.c.} \right\} d\mathbf{r} + H_{\mathrm{int}}, \\
H_{\mathrm{int}} = &\frac{1}{2} \sum_{\tau=g,e} g_{\tau\tau} \int \psi_\tau^\dagger(\mathbf{r}) \psi_\tau^\dagger(\mathbf{r}) \psi_\tau(\mathbf{r}) \psi_\tau(\mathbf{r}) d\mathbf{r} + g_{eg} \int \psi_e^\dagger(\mathbf{r}) \psi_g^\dagger(\mathbf{r}) \psi_g(\mathbf{r}) \psi_e(\mathbf{r}) d\mathbf{r}
\end{aligned}
\tag{1.14}
$$

In the above equation, $\Delta_c = \omega_p - \omega_c$ and $\Delta_a = \omega_p - \omega_a$ are the difference in frequency between the pump (p) and the cavity (c) and atomic (a) resonances. $\psi_\tau(\mathbf{r}) = \psi_\tau(\mathbf{r}, t)$ and $a = a(t)$ are the annhilitaion operators acting on the atoms and the cavity field mode, respectively. In addition to their kinetic energy, the atoms are subject to a trapping potential

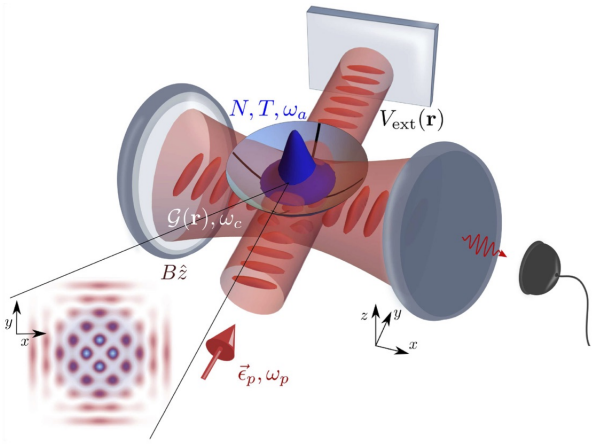

Fig. 1.2. Sketch of a typical cavity QED setup. A cloud of N atoms at temperature T is trapped by an external potential, $V_{\text{ext}}(\mathbf{r})$, and transverse illuminated by a coherent laser field (red arrow) with polarisation ϵ_p and frequency ω_p, detuned from the atomic frequency ω_a. This interferes with the standing wave field of a cavity mode (light red) which dissipate energy at a rate κ (red wiggly arrow). The coupling strength between the cloud and the electromagnetic field is encoded by the space-dependent $\mathcal{G}(\mathbf{r})$. Reprinted figure with permission from Ref. [39]. Copyright (2021) by Taylor&Francis Online (Website).

$\mathrm{V}_{\text{ext}}(\mathbf{r})$ and the interaction term describes two-body contact interactions [40], with $g_{gg} = g_0, g_{ee}, g_{ge} = g_{eg}$ associated coupling strengths. The configurations adopted in cavity QED experiments typically consist in far detuning the laser and cavity frequency from the electronic transition of the atoms so that the excited state is marginally populated, with the benefit of a strong suppression of spontaneous emission. With such an approximation one can eliminate the evolution of the excited state, and the dynamics of the system is reduced to the following pair of coupled Heisenberg equations for the atomic ground state and the cavity field amplitude [39]:

$$\begin{aligned}
\dot{\psi}_g(\mathbf{r},t) &= -i\left[\frac{\mathbf{p}^2}{2m} + \mathrm{V}_{\text{ext}}(\mathbf{r}) + \mathrm{V}(\mathbf{r}) + \mathrm{U}(\mathbf{r})a^\dagger a + \eta(\mathbf{r})(a^\dagger + a) + g_0 n(\mathbf{r})\right]\psi_g(\mathbf{r},t) \\
\dot{a} &= i\left(\Delta_c - \int \mathrm{U}(\mathbf{r})n(\mathbf{r})d(\mathbf{r}) + i\kappa\right)a - i\int \eta(\mathbf{r})n(\mathbf{r})d(\mathbf{r}) - i\xi
\end{aligned} \tag{1.15}$$

where $n(\mathbf{r}) = \psi_g^\dagger(\mathbf{r})\psi_g(\mathbf{r})$. In addition to the trapping term, $V_{\text{ext}}(\mathbf{r})$, the atoms experience the lattice potential generated by the laser $\mathrm{V}(\mathbf{r}) = \mathrm{V}_0\cos^2(k_c y)$, where $\mathrm{V}_0 = \Omega_0^2/\Delta_a$ defines the depth of the potential, and the term $\mathrm{U}(\mathbf{r}) = \mathrm{U}_0\cos^2(k_c x)$, along the cavity

axis, whose depth is given by $U_0 = g_0^2/\Delta_a$. Thus, upon switching the laser beam on, the ensemble starts to absorb laser photons; these are scattered in the cavity thus creating photons in the resonator, as described by the term $U(\mathbf{r})a^\dagger a$, and then scattered again by other atoms in the ensemble either into the cavity or into the pump, with this process due to the term $\eta(\mathbf{r})(a^\dagger + a)$. Therefore, as a consequence of the increasing pump intensity, these two atom-mediated electromagnetic fields generate a λ_c-periodic checkerboard pattern, encoded by the spatial function $\eta(\mathbf{r}) = \eta_0 \cos(k_c x)\cos(k_c y)$, with $\eta_0 = g_0\Omega_0/\Delta_a$, where atoms arrange in either the minima or the maxima of the pattern, according to the type of laser detuning being set. This phenomenon is known as density-modulated atomic self-ordering and it is favored by the interplay of energy gain and dissipation. As already discussed, the former originates from the laser beam while the latter is due to the imperfect cavity mirrors, and is taken into account in Eq.(1.15) through the cavity loss rate κ. The last term in the equation of the field describes a stochastic force with zero average $\langle \xi(t) \rangle = 0$ and delta-correlated in time, $\langle \xi(t)\xi(t') \rangle = 2\kappa\delta(t - t')$.
The intrinsic open system nature, already captured in the Heisenberg picture by Eq.(1.15), is also represented by the density matrix equation of motion for the atom-plus-field system in the Schroedinger picture:

$$\begin{aligned} &\dot{\rho} = -i[H, \rho] + \mathcal{D}[a]\rho \\ &H = \int \psi_g^\dagger \left[\frac{\mathbf{p}^2}{2m} + V_{\text{ext}}(\mathbf{r}) + V(\mathbf{r}) + U(\mathbf{r})a^\dagger a + \eta(\mathbf{r})(a^\dagger + a) + g_0 n(\mathbf{r}) \right] \psi_g d\mathbf{r} - \Delta_c a^\dagger a \end{aligned} \tag{1.16}$$

As the cavity field naturally evolves on a faster timescale than that of the atoms, any change in the atomic distribution determines a rapid adjustment of the field configuration. The cavity field thus adiabatically follows the atomic behavior. Exploiting this separation in timescales, one could find the stationary state from the second equation in Eq.(1.15) and substitute the solution in the first equation, thus eliminating the explicit presence of the field from the overall dynamics. This operation yields a density-density modulated interaction term [39]

$$H_{\text{at}} \propto \int \int \mathbf{D}(\mathbf{r}, \mathbf{r}') n(\mathbf{r}) n(\mathbf{r}') d\mathbf{r} d\mathbf{r}', \tag{1.17}$$

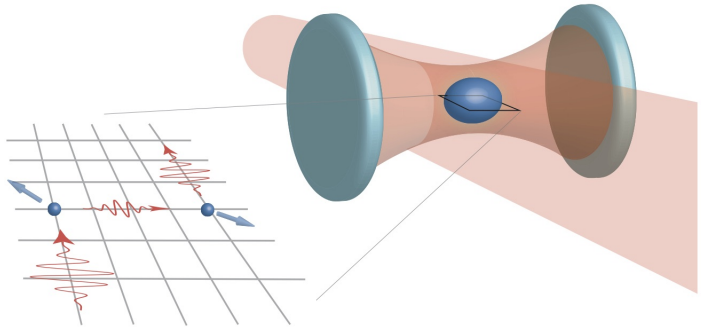

Fig. 1.3. Cavity QED setup to observe atomic selforganisation. An ensemble of atoms (blue sphere) is embedded in the optical potential resulting from the cavity mode structure interfering with the transverse field of the pump. The transverse plane corresponding to the grid on the left represents the interference pattern. Following the directions on the grid, a pump photon (red arrow) is absorbed by a first atom, then emitted in the cavity, absorbed by a second atom and emitted back in the pump beam. In the process, the atoms acquire momentum due to photon scattering, indicated by the blue arrows. Reprinted figure with permission from Ref. [39]. Copyright (2021) by Taylor&Francis Online (Website).

whose strength is given by

$$\mathbf{D}(\mathbf{r},\mathbf{r}') = \frac{2\Delta_c}{|\Delta_c + i\kappa|^2}\eta(\mathbf{r})\eta(\mathbf{r}') = \frac{2\Delta_c g_0^2\Omega_0^2}{\Delta_a^2|\Delta_c + i\kappa|^2}\cos(k_c x)\cos(k_c y)\cos(k_c x')\cos(k_c y') \tag{1.18}$$

To understand the meaning of the above expression, it is useful to adopt the following picture: an atom, located at the point $\mathbf{r}$ inside the resonator, scatters a photon from the pump in the cavity mode. Such a photon is then scattered from the mode to the laser by another atom at position $\mathbf{r}'$. Those atoms thus interact via the electromagnetic field built from the constructive interference of the laser and cavity field, as shown in Fig.(1.3). Therefore, for high enough laser intensity, following this emerging optical interference pattern, initially uncorrelated atoms will leave the homogeneous normal state, characterised by a null average value of the cavity field, and arrange themselves in one of two mutually exclusive checkerboard configurations in the $x-y$ plane, with an interatomic distance set to integers multiple of the wavelength of the light $\lambda_c = 2\pi/k_c$. Such configurations favor a coherent pump-cavity scattering process and the construction of a non-vanishing average field. This atomic self-ordering thus coincides with the onset of superradiance. As it is expressed by the sinusoidal functions in Eq.(1.15), the density-density interaction has a long-range

character and this ensures a homogeneous coupling between all atoms and the radiation field in the resonator.

Now, in order to show how Eq.(1.16) can be connected to the Dicke model, we may express Eq.(1.16) in terms of momentum states. As stated above, the emerging interference pattern determines the periodicity of the atom-atom global interaction being invariant for translations of integer multiples of λ_c along x and y directions. In other words, only those photon-mediated scattering processes leading the atoms to occupy states $\mathbf{k} = (k_x, k_y) = (l, m)k_c$ with $l, m \in \mathbb{Z}$, contribute to constructive interference and superradiant emission. If we express the field operator of the atoms in the momentum basis as,

$$\psi(\mathbf{r}) = \frac{1}{\sqrt{A}} \sum_{l,m\in\mathbb{Z}} e^{ik_c(lx+my)} b_{l,m} \tag{1.19}$$

where $\mathbf{k} = (l, m)k_c$, $\mathbf{r} = (x, y)$, A is the quantization area, and $b_{l,m}$ is a bosonic operator annihilating an atom in the momentum state with components (l, m), then Eq.(1.16) becomes [39]

$$\begin{aligned} H = \sum_{l,m\in\mathbb{Z}} \Bigg[& \omega_r(l^2+m^2) b^\dagger_{l,m} b_{l,m} + \frac{\eta_0}{4}(a^\dagger + a)\left(b^\dagger_{l+1,m+1} b_{l,m} + b^\dagger_{l+1,m-1} b_{l,m} + \text{H.c.}\right) + \\ & \frac{V_0}{4}\left(b^\dagger_{l,m+2} b_{l,m} + \text{H.c.}\right) + \frac{U_0}{4} a^\dagger a \left(b^\dagger_{l+2,m} b_{l,m} + \text{H.c.}\right)\Bigg] - \delta_c a^\dagger a \end{aligned} \tag{1.20}$$

As shown in Fig.(1.3), while scattering a photon from the pump to the cavity, atoms undergo recoil processes at a frequency $\omega_r = k_c^2/2M (\hbar = 1)$ and for large enough pump detuning from higher momentum states, one can restrict the atomic dynamics to the low-energy subspace spanned by the states $\mathbf{k} = (0, 0)$ and $\mathbf{k} = (\pm k_c, \pm k_c)$, as depicted in Fig.(1.4). In this picture, the second term in Eq.(1.20) describes processes where atoms acquire momentum in the $x - y$ directions due to scattering photons either into the cavity or the pump (dynamics due to the emerging checkerboard pattern), while the third and the fourth account for two-photon scattering in the pump (V_0) and cavity (U_0) direction, respectively. The presence of the ensemble determines a shift in the cavity resonance in addition to the pump-mode detuning, specifically $\delta_c = \Delta_c - NU_0/2$. At this point, one can establish relations between such bosonic operators and the collective spin operators in the form of $S^+ = (S^-)^\dagger = \frac{1}{2}\sum_{l,m=\pm1} b^\dagger_{l,m} b_{0,0}$ and $S^z = (\frac{1}{4}\sum_{l,m=\pm1} b^\dagger_{l,m} b_{l,m}) - b^\dagger_{0,0} b_{0,0}$ to

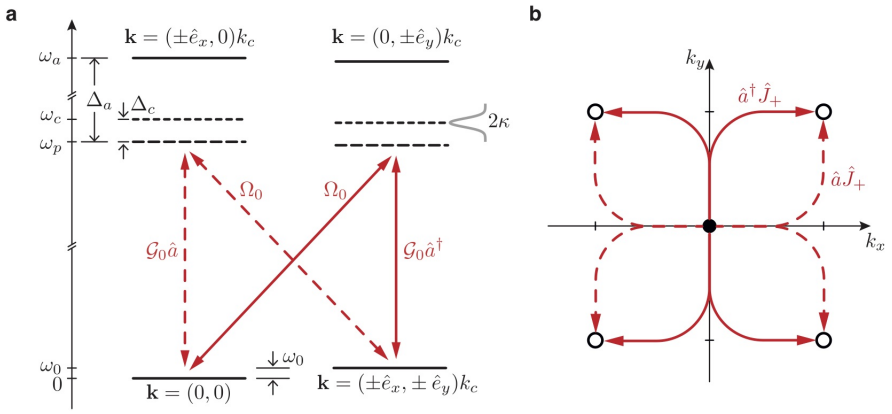

Fig. 1.4. a) Atomic level structure and driving scheme: in this panel, the relevant dynamical scales are provided starting from the low-level spacing $\omega_0 = 2\omega_r$, atomic excited state Δ_a and cavity Δ_c detunings from the laser beam. The solid and dashed red arrows indicate the two possible channels connecting the ground state $\mathbf{k} = (0,0)$ to the excited states $\mathbf{k} = (\pm k_c, \pm k_c)$. b) These channels are reported in a $k_y - k_x$ diagram showing the type of process associated with each path: as an example, an atom scattering a photon from the pump to the cavity leaves the ground state (black dot) to occupy the state (k_c, k_c) (white dot in the first quadrant) by either creating a cavity photon $(a^\dagger J^+)$ or annihilating a cavity photon (aJ^+). Reprinted figure with permission from Ref. [39]. Copyright (2021) by Taylor&Francis Online (Website).

rewrite Eq.(1.20) as

$$H \approx \omega_0 S^z - \delta_c a^\dagger a + \frac{1}{2}\eta_0(a^\dagger + a)(S^+ + S^-) \tag{1.21}$$

In this low-energy picture of the system, the Hamiltonian Eq.(1.21) recovers the form of the $\mathbb{Z}_2$-symmetric Dicke model. Here the two-level particles have a transition frequency given by the photon recoil $\omega_0 = 2\omega_r$, and they are coupled to a single bosonic mode with frequency $-\delta_c$. As given by the critical atom-photon coupling $\eta_{0c}\sqrt{N} = \sqrt{\omega_0(\delta_c^2 + \kappa^2)/-\delta_c}$, the remarkable difference in this case is that the energy spacing between the ground and excited momentum states is of the order of the recoil energy $\hbar\omega_r$, which is smaller than typical optical frequencies, thus lowering the light-matter coupling strength required to reach the self-ordering phase. In other words, according to the original Dicke Hamiltonian, atom-light coupling strengths are compatible with atomic transitions and cavity frequencies (hundreds of THz), while with the Raman driving scheme drawn in Fig.(1.4), the critical coupling shifts to scales compatible with cavity detuning/decay rate and atomic recoil frequency (kHz-MHz). As discussed earlier, the dynamical behaviour of the system

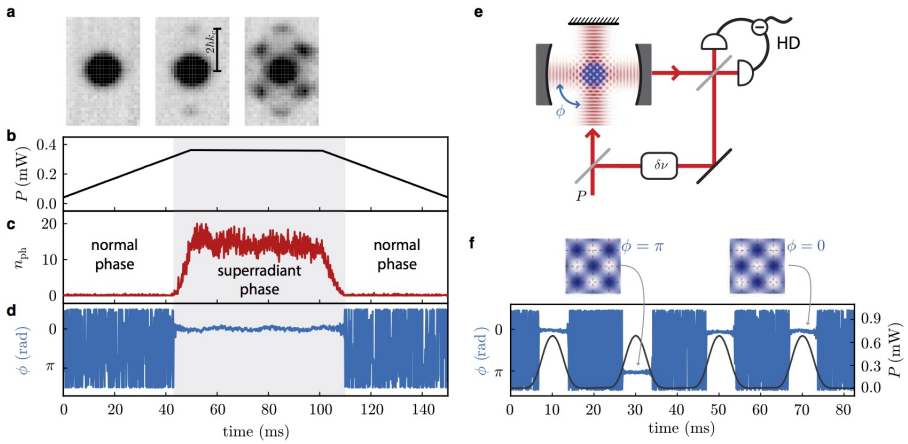

Fig. 1.5. Cavity-QED setup with atoms in a driven BEC undergoing a self-organisation process corresponding to superradiant phase transition. a) Absorption images of the condensate after expansion reveal the momentum states occupied throughout the transition. b) shows how the laser beam power is varied over time while c) and d) show the intensity and the phase of the field. As the pump is increased, the system leaves the normal phase with zero photons recorded and a non-defined phase to enter the superradiant phase with a non-zero intensity and a defined phase. The system is brought back to the normal phase as the power is decreased. e) shows the heterodyne detection scheme measuring amplitude and phase of the field, while f) shows how repeated ramping up processes through threshold reveal how the phase select either 0 or π as consequence of the $\mathbb{Z}_2$ symmetry breaking. Each value corresponds to a different checkerboard pattern. Reprinted figure with permission from Ref. [39]. Copyright (2021) by Taylor&Francis Online (Website). The figure was adapted and reprinted with permission from Ref. [15] published in 2010 by the Nature Publishing Group and Ref. [41] © 2011 by the American Physical Society.

can be seen as a competition between the atomic kinetic energy cost and optical potential arising from pump-to-cavity scattering processes. As the critical atom-photon coupling is reached, the confinement by the attractive optical potential overcomes the free motion of the particles resulting in a regular (λ_c-periodic) arrangement of the atoms which, in turn, favors an optimised intracavity field. The superradiant self-organisation phase transition has been first observed in a Bose-Einstein condensate [15] in a regime of very low temperature compared to dynamical atomic scales, $k_B T \ll \hbar\omega_r$. As described in Fig.(1.5), a pump power P generating the effective light-matter coupling η_0, is injected transversally to the cavity direction and continuously increased. In the normal phase, $P < P_c$, the output light intensity is effectively zero due to pump-cavity scattering processes by the atoms which lead to destructive interference; at the same time the atomic distribution remains homogeneous in the transverse $x - y$ region. When going through the critical power, the output light intensity undergoes a sharp increase: an optical lattice potential arises, as a result of an efficient photon scattering, guiding the particles to locate at definite positions in space. In reciprocal space, this results in a reflected population of momentum states, superposition of the 4 k-states $\mathbf{k} = (\pm k_c, \pm k_c)$, schematically shown in Fig.(1.4), and in the time of flight images in Fig.(1.5). The order parameter used to track the superradiant self-ordered phase transition corresponds to the average value of the checkerboard potential calculated on the atomic density distribution:

$$\Theta = \langle\psi| \cos(k_c x) \cos(k_c y) |\psi\rangle = \frac{1}{\eta_0} \int \eta(\mathbf{r}') n(\mathbf{r}') d\mathbf{r}' \tag{1.22}$$

Such a quantity, in particular its sign, indicates the spatial configuration selected by the atoms: when $\Theta > 0$ ($\Theta < 0$) the sublattice being occupied correspond to the even (odd) sites. In experiments, typical order parameters are the atomic polarisation $\langle S^x \rangle = \langle S^+ + S^- \rangle / 2$ or the photon number operator corresponding to the recorded light intensity outside the cavity $\langle a^\dagger a \rangle$. This twofold spatial arrangement reflects the discrete $\mathbb{Z}_2$ parity symmetry which is broken in the self-organised/superradiant state. Once the phase boundary is reached, the difference in phase between the cavity field and the pump beam is set to one of two mutually exclusive values, either 0 or π, as shown in Fig.(1.5). At the same time, the maximum peaks of the atomic density distribution are found in either the even or the odd sites of the checkerboard lattice potential.

It is noteworthy that the mechanism of symmetry-breaking observed in real experiments is

not spontaneous; usually there are already conditions which are going to favour a specific final configuration. As an example, the overlap of the atomic ensemble with the even or odd sublattice of the arising checkerboard potential could be initially different and this situation helps the system in the selection of the final state. Such a difference causes the presence of a negligible but non-zero field that can induce the symmetry-breaking [41].
Now, to conclude the section, let us briefly see a few works about the spatial self-organization process occuring in BECs. The superradiant phase transition could be accompanied by the emergence of Higgs and Goldstone modes, excitations arising as a result of the breaking of a continuous symmetry, that will be explained in more detail in the next chapter. In [23, 42], such excitations are observed in a BEC of 2×10^5 Rb^{87} atoms off-resonantly driven by a transverse pump lattice and interacting with two optical cavity modes with equal coupling strength. The modification of the effective intra-cavity potential on approaching the critical point of coupling towards the characteristic Mexican hat-shape, as also observed in [32], in the superradiant self-organised phase leads to the two modes. In addition, the authors report the realisation of a system displaying the characteristics of a "supersolid" [23, 42], i.e. a quantum many-body system which upon entering the strong coupling regime, self-organise such that each atom is spatially separated from the others by integer multiple of the wavelength to form a crystalline structure and, at the same time, displaying phase coherence, distinctive of a superfluid.
Other works taking into account the same bimodal configuration predict a novel phase, the vestigial order state, intermediate between the normal and superradiant state. The peculiarity is that although the creation of a density wave occurs at the transition, neither mode manifests superradiance [43]. The vestigial order phase is lower energy than the superradiant phase since it involves momentum exchanges between pump and cavity mode smaller than those occurring in the superradiant state and it is predicted to be more stable in configurations involving a greater number of cavity modes. This fact leads us to enter deeper the multimode regime.

1.3 Self-organisation in spin systems

We have seen that coupling motional states of the atoms to the light field in a cavity QED system realises the superradiance phase transition, predicted by the Dicke model [1, 44]. The works discussed in the previous section, however, neglect the contribution

of the internal dynamics of the atoms, which evolve on a faster timescale compared to the motional degrees of freedom [39]. This aspect will thus be the theme of the present section.

Since the first studies of ultracold atoms in optical lattices, such systems have been proposed as a platform for the exploration of magnetic phenomena because they allow for the exact realisation of theoretical models, such as the Hubbard and Heisenberg models, widely employed in describing the properties of strongly correlated electronic systems [45, 46, 47, 48, 49]. Also, drawing a connection with the spatial self-ordering process involving the atomic motional states, such many-body cavity QED systems have allowed for the prediction and observation of combined density and spin ordering dynamics [50, 51, 52, 53, 54, 55, 56].

However, the Hubbard model simulators are based on short-range interactions between atomic spins, and a possible connection with the Dicke model, involving couplings between the atoms of the "all-to-all" type, is provided by long range cavity-mediated interactions [57]. In Ref. [57], the authors indeed propose a scheme for realizing long-ranged magnetic interactions employing a system of spins in a multimode optical cavity and predicting a phase transition either to a spin glass or to a superradiant state. They show that in the single-cavity mode case, the atomic spins follow a precise ordering within the optical lattice potential, providing a ferromagnetic spin-spin interaction for atoms distant a pump wavelength λ from one another and antiferromagnetic for atoms $\lambda/2$ apart. This spin ordering has something in common with the spatial selforganisation of atoms in Bose-Einstein condensates in the sense that, it leads to a cooperative emission rate into the cavity mode, i.e. superradiance.

While, as seen in the previous section, light-matter interactions induces processes of spatial self-ordering in the atomic BEC that can be mapped to the Dicke superradiance transition, there is still another way to the realisation of an effective Dicke model. Although this approach is also based on a combination of laser and cavity-mediated scattering, it no longer couples motional states but internal levels of the atoms [14], as we now discuss in more detail.

Let us suppose to confine an ensemble of N atoms in an optical resonator and let the atoms couple uniformly with the quantised $\mathrm{TEM}_{0,0}$ mode of this cavity and a pair of external lasers, propagating in the transverse direction to the cavity field. The approximation of uniform coupling might be assumed when the cavity beam waist is broad compared to

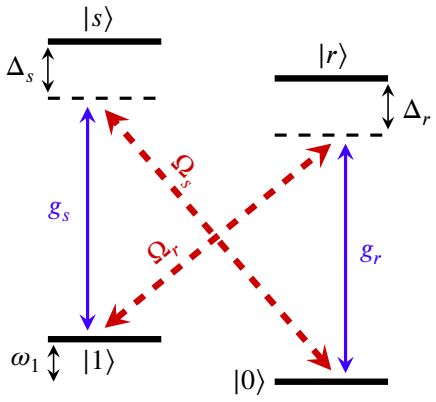

Fig. 1.6. Raman driving scheme: a combination of laser and cavity mediated transitions couples two ground state, $|1\rangle$ and $|0\rangle$, via virtual excited states.

the size of the atomic ensemble. Each emitter can be schematically represented as a 4-level system, as shown in Fig.(1.6), with a pair of low-energy levels, $|0\rangle$ and $|1\rangle$, that are connected via transitions to the excited states, $|s\rangle$ and $|r\rangle$, and scattering processes by the cavity. Specifically, the pump lasers drive crossed transitions $|1\rangle \leftrightarrow |r\rangle$ and $|0\rangle \leftrightarrow |s\rangle$ with associated Rabi frequencies Ω_r and Ω_s and the cavity favours the $|r\rangle \leftrightarrow |0\rangle$ and $|s\rangle \leftrightarrow |1\rangle$ transitions with coupling strengths g_r and g_s respectively. The transitions via excited states are red-detuned by the amount Δr and Δs, in order to reduce the rate of occurrence of spontaneous emission decays by the atoms. From the experimental point of view, the two ground states of Fig.(1.6) can be realised by manipulating the level spectra of alkali-metal atomic species. Specifically, one could for example select the $F = 1$ ground state of Rubidium atoms, and expose the ensemble to properly tuned magnetic fields, thus generating a Zeeman splitting of the $m_F = \pm 1$ magnetic hyperfine levels of the manifold [14]. We now discuss how such multilevel system can be reduced to an effective 2-level system, as it is typical of the Dicke model. To this purpose, it is useful to formalise the various components in the system dynamics. The evolution of the open atom-cavity system is governed by the density matrix equation of motion ($\hbar = 1$):

$$\dot{\rho} = -i[H, \rho] + \kappa \mathcal{D}[a] + \gamma \mathcal{D}[S^-] \tag{1.23}$$

where the Hamiltonian describes the cavity, atom and interaction dynamics, $H = H_{\text{cav}} +$

$H_{\rm at} + H_{\rm int}$, according to

$$\begin{aligned} H_{\rm cav} &= \omega_{\rm c} a^\dagger a \\ H_{\rm at} &= \sum_{j=1}^{N} \left\{ \omega_r |r_j\rangle\langle r_j| + \omega_s |s_j\rangle\langle s_j| + \omega_1 |1_j\rangle\langle 1_j| + H_{\rm drive} \right\} \\ H_{\rm int} &= \sum_{j=1}^{N} [(g_r |r_j\rangle\langle 0_j| a + g_s |s_j\rangle\langle 1_j| a) e^{ikx_j} + \text{H.c.}] \end{aligned} \tag{1.24}$$

where $H_{\rm drive} = (\Omega_r/2) e^{-i\omega_{lr} t} |r_j\rangle\langle 1_j| e^{ik_r x_j} + (\Omega_s/2) e^{-i\omega_{ls} t} |s_j\rangle\langle 0_j| e^{ik_s x_j} + \text{H.c.}$. As for Eq.(1.24), being externally driven, each atom is embedded in the travelling wave along x at position x_j and it can populate the levels $1, r, s, 0$ with energies $\omega_1, \omega_r, \omega_s, 0$, respectively. The two laser sources at frequencies ω_{lr}, ω_{ls} and wavenumbers k_r, k_s, thus guide transitions indicated by the projection operators in $H_{\rm drive}$, while interactions with the quantised cavity mode a, characterised by the coupling strength g_r, g_s, induce the atom to populate either the ground states (with the creation of a cavity photon) or the excited r, s states (with the annihilation of a cavity photon). Eq.(1.23) accounts also for cavity losses, as given by the Lindblad dissipator $\mathcal{D}[a] = 2a\rho a^\dagger - \left\{ a^\dagger a, \rho \right\}$ with rate κ and spontaneous emission, captured by the last term in the equation, characterised by the excited state linewidth γ. While energy dissipation by the cavity cannot be avoided, there are conditions where atomic spontaneous emission can be neglected. These conditions are satisfied for large enough laser detunings from the excited state energies. In particular, by defining the unitary transformation $U = e^{-iH_0 t}$, with

$$H_0 = (\omega_{ls} - \omega_1') a^\dagger a + \sum_{j=1}^{N} \left\{ (\omega_{lr} + \omega_1') |r_j\rangle\langle r_j| + \omega_{ls} |s_j\rangle\langle s_j| + \omega_1' |1_j\rangle\langle 1_j| \right\} \tag{1.25}$$

where $\omega_1' = (\omega_{ls} - \omega_{lr})/2 \approx \omega_1$. Then assuming the large detuning limit, i.e $|\Delta_{r,s}| \gg \Omega_{r,s}, g_{r,s}, \kappa, \delta_{\rm cav}, \gamma$, where $\Delta_r = \omega_r - (\omega_{lr} + \omega_1')$, $\Delta_s = \omega_s - \omega_{ls}$, $\delta_{\rm cav} = \omega_{\rm cav} - (\omega_{ls} - \omega_1')$, one can adiabatically eliminate the excited states and reformulate the problem in terms of a 2-level system, composed by the low-energy $|0\rangle$ and $|1\rangle$ states, collectively coupled to

the cavity field, expressed by

$$\begin{aligned}\dot{\rho} &= -i[H,\rho] + \kappa\mathcal{L}_{\text{cav}}\rho \\ H &= \omega a^\dagger a + \omega_0 S^z + \delta a^\dagger a S^z + \frac{\lambda_r}{\sqrt{N}}(aS^+ + \text{h.c}) + \frac{\lambda_s}{\sqrt{N}}(a^\dagger S^+ + \text{h.c}).\end{aligned} \tag{1.26}$$

The collective atomic operators appearing in Eq.(1.26) are defined according to Fig.(1.6) as follows,

$$\begin{aligned}S^+ &= \sum_{j=1}^{N} |1_j\rangle\langle 0_j| \\ S^z &= \frac{1}{2}\sum_{j=1}^{N}(|1_j\rangle\langle 1_j| - |0_j\rangle\langle 0_j|)\end{aligned} \tag{1.27}$$

This reformulation provides expressions of the parameters given by

$$\begin{aligned}\omega &= \frac{1}{2}N(g_r^2/\Delta_r + g_s^2/\Delta_s) + \delta_{\text{cav}} \\ \omega_0 &= \frac{1}{4}(\Omega_r^2/\Delta_r - \Omega_s^2/\Delta_s) + \omega_1 - \omega_1' \\ \delta &= g_r^2/\Delta_r - g_s^2/\Delta_s \\ \lambda_r &= \frac{1}{2}g_r\sqrt{N}\Omega_r/\Delta_r \\ \lambda_s &= \frac{1}{2}g_s\sqrt{N}\Omega_s/\Delta_s\end{aligned} \tag{1.28}$$

By reading Eq.(1.28), the atomic parameters can be externally adjusted by means of the laser frequencies and intensities. In this way, one changes from a picture where the typical transition frequencies lie in the optical region of the spectrum to a new representation where the driving rates and frequencies involved lie in the infrared region. Most importantly, the possibility to fine tune parameters provided by this driving scheme, bypassing transitions via atomic excited states, is a way to avoid spontaneous emission effects. Setting a configuration such as $g_r^2/\Delta_r = g_s^2/\Delta_s, g_r\Omega_r/\Delta_r = g_s\Omega_s/\Delta_s$, modifies Eq.(1.26) so that it converges to the standard Dicke Hamiltonian.

This coupling scheme is key for simulating models with continuous symmetry breaking because it allows to tune and control the two coupling strengths independently. With regard

to this fact, if we consider only one leg of the Raman scheme, for example $|1\rangle \rightarrow |r\rangle$ and $|r\rangle \rightarrow |0\rangle$, this configuration produces the following chain of events: absorption of a pump photon, emission into the cavity mode with atomic relaxation to the $|0\rangle$ state and loss of the photon into the external environment. This process leads to a net transfer of atomic population from the $|1\rangle$ to the $|0\rangle$ state, which in the long time limit, due to lack of photons in the cavity, becomes a dark state for the system. This fact does not allow the realisation of a model displaying U(1) symmetry whose spontaneous breaking gives rise to gapped Higgs and gapless Goldstone modes [42, 32, 58]. With regard to this issue, it is important to note that the Dicke Hamiltonian, while presenting a discrete $\mathbb{Z}_2$ symmetry, does not manifest a continuous U(1) symmetry due to the presence of the counter-rotating terms in the interaction between atomic and field degrees of freedom which cannot be neglected when entering the strong coupling regime, relevant for the phase transition. This obstacle is overcome in [17] which will be discussed in the next section and constitutes the starting point for the extension to a multimode regime.

1.4 Two-mode Dicke models with U(1) symmetry

We have discussed the standard Dicke model and the $\mathbb{Z}_2$ symmetry-breaking phase transition in the context of open quantum systems. We now consider extensions of such a model where atoms couple to two cavity modes [17, 23, 42, 43]. This represents a first step towards a multimode configuration which will be discussed in the next section. Importantly, contexts beyond the single-mode case open the route to the implementation of more complex symmetries such as continuous symmetries. This in turn provides the chance to analyse the spectrum of the dynamics and detect possible Higgs and Goldstone modes associated with the spontaneous symmetry-breaking [42, 32, 58].

In this regard, we begin with reviewing the analysis of a class of generalised two-mode Dicke models with U(1) symmetry, developed in Ref [17], to present results that will be used as a reference for the research project discussed in Chapter 3.

The scenario investigated in [17] involves a set of multi-level atoms confined in a cavity supporting two optical modes and the mutual interaction is depicted in a similar picture as Fig.(1.6) but in this case for a pair of bosonic modes, see Fig.(1.8). The key ingredient to control the continuous symmetry is the possibility to independently control the co and counter-rotating terms in the Hamiltonian model, advantage provided by the Raman

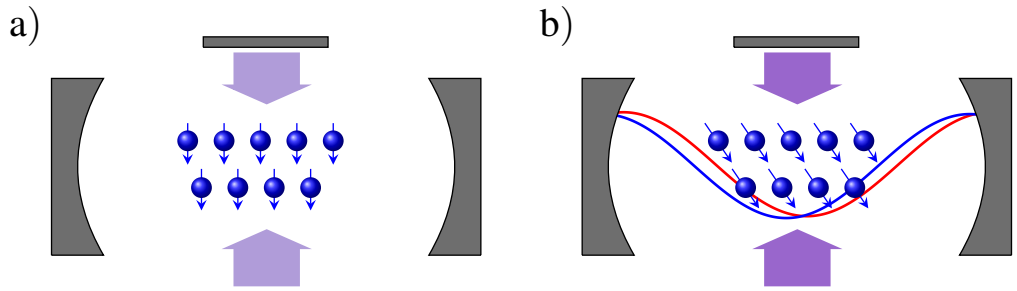

Fig. 1.7. a) Cavity QED setup with atoms exposed to transverse light source at $g < g_c$ (light amethyst) initialised in the normal state $S^z = -N/2, \alpha = \beta = 0$. b) When $g > g_c$ the system undergoes superradiance phase transition spontaneously breaking U(1) symmetry, with atom and field expectations values acquiring a non-zero phase θ, namely $X = X_0 \exp\{\pm i\theta\}$, $X = (\alpha, \beta, S^{\pm})$.

coupling method [14]. While the coupling strength is normally equal between the co-rotating and counter-rotating terms in scenarios involving momentum states of the atoms in a Bose Einstein condensate, this does not need to be the case for hyperfine levels, allowing much more freedom in setting the system's parameters.

The relative strength of the Raman transitions can be externally regulated and monitored by changing the pump strength or the atomic detuning [14].

Let us suppose to have transversally-driven atoms coupled to two optical modes in a cavity, as shown in Fig.(1.7). We suppose all the atoms to be uniformly coupled to the intra-cavity light field and the cavity has losses at rate κ. Being thus subject to energy exchanges with the external environments, the dynamics of the system is regulated by the density matrix equation of motion

$$\dot{\rho} = -i\,[H, \rho] + \frac{\kappa}{2}\left(\mathcal{D}\,[a] + \mathcal{D}\,[b]\right) \tag{1.29}$$

and by the Hamiltonian

$$H = \omega_A a^\dagger a + \omega_B b^\dagger b + \sum_{i=1}^{N}\left\{\omega_0 s_i^z + \left(g_A a^\dagger s_i^- + g_B b^\dagger s_i^- + g'_A a^\dagger s_i^+ + g'_B b^\dagger s_i^+ + \text{h.c}\right)\right\} \tag{1.30}$$

ω_A and ω_B are the mode detunings relative to the pump laser, ω_0 is related to the energy separation between the two atomic internal states, as shown in Fig.(1.6) and $g_{A(B)}$, $g'_{A(B)}$ are respectively co-rotating and counter-rotating coupling constants for each cavity mode.

It is worth recalling that in the absence of any dissipative channel for the spins, such as single atom decay $\Gamma_\downarrow$ and dephasing Γ_ϕ [16, 20], the sum over the individual spin operators can be given in terms of operators $S^\alpha = \sum_{i=1}^{N} s_i^\alpha$ ($\alpha = x, y, z$), introduced previously and describing the collective excitations of the matter component of the system. In such a situation, the dynamics conserves the spin modulus. As mentioned, the values of these four couplings can be in principle distinct and a tailored tuning can provide models with continuous U(1) symmetry. To see this, let us express this symmetry in terms of its generators. According to Noether's theorem, when the Hamiltonian of a physical system has a continuous symmetry property, i.e. the model is invariant upon applying a transformation law, then a conserved quantity must correspond to such symmetry. In other words, when the Hamiltonian is formally the same if transformed according to U_θ, as $U_\theta H U_\theta^\dagger = H$, with $U_\theta = \exp\{i\theta G\}$, for any value of the parameter θ, then H has a continuous symmetry and it respects the condition $[H, G] = 0$, where G is the generator of the symmetry and corresponds to the conserved quantity. To make a connection with our case, we may manipulate the couplings to have $g_B = g'_A = 0$ or $g_A = g'_B = 0$. The Raman scheme realising such a configuration is given in Fig.(1.8). This choice would provide a Hamiltonian with U(1) symmetry where the generator is defined by:

$$G_0 = \left(a^\dagger a - b^\dagger b\right) + S^z \tag{1.31}$$

This corresponds to a transformation of the cavity and spin operators of the type $(a, b, S^\pm) \rightarrow (ae^{i\theta}, be^{-i\theta}, S^\pm e^{\mp i\theta})$. The unitary transformation defined by the generator in Eq.(1.31) would describe the same model when the cavity modes acquire equal and opposite phases. If for example $g_B = g'_A = 0$ and $g_i = g_i^*$, the corresponding expression for the interaction Hamiltonian would then be:

$$H_{int} = g_A a^\dagger S^- + g'_B b^\dagger S^+ + \text{h.c.} \tag{1.32}$$

Another U(1)-symmetric model can be extracted from the generalised Hamiltonian Eq.(1.30) by setting $g_A = g'_A$ and $g_B = -g'_B$, as discussed in previous works [58]. The generator in this case is expressed by

$$G_1 = -i\left(a^\dagger b - b^\dagger a\right) + S^z \tag{1.33}$$

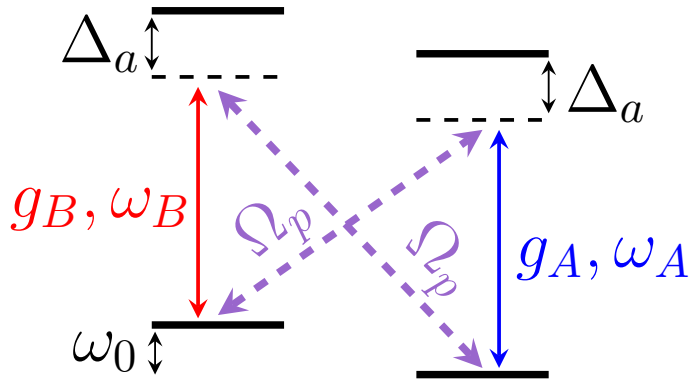

Fig. 1.8. Raman coupling scheme associated with the symmetry generator in E.(1.31).

This leads to an atom-field interaction where each mode couples to a different spin quadrature:

$$H_{int} = g_A \left(a^\dagger + a\right) \left(s_i^+ + s_i^-\right) - g_B \left(b^\dagger - b\right) \left(s_i^+ - s_i^-\right). \tag{1.34}$$

When the ensemble is degenerately coupled to both cavities $g_A = g_B$ and $\omega_A = \omega_B$, the full Hamiltonian manifests a U(1) symmetry under a unitary transformation of both fields and spin quadratures. Eq.(1.33) reveals a different type of U(1) symmetry from the previous case Eq.(1.31): while there the symmetry had a phase character, the present case Eq.(1.33) involves the amplitudes of modes a and b. To see this more clearly, one can equivalently cast the symmetry generator as $G = \Lambda^\dagger M \Lambda$ + spin op. where $\Lambda = (a, b)^T$ is the column vector of the cavity operators and M is a unitary matrix defining the transformation: $\Lambda' = U_\theta \Lambda U_\theta^\dagger = \exp\{i\theta M\}\Lambda$. Therefore, the transformation matrix for the generator Eq.(1.31) is the Pauli matrix σ_z:

$$e^{i\theta\sigma_z} = \begin{pmatrix} e^{-i\theta} & 0 \\ 0 & e^{i\theta} \end{pmatrix} \tag{1.35}$$

while in the case of generator Eq.(1.33), the transformation is the Pauli matrix σ_y

$$e^{i\theta\sigma_y} = \begin{pmatrix} \cos\theta & \sin\theta \\ -\sin\theta & \cos\theta \end{pmatrix} \tag{1.36}$$

For an open system, in addition to the condition $[H, G] = 0$, one should check that the same transformation carrying the symmetry generator U_θ, leaves the master equation unaltered $\rho = U_\theta \rho U_\theta^\dagger$ (a condition on the Lindblad superoperators: $\mathcal{L}[x] = U_\theta \mathcal{L}[x] U_\theta^\dagger$).

The two cases presented above are the extreme limits of a family of U(1) symmetric models whose generator is a combination of G_0 and G_1, expressed by

$$G_\gamma = \cos(2\chi)\left(a^\dagger a - b^\dagger b\right) - i\sin(2\chi)\left(a^\dagger b - b^\dagger a\right) + S^z. \tag{1.37}$$

The condition $[H, G_\gamma] = 0$ is satisfied for the following Hamiltonian [17]

$$H = \omega_A a^\dagger a + \omega_B b^\dagger b + \sum_{i=1}^{N}\left\{\omega_0 s_i^z + g\left(\left[\left(a^\dagger + i\gamma e^{i\psi} b^\dagger\right) s_i^- + \left(b^\dagger + i\gamma e^{-i\psi} a^\dagger\right) s_i^+\right] + \text{h.c}\right)\right\} \tag{1.38}$$

if we choose $\tan(\chi) = \gamma$, where $0 \leq \gamma \leq 1$ is a parameter expressing the ratio between the coupling constants to each cavity mode, $\gamma = g_B/g_A$ (or $\gamma = g'_A/g'_B$). The two extreme values $\gamma = 0, 1$ ($\psi = 0$) corresponds respectively to the generators of eqs.(1.31) and (1.33). These limiting cases are treated in [58, 32]. As discussed later on, while the system described by Eq.(1.31) has U(1) symmetry for $\omega_A \neq \omega_B$, the second scenario Eq.(1.33) requires $\omega_A = \omega_B$ to ensure symmetry.

Now, by means of Eqs.(1.29-1.38), one could derive coupled semiclassical equations of motion for the classical fields of the two modes and atomic spins [17]:

$$\dot{\alpha} = -\left(i\omega_A + \frac{\kappa}{2}\right)\alpha + g\left(\gamma S^+ - iS^-\right) \tag{1.39}$$

$$\dot{\beta} = -\left(i\omega_B + \frac{\kappa}{2}\right)\beta + g\left(\gamma S^- - iS^+\right) \tag{1.40}$$

$$\dot{S}^+ = i\omega_0 S^+ - 2g\left[i\left(\alpha^* + \beta\right) + \gamma\left(\alpha - \beta^*\right)\right] S^z \tag{1.41}$$

$$\dot{S}^z = g\left\{\left[i\left(\alpha^* + \beta\right) + \gamma\left(\alpha - \beta^*\right)\right] S^- + c.c\right\} \tag{1.42}$$

We recall that the field and spin variables appearing in the above dynamical equations are expectation values of the corresponding quantum operators. Moreover we approximate correlation functions of two operators by product of their expectations. This approximation will be discussed in the next chapter. Asking for the steady state solutions (by imposing the derivatives to 0) combined with a direct time-evolution of the equations provides expressions for fixed-points solutions and limit cycles [17]. This system will always admit the normal and inverted states ($\alpha = \beta = S^{\pm} = 0$, $S^z = \mp N/2$) as fixed-point attractors but for sufficiently higher matter-light coupling strength, the system enters the stable superradiant state, see Fig.(1.9). By recalling that the length of collective spin is conserved when no spin dissipation channels are explicitly considered, one may express the spin raising operator as:

$$S^+ = e^{i\theta}\sqrt{N^2/4 - S^{z2}} \tag{1.43}$$

in terms of the spin projection and of the angle θ of the collective spin with the z-axis. The angle is effectively free when $g < g_c$, indicating that the corresponding steady state solutions preserve the U(1) symmetry under rotations around the z-axis. As the system becomes superradiant for $g > g_c$, the phase θ of the spin locks to a well defined value, breaking the symmetry in the ground state. This can be seen if we solve $\dot{S}^+$ for the stationary state, knowing Eq.(1.43) and the steady state values of the fields found from $\dot{\alpha} = 0$ and $\dot{\beta} = 0$ (Eq.(1.42) is automatically satisfied by any solution of Eq.(1.41)). We thus get an equation for S^z:

$$\begin{aligned} S^z = -\frac{\omega_0}{2g^2}\Bigg[(1+\gamma^2)\left(\frac{\omega_A}{\omega_A^2+\kappa^2/4}+\frac{\omega_B}{\omega_B^2+\kappa^2/4}\right)+i\frac{\kappa}{2}(1-\gamma^2)\left(\frac{1}{\omega_B^2+\kappa^2/4}-\frac{1}{\omega_A^2+\kappa^2/4}\right) \\ +i2\gamma e^{-i2\theta}\left(\frac{\omega_B}{\omega_B^2+\kappa^2/4}-\frac{\omega_A}{\omega_A^2+\kappa^2/4}\right)\Bigg]^{-1}. \end{aligned} \tag{1.44}$$

One needs to make sure that Eq.(1.44) is a physical solution, meaning $S^z \in \mathbb{R}$ and $|S^z| < N/2$, therefore constraints are imposed depending on system parameters. We will focus our attention mainly on the case $\gamma = 0$, as the corresponding U(1) model is central for the analysis we will discuss in Chapter 3. When $\gamma = 0$ and for perfect mode degeneracy

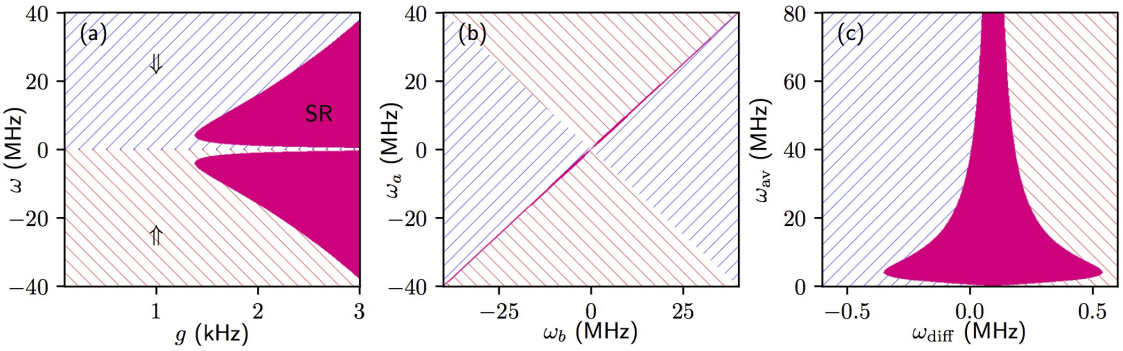

Fig. 1.9. a) $\omega - g$ Phase diagram showing the stability of the steady-states of the system with increasing values of the atom-light coupling rate g for the case $\gamma = 0$, $\omega_A = \omega_B = \omega$. For low values of g, the normal (blue region) and inverted (red region) states are stable, while for higher values of g, the superradiant solution (purple region) becomes stable. b) $\omega_A - \omega_B$ phase diagram showing U(1) symmetry-breaking along the $\omega_A = \omega_B$ line, revealing a finite extension (panel c) in the range of cavity frequencies ($\omega_{av} = (\omega_A + \omega_B)/2$ and $\omega_{diff} = (\omega_A - \omega_B)/2$). Reprinted figure from Ref. [17] with permission from R.I Moodie *et al.*, Phys. Rev. A **97**, 033802, 2018. Copyright (2018) by the American Physical Society.

$\omega_A = \omega_B = \omega$, the solution in Eq.(1.44) is always real:

$$S^z = -\frac{\omega_0}{4g^2}\left(\frac{\omega^2 + \kappa^2/4}{\omega}\right). \tag{1.45}$$

Moreover, as this solution is independent of θ and symmetric, the superradiant transition spontaneously breaks the symmetry by fixing the angle of the collective spin. From Eq.(1.45), one can compute the critical value g_c for the onset of the phase transition: for $S^z > -N/2$, one can find the critical point after which the system enters the symmetry-broken phase,

$$g_c^2 N = \frac{\omega_0}{2}\left(\frac{\omega^2 + \kappa^2/4}{\omega}\right). \tag{1.46}$$

as we have already discussed for the driven-dissipative version of the Dicke model. On the other hand, when $\gamma = 0$ and $\omega_A \neq \omega_B$, the stationary solution Eq.(1.44) is again θ-independent but the presence of an imaginary part, given by the term proportional to $\kappa/2$, breaks the condition of a real S^z solution. This obstacle is overcome by moving to a rotating frame [17]: once entered the symmetry-broken phase, the system would be in

a time-dependent steady state identified by $\alpha = \alpha_0 e^{-i\nu t}$, $\beta = \beta_0 e^{i\nu t}$, $S^+ = S_0^+ e^{i\nu t}$. The system would evolve under the Hamiltonian $H - \nu G_0$, where the unitary transformation relating the original reference frame and the rotating frame is given by $U = \exp\{i\nu G_0 t\}$. This change of picture manifests in a change of the effective frequencies in the equations of motion with $\omega_A \to \omega_A^* = \omega_A - \nu$, $\omega_B \to \omega_B^* = \omega_B + \nu$ and $\omega_0 \to \omega_0^* = \omega_0 - \nu$; therefore the condition required for Eq.(1.44) to be real when the cavity modes are non-degenerate is that $\omega_A^* = \omega_B^*$, alternatively that $\nu = (\omega_A - \omega_B)/2$. Such a requirement on the mode frequencies implies that there exists a finite frequency region where the system undergoes a symmetry-breaking phase transition to a time-dependent superradiant solution, depicted in purple in Fig.(1.9)-c). This feature is unique of the $\gamma = 0$ model. Indeed, in all the other $\gamma \neq 0$ models, U(1) symmetry is guaranteed only when $\omega_A = \omega_B$. In those models, the phase diagram acquires a structured form, made of regions with single-mode superradiance as well as coexisting superradiant phases, and limit cycles [17].
For what follows, we are particularly interested in the $\gamma = 0$ U(1) symmetric model and the results we have just discussed will be our reference frame for verifying the reliability of the atom-only density matrix equation of motion associated with such a model that will be derived and analysed in Chapter 3. Before such a discussion, the last section of this chapter will be dedicated to multimode extensions of the Dicke model, reviewing experimental and theoretical progress in this field.

1.5 Multimode cavity QED

As discussed in the previous section, coupling atoms to more than a single cavity field provides additional features to the phase diagram, particularly allowing for models with more complex symmetries than $\mathbb{Z}_2$ to emerge [59, 42, 23, 17]. Building on what we have discussed so far, we now enter the novel context of light-matter interactions in cavities supporting multiple modes.
Previous theoretical investigation has detailed the self-organization process of BECs in a multimode cavity-QED setting, revealing how the nature of the phase transition changes due to quantum fluctuations [59, 60], and describing the conditions to realise frustration in the dynamics [57]. The remarkable control of the experimental conditions allows one to fine tune the regimes to be investigated, switching from single-mode to multimode configurations by properly adjusting mirrors separations [61]. Moreover, the inclusion of

many electromagnetic modes in the dynamics is key for realising synthetic gauge fields [62], manipulating light-mediated atom-atom interactions [63] and simulating pattern-retrieval in neural networks [64].

To prepare the ground for some of the most relevant works involving cold atoms coupled to multiple electromagnetic modes, it is useful to introduce the main properties of the resonators [65, 66, 67]. As discussed in section 1.2, an optical cavity is typically formed by two facing, highly reflective mirrors of radii of curvature $R^c_{1,2}$ respectively, and the distance between them, l_{res}. With these two quantities, one can define parameters $g_i = 1 - l_{\text{res}}/R^c_i$, with $i = 1, 2$ and $0 \leq g_1 g_2 \leq 1$, that identify the type of cavity. These properties are summarised in Fig.(1.10). As depicted in the right side of the figure, each geometry has an associated frequency spectrum, showing the position of longitudinal modes, identified by the index l that keeps track of the nodes along the cavity axis, and transverse electromagnetic $\text{TEM}_{\text{m,n}}$ modes. These are described by the spatial function:

$$\begin{aligned}\mathcal{E}(\mathbf{r}) =& \mathcal{E}_0 \frac{w_0}{w(x)} H_m\left(\frac{\sqrt{2}y}{w(x)}\right) H_n\left(\frac{\sqrt{2}z}{w(x)}\right) e^{-(y^2+z^2)/w^2(x)} \\ &\times \cos\left[k_c\left(x + \frac{y^2+z^2}{2R(x)}\right) - \varphi^{\text{Guoy}}_{mn}(x) + \varphi^{\text{offset}}_{mn}\right]\end{aligned} \tag{1.47}$$

In the above expression, each transverse mode is identified by a couple of integers m, n that, in the same fashion as l, indicate the numbers of nodes at each direction in the transverse $y - z$ plane. Moreover, the $\text{TEM}_{\text{m,n}}$ is characterised by a frequency, connected to the wave number $k_c = 2\pi/\lambda_c$ and a mode waist $w(x) = w_0\sqrt{1 + (\lambda_c x/\pi w_0^2)^2}$, with w_0 being the beam waist associated with the $\text{TEM}_{0,0}$. $H_{m,n}$ are Hermite-Gaussian functions that determine the mode structure in the transverse plane and $R(x) = x + \pi^2 w_0^4/\lambda_c^2 x$ is how the radius of curvature modifies along the longitudinal axis. The term $\varphi^{\text{Guoy}}_{mn}(x) = (1 + m + n)\arctan(\lambda_c x/\pi w_0^2)$ accounts for an additional phase shift due to the spatially changing radius of curvature $R(x)$ and that becomes relevant for higher transverse modes, while the last term $\varphi^{\text{offset}}_{mn} = (m + n)\arctan(\lambda_c l_{\text{res}}/2\pi w_0^2)$ is included so that Eq.(1.49) respects boundary conditions at the mirrors locations. Regarding the spectral features of the cavity geometries, one finds that, in the limiting case of a planar ($g_1 = g_2 = 1$, $R_i = \infty$) resonator, the transverse modes are organised in well separated and near-degenerate families belonging to a specific longitudinal mode whose frequency separation with the

nearest neighbour indexes ($l \rightarrow l \pm 1$) is equal to the free spectral range $\nu_{FSR} = c/2l_{\text{res}}$, see Fig.(1.10). In contrast, for confocal ($g_1 = g_2 = 0$, $R_i \approx l_{\text{res}}$) or concentric ($g_1 = g_2 = -1$, $R_i \approx l_{\text{res}}/2$) cavities, transverse modes split and concentrate in families with different longitudinal mode index. In particular, in the confocal regime, modes are found in groups labelled by either even or odd $m+n$, and whose separation is set to half of the free spectral range. In general, the frequency of resonances is given by

$$\nu_{lmn} = \nu_{FSR}\left[l + (m+n+1)\frac{\arccos\left(\pm\sqrt{g_1 g_2}\right)}{\pi}\right] \tag{1.48}$$

where the arccos function is obtained by calculating the Guoy phase shift accumulated across the cavity and the ± signs refer to the planar (+) and concentric (−) configurations.

For what concerns the quality of the resonators, this is encoded by the finesse $\mathcal{F} = \pi(\mathcal{R}_1\mathcal{R}_2)^{1/4}/(1-\sqrt{\mathcal{R}_1\mathcal{R}_2})$, where $\mathcal{R}_i$ is the reflectivity of the mirrors. It basically represents the degree of confinement of the field in the volume of space enclosed by the mirrors. Finally, to make a connection with the cavity losses, described in the density matrix equation of motion, and the optical properties just discussed, the cavity decay rate is given by $\kappa = \pi\nu_{FSR}/\mathcal{F}$.

Several experiments have made use of resonators in the planar and confocal regime. While works making use of the former type have been discussed in sections 1.2, some of those involving confocal cavities will be explored here.

Because of their driven-dissipative open system nature, single and few-modes cavity QED, have allowed the observation and characterisation of exotic quantum matter-light phases [23, 42]. Such systems are generally well described within a mean-field framework where contributions due to light-matter quantum correlations are neglected. In contrast, in a multimode regime of a large number of cavity modes, the breakdown of mean field theory occurs because the number of cavity modes becomes comparable to the number of atoms. Therefore, adopting beyond-mean field approaches becomes necessary. Moreover, it has been demonstrated that including light-matter correlations can remarkably alter the nature of the phase transitions and the properties of these intrinsically nonequilibrium systems [59, 60]. Furthermore, in this case, the spatial structure of the matter-light coupling strength do assume a role, since it explicitly contains the Hermite Gaussian transverse

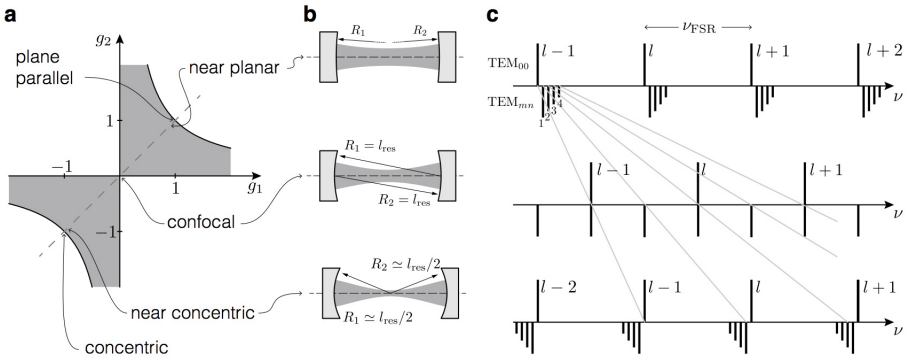

Fig. 1.10. a) Diagram showing the stable configurations for a cavity, $0 \leq g_1 g_2 \leq 1$ (grey area). Stable configurations on the $g_1 = g_2$ dashed line are schematically represented in b) along with the corresponding cavity spectrum c). Longitudinal modes are shown above the frequency axis along with the Gaussian $TEM_{0,0}$, while higher transverse modes are shown below the axis. While in the near planar cavity, modes with same l index are nearly degenerate, they migrate to different longitudinal modes when approaching the near confocal and concentric configurations. Reprinted figure with permission from Ref. [39]. Copyright (2021) by Taylor&Francis Online (Website).

mode functions as

$$g(\mathbf{r}) = g(x, y) = \frac{g_0 \Omega_p \Xi_{m,n}(x, y)}{\Delta_a} \tag{1.49}$$

where g_0 is the atom-cavity coupling rate at $x = y = 0$, Δ_a is the detuning between the pump beam, with Rabi frequency Ω_p, and the atomic excited state and $\Xi_{m,n}(x, y)$ is the Hermite-Gauss function of the $TEM_{m,n}$ mode at the transverse plane (x, y) of the cavity. Typically, the single-mode cases under scrutiny are Fabry-Perot cavities supporting a single cavity mode, the $TEM_{0,0}$ mode, with a Gaussian spatial profile, and atoms located at (x, y) mediate pump-mode scattering processes at a rate $g = g_0 \Omega_p \Xi_{0,0}(x, y)/\Delta_a$.

One major limit coming from single or few-modes cavities is that they do not allow for manipulation of cavity-mediated atom-atom interaction range. Such systems display a global range character whose physical effects are in general well described by mean-field equations. On the other hand, the authors in [63] demonstrate that the interatomic interaction range can be reduced by allowing more modes to participate in the overall dynamics. Due to the multimode cavity system, a spatially structured superradiant emission is observed when transversely pumping a BEC above a critical value and close in frequency to a set of cavity modes [68]. The novel phase reported in [68] expresses a peculiar form of non-

equilibrium condensation called 'supermode-density-wave-polariton' condensate, a joint state of matter and light field where the material component is represented by the atomic density-wave (DW) which follows the self-organisation process previously discussed and the photonic component, the supermode, which is a superposition of bare cavity modes mixed by the interaction with the BEC. The cavity is not confocal (the confocal condition is obtained when the cavity length L is set to almost match the radius of curvature R of the mirrors $\delta L = L - R \simeq 0$), and although not all modes are degenerate, the cavity spectrum presents isolated families of modes whose frequencies are nearly degenerate within a given family, therefore allowing a tunable degeneracy by properly moving close or further from resonance to a particular mode. Furthermore, by changing the BEC's position within the cavity and locating it with respect to the bare cavity modes remarkably affects the structure of the superradiant pattern emitted by the supermode-DW-polariton condensate, yielding the spatial configuration of the supermode, see Fig.(1.11). Thus, by tuning the laser close to the mode resonances within the family $m+n = 6$, as an example, the emitted light pattern reflects a particular superposition of the modes contained in that family. This phenomenon is accompanied by a $\mathbb{Z}_2$ symmetry breaking, where the field assumes either a ϕ or $\phi + \pi$ with respect to the laser source phase, and a spontaneous self-ordering of the BEC's wavefunction in one of the two possible checkerboard lattices associated to the two phases of the intra-cavity field, as previously discussed.

For the discussion of the research in chapter 4, we now briefly describe the work in Ref.[64]. The authors show how a system of spins scattering photons in a multimode confocal cavity, exploiting driving and dissipation, effecively realises a Hopfield model [69, 70, 71] simulating a neural network working as an associative memory. Artificial neural networks [72, 73] are constituted by interconnected units, artificial neurons (e.g., spins) whose configuration is dictated by signals sent by other units [74, 75, 76]. These signals in a cavity-QED system can be electromagnetic fields that spins exchange, playing the role of synapses in this analog of neural network [57, 77]. Additional studies have explored the possibility of employing quantum-optical systems as platforms for the realisation of neural networks [78, 79, 80, 81].

Specific arrangements of the spins define the connectivity of the neural network and can be represented by an energy cost function. The goal is finding the ground state configuration that minimise the energy functional by letting the system evolve. In the case of an associative memory, this can be interpreted in the following way: given a number of spins

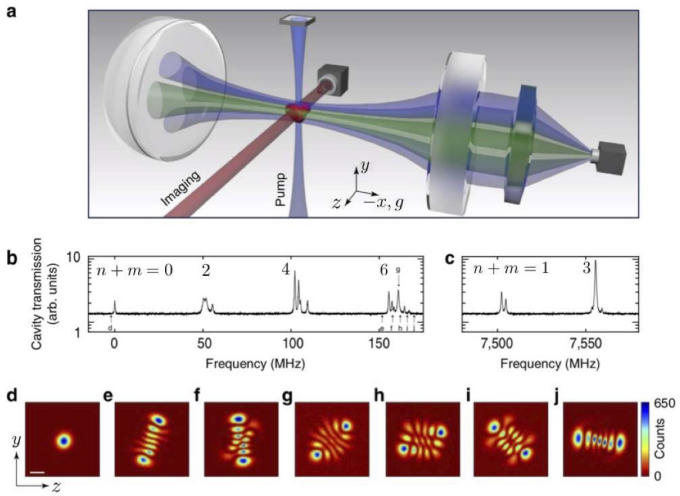

Fig. 1.11. a) Multimode cavity-QED setup showing a transverse driven BEC at the center of the resonator. Cavity spectrum showing the resonances associated to families of even (b) and odd (c) $m + n$ modes. Superradiant emission in the $TEM_{0,0}$ mode (d) and in various superpositions of modes within the $m + n = 6$ family (e-j), showing the structure of the supermodes. Reprinted figure with permission from Ref. [39]. Copyright (2021) by Taylor&Francis Online (Website). The original figure of Ref [68] was published in 2017 by the Nature Publishing Group.

located at different points in the cavity that realise a specific connectivity, a number N of patterns of spin alignments is stored in the cavity-QED network as memories, minima of the energy landscape, that can be recovered by the system [64]. By injecting a corrupted pattern in the cavity-QED system, if this is not too far in energy from the memory to be retrieved, then the system will evolve towards the steady state configuration that matches the stored pattern. Since, as we will see, the multimode cavity-QED model we will discuss here and in chapter 4, can be connected with an Ising model, we can think of the physical evolution of the driven-dissipative system as following an energy minimisation process of the related Ising problem.

Associative memories are characterised by two properties: capacity, i.e, the number of patterns that are stored, and robustness, the dimension of the basin of attraction of a pattern or memory. As the number of memories increases, the system enters a regime of spin glass [82] preventing the associative memory to find desired patterns.

The model considered in Ref.[64] that realises the Hopfield-Ising model that we will use

as starting point for our analysis in chapter 4 is the multimode Dicke model:

$$\dot{\rho} = -i[H,\rho] + \kappa \sum_m \mathcal{D}[a_m]$$
$$H = \sum_m \left(\omega_m a_m^\dagger a_m + \varphi_m(a_m^\dagger + a_m)\right) + \omega_0 \sum_{i=1}^{N_E} S_i^z + g \sum_m \sum_{i=1}^{N_E} \eta_{im} S_i^x (a_m^\dagger + a_m) + \chi(t) \sum_{i=1}^{N_E} S_i^x . \tag{1.50}$$

where we have a total number N of spins-$1/2$ transverse pumped, and whose energy splitting is proportional to ω_0, distributed in N_E localised ensembles within the transverse plane of a multimode cavity. Each ensemble is composed by M_i spins so that $\sum_{i=1}^{N_E} M_i = N$ and behaves as a collective spin $S_i = M_i/2$. The spin ensembles scatter photons with, in principle, an infinite number of modes a_m, each one decaying at a rate κ. ω_m is the frequency detuning between each cavity mode and the pump, and the dispersion relation in the near degenerate regime is given by $\omega_m = \omega_c + \epsilon\delta\omega_m$, with $\epsilon \ll 1$ and ω_c is the bare cavity frequency. The term proportional to φ_m describes a longitudinal pumping term used to inject potential corrupted memories in the cavity. The coupling strength $\eta_{im} = \Xi_m(\mathbf{r}_i) g_0 \Omega_p \cos(\phi_m)/\Delta_a$, expressed in terms of the Hermite-Gaussian TEM modes (functions of the transverse vector) and the Gouy phase ϕ_m, quantifies the interaction between the ith spin ensemble and the mth mode, while g gives an overall coupling strength between atoms and modes. The last term describes a classical noise term used in [64] to study the dynamics in a restricted subspace of states to allow for comparisons with other associative memory models. We are going to neglect such a term and that proportional to φ_m in chapter 4.

This system shows the typical $\mathbb{Z}_2$ superradiant transition where cavity-mediated photon exchanges among ensembles determine the relative spin orientation accompanied by coherent light emission above the normal-to-superradiant critical point. Since Eq.(1.50) refers to the dynamics of a finite number of atomic ensembles coupled to a potentially infinite number of photon operators of the cavity, the first aspect we will care about in chapter 4 will be to shift to an equivalent picture but describing atoms coupled to superpositions of bare cavity modes we have discussed above, the supermodes. This will reduce the number of effective degrees of freedom involved in the dynamics. Then, we will show that with a proper unitary transformation, the multimode Dicke model encodes an Ising

model. Solving the dynamics of the Dicke model will mean finding the ground state of the related Ising model. We will employ a cumulant approach to extract statistics of the spin alignment configurations addressing its ability in finding the ground state.

Chapter 2

Methods

This chapter is dedicated to introducing the methods that will be applied in chapters 3 and 4. After introducing some concepts on the theory of open quantum systems in section 2.1, from the properties of the density matrix to the equation governing its dynamics, we will discuss the Redfield theory in section 2.2, a method to characterise the dynamics of a small quantum system while this interacts with a large environment. The resulting equation of motion could be considered the second order of a perturbative expansion in the system-environment coupling when this is sufficiently weak. The equation will depend on system degrees of freedom only, becoming a relevant tool when tackling many body problems. As we will see in the third chapter, there are cases where the Redfield theory can fail. Section 2.3 then discuss a method to go beyond the second order Redfield theory by means of Keldysh diagrams. Section 2.4 will provide an overview on the most relevant spectral features of Liouvillian superoperators describing physical systems which undergo symmetry-breaking dissipative phase transitions. Finally, in section 2.5, we will discuss properties and limits of the mean field approximation, and approaches to decouple higher order correlation functions of non commuting operators within the framework of the cumulant expansion.

2.1 Theory of open quantum systems

From the description of the physical system in Chapter 1, i.e. an ensemble of laser-driven atoms coupled to one or more electromagnetic modes in a dissipative cavity, we

have understood that its nature is that of an open quantum system. Here, we start by giving a definition and then characterising the dynamics of an open quantum system. To this aim, we will discuss the concept of density operator as a representation of the state characterising an open quantum system. By means of the density operator, one can perform operations such as defining expectation values of physical observables and much more, as we will see.

To start, let us suppose to have a combined system, constituted by two subsystems, S and B. The former, S, is said to be an open quantum system because it interacts with the other quantum system, B, generally termed as the environment. The dynamics of the subsystem S is thus influenced by the presence of B and in general the evolution of the state of S will be the result of its own internal dynamics plus the interaction with its environment. As such, the dynamics of S can no longer be governed by the Hamiltonian only, because both S and B exchange energy and develop correlations. Therefore, the formulation of the dynamics as expressed by the Von Neumann equation [19] ($\hbar = 1$)

$$\frac{d\rho}{dt} = -i[H, \rho] \tag{2.1}$$

needs to be expanded to account for those processes. The above equation describes the dynamics of a closed system, governed by the Hamiltonian.

Having written Eq.(2.1), we give the definition of density operator ρ representing the state of a generic system:

$$\rho = \sum_i p_i |\phi_i\rangle\langle\phi_i| \tag{2.2}$$

where $\{|\phi_i\rangle\}$ is a set of orthonormal state vectors and p_i are non negative weights of the mixed state. The density operator is an alternative representation of the physical state of a quantum system, providing information about the statistical properties such as the probabilities associated with the outcomes of a measurement process on the system. Equation (2.2) describes a Hermitian, positive semi-definite operator with trace one:

$$\rho = \rho^\dagger, \quad \rho \geq 0, \quad \mathrm{Tr}(\rho) = 1 \tag{2.3}$$

with $\mathrm{Tr}(\rho) = \sum_i p_i = 1$ and where the second condition above implies that all eigenvalues

are positive.

Let $\mathcal{H}_S$ and $\mathcal{H}_B$ be the Hilbert spaces of operators acting on the state of the reduced system and environment, respectively. Then, the space of the combined $S+B$ system is represented by the tensor product of those spaces, $\mathcal{H}_S \otimes \mathcal{H}_B$. In this fashion, the Hamiltonian of the total $S + B$ system is given by

$$H = H_S \otimes I_B + I_S \otimes H_B + H_I \tag{2.4}$$

where H_S and H_B describe the energies of the system and the environment, respectively, I_i indicates the identity on the Hilbert space $\mathcal{H}_i$ ($i = S, B$), while the last term in Eq.(2.4) describes the interaction between S and B. Analogously, if the system and the environment are uncorrelated, the density operator of the combined system is expressed by the tensor product of the two:

$$\rho = \rho_S \otimes \rho_B \tag{2.5}$$

and, if one is interested in determining the state of the system, this is achieved by taking the partial trace over the environment degrees of freedom:

$$\rho_S = \mathrm{Tr}_B(\rho). \tag{2.6}$$

This in turn can be exploited to calculate expectation values of operators A acting on the Hilbert space of the system:

$$\langle A \rangle = \mathrm{Tr}_S(A\rho_S). \tag{2.7}$$

where, as for Eq.(2.6), Tr_S indicates the partial trace over the system degrees of freedom. Proceeding on this line, typically, the environment is constituted by a much larger number of degrees of freedom with respect to the open system, forcing one to write down an accordingly large set of equations of motion for each degree of freedom. In addition, one usually finds it is more relevant to focus on the properties of the system and measure its observables. For this reason, we are interested in methods yielding an equivalently good description of the problem but in terms of fewer variables, typically those of the system S. This topic will be the core of the subsequent sections.

We next discuss the formal properties of the time evolution of an open quantum system; these properties will represent the basis for subsequent discussion on practical approaches to derive the open system dynamics of the system S in the following sections.

Let us consider the total system to be initially prepared in an uncorrelated state of the form in Eq.(2.5). The state of the system at a future time $t \geq 0$ can be given by means of a unitary time evolution operator acting on the total system and tracing out the environment:

$$\rho_S(0) \rightarrow \rho_S(t) = \mathrm{v}(t)\rho_S(0) = \mathrm{Tr}_B\{U(t,0)[\rho_S(0) \otimes \rho_B]U^\dagger(t,0)\} \tag{2.8}$$

where $U(t,0) = \exp(-iHt)$. The superoperator $\mathrm{v}(t)$ is thus a linear operation projecting the space of the density matrices into itself and is termed *dynamical map*. To extract the form of this map [19], one starts from the representation of the density operator of the environment in terms of a set of orthonormal state vectors $\{|\varphi_\beta\rangle\}$ and positive real-valued weights λ_β summing up to 1:

$$\rho_B = \sum_\beta \lambda_\beta |\varphi_\beta\rangle\langle\varphi_\beta|. \tag{2.9}$$

With the help of operators acting on the system's space state, defined as:

$$W_{\alpha\beta}(t) = \sqrt{\lambda_\beta}\langle\varphi_\alpha|U(t,0)|\varphi_\beta\rangle \tag{2.10}$$

obeying the following relation

$$\sum_{\alpha\beta} W^\dagger_{\alpha\beta}(t)W_{\alpha\beta}(t) = \mathbb{I} \tag{2.11}$$

one can find Eq.(2.8) by expressing the map as

$$\mathrm{v}(t)\rho_S(0) = \sum_{\alpha\beta} W_{\alpha\beta}(t)\rho_S(0)W^\dagger_{\alpha\beta}(t). \tag{2.12}$$

In virtue of Eq.(2.11), the operators $W_{\alpha\beta}$ guarantee the unit trace of the system density operator.

By varying the parameter t continuously, the set of dynamical maps $\{\mathrm{v}(t)|t \geq 0\}$ ($\mathrm{v}(0) = \mathbb{I}$) representing the time evolution of the open system S is termed quantum dynamical

semigroup if and only if the following condition is respected:

$$\mathrm{v}(t_1)\mathrm{v}(t_2) = \mathrm{v}(t_1 + t_2), \quad t_1, t_2 \geq 0. \tag{2.13}$$

The quantum dynamical semigroup can be then expressed by means of its generator as

$$\mathrm{v}(t) = \exp\{(\mathcal{L}t)\} \tag{2.14}$$

The above equation then yields the equation of motion of the open system:

$$\frac{d\rho_S}{dt} = \mathcal{L}\rho_S \tag{2.15}$$

where $\mathcal{L}$ is a super-operator acting on the space of the density matrices and the generator of the dynamical semigroup [19]. This is commonly named *Liouvillian* since it is the "open system" analogue of the Liouville operator in the dynamics of closed systems, represented by the commutator of the density matrix with the Hamiltonian of the system. To get an explicit form of the super-operator, we begin by considering the open system's Hilbert space to be finite-dimensional, $\dim\mathcal{H}_S = N$. As such, the space of the Liouvillian superoperators has a dimension N^4. A complete set of orthonormal operators, F_i, $(\mathrm{Tr}(F_i^\dagger F_j) = \delta_{ij})$, with $i = 1, ..., N^2$, spanning the space of operators acting on the system's Hilbert space, can be chosen. The basis operators can be selected to have the first $N^2 - 1$ operators with trace 0 and the N^2-th proportional to the identity matrix, $F_{N^2} = \mathbb{I}_S/\sqrt{N}$. If one expresses the operators $W_{\alpha\beta}(t)$ as a superposition of the orthonormal operators F_i

$$W_{\alpha\beta}(t) = \sum_{i=1}^{N^2} f_i^{\alpha\beta} F_i \tag{2.16}$$

where

$$f_i^{\alpha\beta} = \langle F_i, W_{\alpha\beta}(t)\rangle = \mathrm{Tr}_S\{F_i^\dagger W_{\alpha\beta}(t)\} \tag{2.17}$$

$f_i^{\alpha\beta}$ is the coefficient given by the inner product $\langle F_i, W_{\alpha\beta}(t)\rangle$. Then Eq.(2.12) can be

rewritten in terms of the basis of F_i:

$$\mathrm{v}(t)\rho_S = \sum_{i,j=1}^{N^2} c_{ij} F_i \rho_S F_j^\dagger \tag{2.18}$$

with $c_{ij} = \sum_{\alpha\beta}\langle F_i, W_{\alpha\beta}(t)\rangle(\langle F_j, W_{\alpha\beta}(t)\rangle)^*$ being a Hermitian and positive matrix.

Now using Eq.(2.14,2.18), a preliminary form of the action of the Liouvillian on the system's density operator can be written as:

$$\begin{aligned}\mathcal{L}\rho_S &= \lim_{\epsilon\to 0}\frac{\mathrm{v}(\epsilon)\rho_S - \rho_S}{\epsilon} \\ &= \frac{a_{N^2,N^2}}{N}\rho_S + \frac{1}{\sqrt{N}}\sum_{i=1}^{N^2-1}\left(a_{i,N^2}F_i\rho_S + a_{N^2,i}\rho_S F_i^\dagger\right) + \sum_{i,j=1}^{N^2-1} a_{ij}F_i\rho_S F_j^\dagger\end{aligned} \tag{2.19}$$

where a is a Hermitian, positive matrix and $a_{N^2,N^2} = \lim_{\epsilon\to 0}\frac{c_{N^2,N^2}(\epsilon)-N}{\epsilon}$, $a_{i,N^2} = \lim_{\epsilon\to 0} c_{i,N^2}(\epsilon)/\epsilon$, $a_{ij} = \lim_{\epsilon\to 0} c_{ij}(\epsilon)/\epsilon$ $(i,j = 1,...,N^2-1)$. By defining new operators such as

$$\begin{aligned}F &= \frac{1}{\sqrt{N}}\sum_{i=1}^{N^2-1} a_{i,N^2}F_i \\ G &= \frac{1}{2N}a_{N^2,N^2}\mathbb{I}_S + \frac{1}{2}(F + F^\dagger) \\ H &= \frac{1}{2i}(F - F^\dagger),\end{aligned} \tag{2.20}$$

Eq.(2.19) can be recast in the following form

$$\mathcal{L}\rho_S = -i[H,\rho_S] + \{G,\rho_S\} + \sum_{i,j=1}^{N^2-1} a_{ij}F_i\rho_S F_j^\dagger. \tag{2.21}$$

When tracing over the system degrees of freedom and exploiting the trace-preserving property of the dynamical semigroup, one gets

$$0 = \mathrm{Tr}(\mathcal{L}\rho_S) = \mathrm{Tr}\left[\left(2G + \sum_{i,j=1}^{N^2-1} a_{ij}F_j^\dagger F_i\right)\rho_S\right] \tag{2.22}$$

which imposes $2G + \sum_{i,j=1}^{N^2-1} a_{ij} F_j^\dagger F_i = 0$ and thus

$$G = -\frac{1}{2} \sum_{i,j=1}^{N^2-1} a_{ij} F_j^\dagger F_i \tag{2.23}$$

Substituting the above expression for G in Eq.(2.21) yields [83]

$$\mathcal{L}\rho_S = -i[H, \rho_S] + \sum_{i,j=1}^{N^2-1} a_{ij} \left(F_i \rho_S F_j^\dagger - \frac{1}{2} \left\{ F_j^\dagger F_i, \rho_S \right\} \right) \tag{2.24}$$

By means of a unitary transformation U, one could move to a new basis of operators, A_γ, for the Liouville space, therefore writing $F_i = \sum_{\gamma=1}^{N^2-1} u_{\gamma i} A_\gamma$ so that Eq.(2.24) becomes

$$\mathcal{L}\rho_S = -i[H, \rho_S] + \sum_{\gamma=1}^{N^2-1} \kappa_\gamma \left(A_\gamma \rho_S A_\gamma^\dagger - \frac{1}{2} \left\{ A_\gamma^\dagger A_\gamma, \rho_S \right\} \right) \tag{2.25}$$

where κ_γ are positive eigenvalues of the matrix a, diagonalised by means of the unitary matrix u. Both the forms of Eq.(2.24) and Eq.(2.25) are considered the most general expressions of the generator of the dynamical semigroup in a finite size Hilbert space. The former has been derived by Gorini, Kossakowsky and Sudarshan [83] while the latter has been proved in a theorem by Lindblad [18]. With reference to Eq.(2.25), the first term in the equation describes the unitary dynamics of the open system, governed by the total Hamiltonian (comprising the system, the environment and their mutual interaction) while, the contribution within the sum describes energy losses from the system to the environment at rates given by κ_γ. We will see in the next section that these rates are determined by the correlation functions of the environment. For the reason just discussed, the term within the sum in Eq.(2.25) is commonly referred to as *dissipator*:

$$\mathcal{D}[\rho_S] = \sum_{\gamma=1}^{N^2-1} \kappa_\gamma \left(A_\gamma \rho_S A_\gamma^\dagger - \frac{1}{2} \left\{ A_\gamma^\dagger A_\gamma, \rho_S \right\} \right) \tag{2.26}$$

so that the density matrix equation of motion in Lindblad form generally reads

$$\frac{d\rho_S}{dt} = \mathcal{L}\rho_S = -i[H, \rho_S] + \mathcal{D}[\rho_S]. \tag{2.27}$$

Among the techniques used to analyse dynamics of open quantum systems described by Lindblad master equations, the literature includes input-output theory [84], quantum trajectories and measurement [85, 86, 87, 88].

Importantly, Eq.(2.15) and the steps leading to the formulation of Eq.(2.25) rely on the condition of negligible correlations between the open system and the environment and the fact that the system response is local in time. For this reason, Eq.(2.15) and Eq.(2.25) are known as Markovian master equations.

In the following section, we will discuss the role of the Markov approximation in a method to derive a density matrix equation of motion for the system only, given its interaction with an external environment. As we will see, such an equation will not always be in Lindblad form. We will thus explore methods to try providing this property.

2.2 Redfield theory

As anticipated, this section will be dedicated to methods for the derivation of the equation of motion for one subsystem of the bipartite $S + B$ system, averaging over the degrees of freedom of the remaining subsystem. The theory discussed here will be important for the development of an effective atom-only theory describing the superradiance phase transition of a U(1)-symmetric Dicke model treated in section 2.4, that we will detail in the next Chapter.

As we have seen in the previous section, Eq.(2.15) formally describes the dynamics of the system density matrix determined by the Liouvillian superoperator. However, in a general situation, one starts from a model that takes into account the interaction between the system and the environment. One should thus move to an approach providing a density matrix equation of motion for the system only, where the environment is traced out as part of the procedure. Such a result can be reached by means of the Redfield theory that we now discuss.

In line with the description in the previous section, the physical picture we start with is an open system S weakly interacting with its environment B consisting of a much

larger number of degrees of freedom. This composite system is described by Hamiltonian Eq.(2.4) that is re-introduced here, dropping the notation involving the tensor product with the Identity operator for brevity:

$$H = H_S + H_B + H_I \tag{2.28}$$

where the first and second term represents the energy of the system and the environment, respectively. The coupling between the two subsystems is captured by H_I. For convenience, the standard derivation of the equation of motion is carried out in interaction picture, starting from the Liouville-Von Neumann equation for the density matrix of the composite system

$$\frac{d\rho(t)}{dt} = -i[H_I(t), \rho(t)] \tag{2.29}$$

whose solution is given by

$$\rho(t) = \rho(0) - i \int_0^t dt' [H_I(t'), \rho(t')]. \tag{2.30}$$

Substituting Eq.(2.30) into Eq.(2.29) yields

$$\frac{d\rho_S(t)}{dt} = -\int_0^t dt' \mathrm{Tr}_B[H_I(t), [H_I(t'), \rho(t')]] \tag{2.31}$$

where the trace over the environment Tr_B is performed on both sides of the equation, together with the assumption, $\mathrm{Tr}_B[H_I(t), \rho(0)] = 0$.

According to Eq.(2.31), the double commutator includes the density matrix of the total system at time t'. To provide an equation of motion for the density matrix of the system S, two approximations are commonly applied on Eq.(2.31). The first one considers the joint system to be in a weak coupling regime. Specifically, the change of state in the environment B due to the interaction with the system S is negligible because of the initial assumption on the environment being considerably larger than the system. Such an assumption allows to consider the total system to be in a factorised state, neglecting any correlations between

S and B, i.e.

$$\rho_t(t) = \rho_S(t) \otimes \rho_B \tag{2.32}$$

The second approximation assumes that the state of the system S evolves on a slower time scale compared to the decay times of the correlation functions of the environment. In other words, the system follows adiabatically the change of configuration of the environment and this behaviour can be mathematically expressed by taking $\rho_S(t') \approx \rho_S(t)$ at the present time t. The two combined approximations are the so-called *Born-Markov* approximation and, once applied to Eq.(2.31), they gives the following local in time integro-differential equation for $\rho_S(t)$ [19, 89]

$$\frac{d}{dt}\rho_S(t) = -\int_0^t dt' \mathrm{Tr}_B[H_I(t), [H_I(t'), \rho_S(t) \otimes \rho_B]] \tag{2.33}$$

By changing the time dependence in the integral so that $t' \to t - \tau$ and taking the upper limit to be $t \to \infty$, this yields

$$\frac{d}{dt}\rho_S(t) = -\int_0^\infty dt' \mathrm{Tr}_B[H_I(t), [H_I(t - t'), \rho_S(t) \otimes \rho_B]] \tag{2.34}$$

Eq. (2.34) is known as *Redfield* master equation [90, 19].

In order to give a more explicit form of Eq.(2.34), let us consider the structure of the interaction Hamiltonian, typically given by a tensor product of Hermitian operators acting on the system and environment Hilbert spaces:

$$H_I = \sum_\alpha S_\alpha \otimes B_\alpha + \mathrm{H.c.} \tag{2.35}$$

Then we move to the interaction picture with respect to the unperturbed Hamiltonian, $H_0 = H_S + H_B$ and express S_α

$$\begin{aligned} e^{iH_S t} S_\alpha e^{-iH_S t} &= S_\alpha(t) \\ e^{iH_S t} S_\alpha^\dagger e^{-iH_S t} &= S_\alpha^\dagger(t) \end{aligned} \tag{2.36}$$

The time dependence of the environment degrees of freedom is given by $B_\alpha(t) = e^{iH_B t} B_\alpha e^{-iH_B t}$ and can be found by solving Heisenberg equations.

Writing in terms of operators $A_\alpha(\omega)$ such as $S_\alpha(t) = \sum_\omega A_\alpha(\omega)e^{-i\omega t}$, substituting H_I in the interaction picture in Eq.(2.34) and solving the integral provides

$$\frac{d}{dt}\rho_S(t) = \sum_{\omega,\omega'}\sum_{\alpha,\beta} e^{i(\omega-\omega')t}\kappa_{\alpha\beta}(\omega)\left(A_\beta(\omega)\rho_S A_\alpha^\dagger(\omega') - A_\alpha^\dagger(\omega')A_\beta(\omega)\rho_S\right) + \text{h.c.} \quad (2.37)$$

In connection with the assumption $\mathrm{Tr}_B[H_I(t), \rho(0)] = 0$, we consider $\langle B_\alpha(t)\rangle = \mathrm{Tr}_B\left(B_\alpha(t)\rho_B\right) = 0$, while two-time correlations of the environment are expressed by

$$\kappa_{\alpha\beta}(\omega) = \int_0^\infty dt' e^{i\omega t'}\langle B_\alpha^\dagger(t)B_\beta(t-t')\rangle = \int_0^\infty dt' e^{i\omega t'}\langle B_\alpha^\dagger(t')B_\beta(0)\rangle \quad (2.38)$$

where the last equality describes correlations that are constant in time because the state of the environment ρ_B is assumed to be in a stationary state.

Eq.(2.37) has an explicit dependence on oscillating functions whose frequency is given by the difference $\omega - \omega'$. If t_S is the time scale expressed by the inverse of $|\omega - \omega'|$ $(\omega' \neq \omega)$, and t_R is the time required to the system to reach a out-of-equilibrium steady state then for $t_S \ll t_R$, the terms $e^{i(\omega-\omega')t}$ are fast oscillating over time and average to 0, thus yielding

$$\frac{d}{dt}\rho_S(t) = \sum_{\omega}\sum_{\alpha,\beta} \kappa_{\alpha\beta}(\omega)\left(A_\beta(\omega)\rho_S A_\alpha^\dagger(\omega) - A_\alpha^\dagger(\omega)A_\beta(\omega)\rho_S\right) + \text{h.c.} \quad (2.39)$$

This approximation is known as *secular approximation* and typically guarantees the positivity of the equation of the motion and therefore the Lindblad form [91]. The rates $\kappa_{\alpha\beta}(\omega)$ are generally given in terms of a real and an imaginary part

$$\kappa_{\alpha\beta}(\omega) = \frac{1}{2}\gamma_{\alpha\beta}(\omega) + iS_{\alpha\beta}(\omega) \quad (2.40)$$

and, while the $S_{\alpha\beta}(\omega)$ provide a renormalization of the energies of the open system Hamiltonian, the term $\gamma_{\alpha\beta}(\omega)$ describes a positive Hermitian matrix representing the power spectrum of the environment

$$\gamma_{\alpha\beta}(\omega) = \kappa_{\alpha\beta}(\omega) + \kappa_{\alpha\beta}^*(\omega) = \int_{-\infty}^\infty dt' e^{i\omega t'}\langle B_\alpha^\dagger(t)B_\beta(t-t')\rangle \quad (2.41)$$

Eq.(2.39) can be cast in the form

$$\frac{d}{dt}\rho_S(t) = -i[H'_S, \rho_S(t)] + \mathcal{D}(\rho_S(t)) \tag{2.42}$$

with

$$\begin{aligned} H'_S &= H_S + H_{LS} = H_S + \sum_{\omega} \sum_{\alpha,\beta} S_{\alpha\beta}(\omega) A^{\dagger}_{\alpha}(\omega) A_{\beta}(\omega) \\ \mathcal{D}(\rho_S(t)) &= \sum_{\omega} \sum_{\alpha,\beta} \gamma_{\alpha\beta}(\omega) \left(A_{\beta}(\omega) \rho_S(t) A^{\dagger}_{\alpha}(\omega) - \frac{1}{2} \left\{ A^{\dagger}_{\alpha}(\omega) A_{\beta}(\omega), \rho_S(t) \right\} \right). \end{aligned} \tag{2.43}$$

Eq.(2.42) is in the first standard form of Eq.(2.24) and can be cast in Lindblad form by diagonalising the matrix $\gamma_{\alpha\beta}(\omega)$.

It is important to stress that the approximations adopted here rely on the assumption that the environment is remarkably large compared to the system and its frequency spectrum tends to be continuous as a reflection of the high number of modes. Moreover, correlations between the system and the environment are neglected due to the weak system-environment coupling approximation and finally the density matrix equation of motion is local in time and Markovian.

There can be cases where Redfield theories do not meet the property of positivity but still they capture correct dynamics [92, 93, 94, 95, 91, 96]. These theories can achieve a Lindblad form when the secular approximation, i.e., neglecting time-dependent terms in the interaction picture [97, 91], is applied to the equation. We will come back to this aspect when discussing a two-mode Dicke model in chapter 3.

As expressed by Eq.(2.34), the density matrix equation of motion for the system can be thought as the second order of a perturbative expansion in the system-environment coupling parameter, based on the aforementioned weak coupling approximation. There might be cases where the standard Redfield equation is not a sufficient description of system behaviour and higher order terms must be included for a good comparison with the original problem [98]. In the next section, we are going to discuss a systematic method to evaluate higher order terms in the Redfield equation [99].

2.3 Time-dependent perturbation theory with Keldysh diagrams

In this section, we are going to discuss a method to evaluate density matrix equations of motion for the reduced system that go beyond the usual second order Redfield theory in the system-environment coupling strength. The procedure is a time-dependent perturbation theory in the coupling parameter based on Keldysh diagrams and is thoroughly detailed in Ref.[99] with additional practical applications. The work in [99] aims at connecting the Keldysh selfenergy formalism and the Lindblad theory in the context of driven-dissipative systems. The method based on the Keldysh diagrams [100, 101] has been used in non-equilibrium systems [102] and to characterise mesoscopic systems [103, 104, 105, 106, 107]. While the technique has proved to be successful in those cases, the treatment does not usually go beyond the second order or it involves a restricted set of diagrams. The approach adopted in [99] instead classifies the diagrams according to the perturbative order and provides a tool to compute the density matrix equation of motion in Lindblad form resulting from the complete set of diagrams at an arbitrary order.

Here, we will summarise what was done in Ref.[99] by describing the technique and giving the interpretation of the Keldysh diagrams. We thus start from the expression of the density matrix equation of the system:

$$\frac{d\rho}{dt} = \sum_k \mathcal{L}^{(k)}\rho. \tag{2.44}$$

To simplify the notation, we will refer to the full density matrix as ρ_t, the system density matrix as ρ, and the superscripts SP and IP will stand for Schroedinger and interaction picture respectively. As seen earlier in this chapter, the above equation governs the evolution of the system and, under the assumption of weak system-environment coupling, it can be decomposed into a series of contributions or perturbative orders labelled by k. Each Liouvillian superoperator, $\mathcal{L}^{(k)}$, is a combination of coherent processes, where the system evolves according to some effective Hamiltonian, and relaxation processes, represented by dissipators.

To evaluate Eq.(2.44) using the Keldysh approach, we start from the total Hamiltonian

$$H = H_0 + H_I \tag{2.45}$$

constituted by an unperturbed part, describing the system and the environment degrees of freedom, $H_0 = H_S + H_B$, and an interaction term, represented by a coupling parameter. Given the projection operator onto the system states, $P_{mm'} = |m\rangle\langle m'|$, the evolution of the system density matrix in the Schroedinger picture is captured by the equation

$$\begin{aligned}\rho^{SP}_{mm'}(t) &= Tr_B(\rho^{SP}_t(t)|m\rangle\langle m'|) = Tr_B(\rho^{IP}_t(t)U_0^\dagger|m\rangle\langle m'|U_0) = \\ &= Tr_B(U_I\rho^{IP}_t(t_0)U_I^\dagger U_0^\dagger|m\rangle\langle m'|U_0) = \\ &= \sum_{l,l'}\rho_{l,l'}(t_0)\langle l|Tr_B(\rho_B U_I^\dagger P_{mm'}(t)U_I)|l'\rangle = \\ &= \sum_{l,l'}\rho_{l,l'}(t_0)\Pi_{l,l'\to m,m'}(t_0,t).\end{aligned} \tag{2.46}$$

where the Born approximation Eq.(2.32) of a factorised state is assumed and the trace over the environment is performed, yielding the system density operator. Moreover, the density matrix is written in interaction picture (superscript IP) by means of the unitary operator $U_0 = U_0(t,t_0) = e^{-iH_0(t-t_0)}$ and evolves from an initial time t_0 to a final time t due to the time-evolution operators $U_I(U_I^\dagger)$, defined in the interaction picture by

$$U_I = U_I(t,t_0) = \overrightarrow{T}\exp\left\{-i\int_{t_0}^{t}dt_1 H_I(t_1)\right\} \tag{2.47}$$

$$U_I^\dagger = U_I(t_0,t) = \overleftarrow{T}\exp\left\{i\int_{t_0}^{t}dt_1 H_I(t_1)\right\}. \tag{2.48}$$

$\overrightarrow{T}$ and $\overleftarrow{T}$ indicate time-ordering and anti-time ordering respectively. Also, the interaction Hamiltonian is expressed in the interaction picture with respect to H_0, as $H_I(t) = U_0^\dagger H_I U_0$. Finally, Eq.(2.46) introduces the density operator propagator $\Pi_{l,l'\to m,m'}(t_0,t)$ evolving the state of the system from $|l'\rangle\langle l|$ at t_0 to $|m\rangle\langle m'|$ at the final time t. According to Eq.(2.46), the interaction Hamiltonian acts on both sides of the density operator through the unitary time-evolution operators U_I and its Hermitian conjugate. One can then write the Taylor

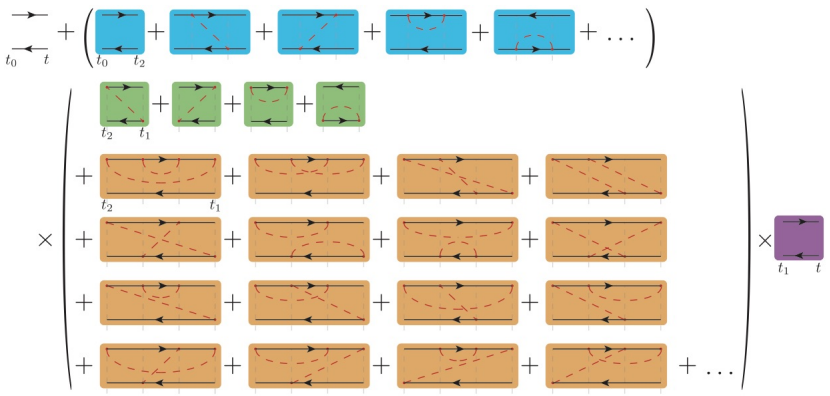

Fig. 2.1. Graphical representation of the propagator $\Pi(t_0, t)$ in Eq.(2.49). The purpose of the figure is to highlight the selfenergy superoperator Σ, containing the series of irreducible diagrams (green and orange displayed here) to be evaluated when solving Eq.(2.52) in the interaction picture. Reprinted figure from Ref. [99] with permission from C. Muller and T.M. Stace, Phys. Rev. A **95**, 013847, 2017. Copyright (2017) by the American Physical Society.

expansion of the unitary operator retaining all the terms at a certain power of the coupling parameter appearing in the interaction Hamiltonian. Given an order k, this operation implies the writing of strings of k instances of time-dependent interaction Hamiltonian acting on both sides of the density operator. Such a procedure could in general cause double counting of contributions within a fixed order of perturbation. As an example, at fourth order one wants to avoid contributions that are just the product of second order terms. As we will see, the diagrammatic representation of the contributions will avoid this. In fact, one could draw a correspondence between the terms in the expansion of U_I and $U_I^\dagger$ and a set of irreducible diagrams, as those in Fig.(2.1). Each diagram is constituted by two oriented solid lines describing free evolution of the system. Within a given order k, the number of applications of H_I is represented by dots drawn along the horizontal lines; in particular, the number of applications coming from U_I ($U_I^\dagger$) corresponds to the number of vertices drawn on the upper (lower) line. In this scenario, there will be a total number k of interaction vertices.

The advantage provided by this graphical method is that the diagrams already include the decomposition of higher order correlation functions of the operators acting on the environment in sums of two-time correlators, according to Wick's theorem [108]. Such two-time correlations are expressed as dashed lines connecting pairs of vertices in the diagrams.

At this point, one can express the propagator $\Pi(t_0, t)$, graphically as in Fig.(2.1) and mathematically as

$$\Pi(t_0, t) = \Pi^0(t_0, t) + \int dt_2 dt_1 \Pi(t_0, t_2)\Sigma(t_2, t_1)\Pi^0(t_0, t) \tag{2.49}$$

where Π^0 is the free evolution and Σ is the selfenergy superoperator represented by the complete set of irreducible diagrams, i.e. diagrams that cannot be further reduced by vertical lines without breaking correlation lines of the environment: taking for example the fourth order diagrams in Fig.(2.1), if we draw a vertical line at any point in any of those diagrams with the aim of getting diagrams that are products of second order diagrams, we would necessarily cut a correlation (dashed) line between operators of the environment. As a consequence, these diagrams cannot be reduced to product of lower order diagrams.

When inserting Eq.(2.49) into Eq.(2.46) and making use of the expression $\Pi^0_{l,l'\to m,m'}(t_0, t) = \delta_{l,m}\delta_{l',m'}e^{-i(E_{m'}-E_m)(t-t_0)}$, we get in the Schroedinger picture (we drop SP here for simplicity)

$$\begin{aligned}
\rho_{mm'}(t) = &\sum_{l,l'} \rho_{l,l'}(t_0)\Pi^0_{l,l'\to m,m'}(t_0, t) + \\
&\sum_{l,l'}\sum_{l_1,l_1'}\sum_{l_2,l_2'} \int_{t_0}^{t} dt_1 \int_{t_0}^{t_1} dt_2 \rho_{l,l'}(t_0)\Pi_{l,l'\to l_1,l_1'}(t_0, t_2)\Sigma_{l_1,l_1'\to l_2,l_2'}(t_2, t_1)\Pi^0_{l_2,l_2'\to m,m'}(t_1, t) \\
= &\rho_{m,m'}(t_0)e^{-i(E_{m'}-E_m)(t-t_0)} + \sum_{l,l'} \int_{t_0}^{t} dt_1 \int_{t_0}^{t_1} dt_2 \rho_{l,l'}(t_2)\Sigma_{l,l'\to m,m'}(t_2, t_1)e^{-i(E_{m'}-E_m)(t-t_1)}
\end{aligned} \tag{2.50}$$

where, in the passage to the third line, the expression of $\Pi^0_{l,l'\to m,m'}(t_0, t)$ eliminates the sum over l and l' in the first term, and the sum over l_2 and l_2' in the second, while, recalling that $\rho_{l,l'}(t_2) = \sum_{l_1,l_1'} \rho_{l,l'}(t_0)\Pi_{l,l'\to l_1,l_1'}(t_0, t_2)$ removes the sum over l_1 and l_1' in the second term. E_m represents the energy of the state $|m\rangle$. From the above, we see that the time evolution of ρ is controlled by the propagator Π.

The time-derivative of Eq.(2.50) finally provides the time evolution of the matrix elements

of the systems density operator:

$$\dot{\rho}_{m,m'}(t) = -i(E_{m'} - E_m)\rho_{m,m'}(t) + \sum_{l,l'} \int_{t_0}^{t} dt_1 \rho_{l,l'}(t_1)\Sigma_{l,l'\to m,m'}(t_1, t) \tag{2.51}$$

Finally, the more compact form, given that $\rho(t) = \sum_{m,m'} \rho_{m,m'}(t)|m'\rangle\langle m|$, is written in the Schroedinger and interaction picture as

$$\begin{aligned} \dot{\rho}^{(SP)}(t) &= -i[H_0, \rho^{(SP)}(t)] + \int_{t_0}^{t} dt_1 \rho^{(SP)}(t_1)\Sigma(t_1, t) \\ \dot{\rho}^{(IP)}(t) &= \int_{t_0}^{t} dt_1 \rho^{(IP)}(t_1)\Sigma(t_1, t) \end{aligned} \tag{2.52}$$

It is important to note that the selfenergy in Eq.(2.52) is exact since it includes all perturbative orders.

To give a concrete example of how the irreducible diagrams identifying the selfenergy are interpreted, let us move to the interaction picture and consider a general interaction Hamiltonian,

$$H_I(t) = g\left(S(t)B^{\dagger}(t) + S^{\dagger}(t)B(t)\right) \tag{2.53}$$

where, for simplicity, we label with S and B operators acting on the Hilbert spaces of the system and environment, respectively, while g describes the coupling strength between them. Then, if we take the second order diagram, shown in Fig.(2.2), as an example, the contributions to the master equation corresponding to those diagrams would be written as

$$\dot{\rho}(t) = \left(\mathcal{L}_A^{(2)} + \mathcal{L}_B^{(2)} + \mathcal{L}_C^{(2)} + \mathcal{L}_D^{(2)}\right)\rho(t)$$

$$\begin{aligned}
\mathcal{L}_A^{(2)}\rho(t) &= \mathrm{Tr}_B\left[\int_{t_0}^{t} dt_1 H_I(t)H_I(t_1)\rho(t_1)\right] \\
\mathcal{L}_B^{(2)}\rho(t) &= \mathrm{Tr}_B\left[\int_{t_0}^{t} dt_1 \rho(t_1)H_I(t_1)H_I(t)\right] \\
\mathcal{L}_C^{(2)}\rho(t) &= -\mathrm{Tr}_B\left[\int_{t_0}^{t} dt_1 H_I(t)\rho(t_1)H_I(t_1)\right] \\
\mathcal{L}_D^{(2)}\rho(t) &= -\mathrm{Tr}_B\left[\int_{t_0}^{t} dt_1 H_I(t_1)\rho(t_1)H_I(t)\right]
\end{aligned} \tag{2.54}$$

where the subscript in $\mathcal{L}^{(2)}$ identifies the diagram. The specific arrangement of operators within the integral is directly read from the diagram: we start from the lower line on the bottom right corner where we may (first and third diagram in Fig.(2.2)) or may not find an interaction vertex, we follow the orientation of the line to the bottom left corresponding to the smallest time t_1 which in the second order diagrams is a dummy variable, and again we might (first and fourth diagram) or not find an interaction point. The operator H_I at the smallest time is always followed (first and fourth) or follows (second and third) the density operator at the same smallest time (t_1 in this case). We thus get to the upper line and repeat the same procedure following the orientation of the line, from t_1 to t. By summing up those integrals, we thus note that the second order Keldysh master equation is equivalent to the Redfield equation, Eq.(2.33), as we show next.

Let us consider the first and the third integral in Eq.(2.54) and substitute the expression for the interaction Hamiltonian Eq.(2.53). Given that the environment is supposed to be prepared in a thermal steady state, for simplicity the vacuum state, and assuming a complete factorised state $\rho_{\mathrm{tot}}(t') = \rho(t') \otimes \rho_B$ for $t_0 < t' < t_1$, the only possible correlation function of the environment is

$$\langle B(t_1)B^\dagger(t)\rangle = \mathrm{Tr}_B\left[B(t_1)B^\dagger(t)\rho_B\right] \tag{2.55}$$

while $\langle B^\dagger(t_1)B(t)\rangle = \langle B(t_1)B(t)\rangle = \langle B^\dagger(t_1)B^\dagger(t)\rangle = 0$ when calculated on the vacuum state of the environment. The time dependence of these operators can be found by solving Heisenberg equations, as we will discuss in the following chapter. As a result, the type of correlation in Eq.(2.55) determines which system operators appear on the vertices connected by a dashed line, and these must be hermitian conjugates pairs of operators.

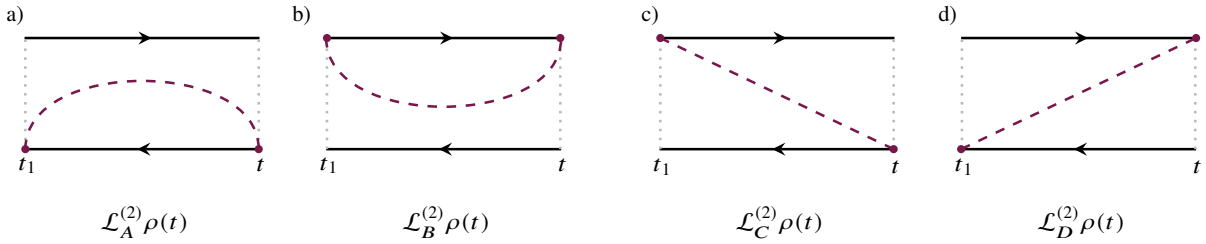

Fig. 2.2. Second order Keldysh diagrams and correspondent contributions to the selfenergy superoperator. Two horizontally oriented black lines define the system free time evolution, interrupted by vertices (purple dots) representing the action of the interaction Hamiltonian. Vertices on the lower (upper) branch are operators acting to the left (right) of the density matrix at the smallest time t_1. Each diagram is meant to be read from the bottom right to the top right vertices, according to the orientations of the black arrows. Purple dashed lines are contractions of two-time correlations of operators of the environment and the $(-)$ is assigned to all the diagrams with an odd number of vertices on the branches.

The two integrals in Eq.(2.54) thus become

$$\begin{aligned}\mathcal{L}_C^{(2)}\rho(t) &= -\int_{t_0}^{t} dt_1 S(t)\rho(t_1)S^\dagger(t_1)\langle B(t_1)B^\dagger(t)\rangle \\ \mathcal{L}_A^{(2)}\rho(t) &= -\int_{t_0}^{t} dt_1 S(t)S^\dagger(t_1)\rho(t_1)\langle B(t_1)B^\dagger(t)\rangle\end{aligned} \tag{2.56}$$

The treatment of fourth and higher order diagrams follows straightforwardly from the above with a number $k-1$ of time integrals to solve for the k-th perturbative order. Moreover, depending on the form of the interaction Hamiltonian, alternative patterns of system operators can be allowed, such as $S(t)S(t_1)$ and $S^\dagger(t)S^\dagger(t_1)$ distributed on either side of ρ, as we will see in chapter 3.

As a note, we consider cases where the perturbative expansion accounts for only even orders since we consider models where any expectation value of the environment operators including odd numbers of operators on any thermal state is zero. There could be other situations where intra-system couplings play a role and therefore contributions from first or third order diagrams may arise. However, for our scope, we are going to analyse only the second and fourth order terms in the Dyson expansion.

2.4 Liouvillians and spectral theory of dissipative phase transitions

The previous discussion has introduced the concept of Liouvillian superoperator as generator of the dynamics of an open system. In this section, we discuss the spectral properties of the Liouvillians and their physical meaning, with particular focus on dissipative phase transitions and symmetries [109, 110, 111, 112, 113].

Phase transitions in closed systems have been widely characterised [114, 115, 116]. In those cases where the dynamics of a system is governed by the Hamiltonian, the symmetry of the model reveals the nature of the excitations emerging when the system undergoes a phase transition breaking the symmetry. The example of a model with U(1) symmetry shows that when the symmetry is broken, modes at zero and finite energy appear [42]. This is shown in Fig.(2.3) where the energy of the system can be expressed by a function of a complex order parameter $\alpha = |\alpha|e^{i\theta}$, defined by an amplitude and a phase. While for values $\alpha < \alpha_c$, the system is in a symmetric state characterised by a bowl-shaped energy function, for values above that threshold, the energy landscape assumes the form shown in Fig.(2.3)b) characterised by a valley of energy minima. The excitations associated to fluctuations of the phase of the order parameter (represented by the arrow along the valley in Fig.(2.3)) are known as Goldstone modes, while those associated to fluctuations of the amplitude are known as Higgs modes.

Our goal now is to identify a similar paradigm in the context of symmetry breaking phase transitions in open systems where the dynamics is governed by the Liouvillian.

We start from the Markovian density matrix equation of motion Eq.(2.27) describing the dynamics of the system, written here in an equivalent form

$$\frac{d\rho_S}{dt} = \mathcal{L}\rho_S = -i[H, \rho_S] + \sum_i \kappa_i \mathcal{D}[A_i]\rho_S. \tag{2.57}$$

where the coherent evolution of the system is controlled by the Hamiltonian and any exchange process with the environment is regulated by the dissipators $\mathcal{D}[A_i]\rho_S = \left(A_i\rho_S A_i^\dagger - \frac{1}{2}\left\{A_i^\dagger A_i, \rho_S\right\}\right)$. The sum over i account for all types of dissipation channels involved, each identified by a Lindblad operator or quantum jump operator A_i and a rate of occurrence κ_i of the process [19]. As discussed, the Liouvillian superoperator

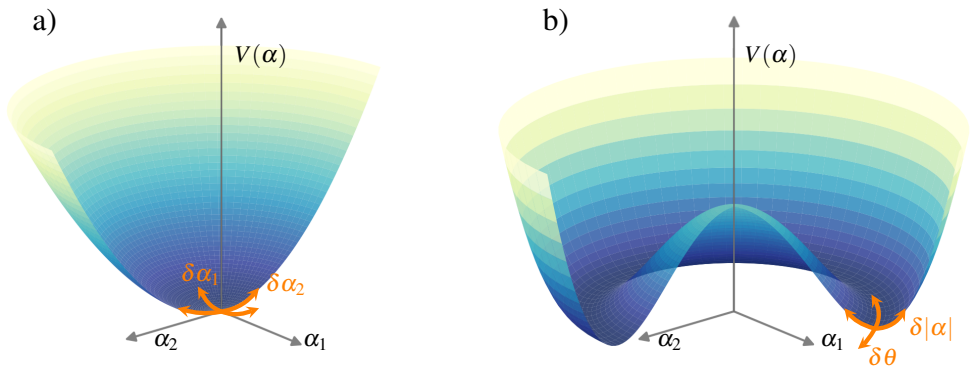

Fig. 2.3. Energy landscape $V(\alpha)$ as a function of the complex order parameter $\alpha = \alpha_1 + i\alpha_2 = |\alpha|e^{i\theta}$ in the normal phase a) and in the symmetry-broken phase b). While in a) any fluctuation of the order parameter is decaying, leading the system to a unique energy minimum, in the symmetry-broken phase b), the fluctuations have amplitude (represented by variations in the modulus of α) and phase character (represented by variations in θ). The excitation associated with the amplitude is known as Higgs mode, while that associated with the phase is known as Goldstone mode.

$\mathcal{L}$ is the generator of a completely positive map $v(t) = e^{\mathcal{L}t}$ which evolves the state of the system [117, 118, 67, 119]. All information regarding the dynamics of the system is contained in the eigensystem of the Liouvillian, when this is diagonalisable:

$$\mathcal{L}\rho_i = \lambda_i \rho_i \tag{2.58}$$

where λ_i and ρ_i are respectively eigenvalues and eigenmatrices of $\mathcal{L}$. The eigenmatrices or eigenstates ρ_i do not satisfy orthogonality ($\rho_i \cdot \rho_j \neq 0$) because $\mathcal{L}$ is not a Hermitian superoperator. However, they can be normalised to have $\|\rho_i\|^2 = 1$, according to the definition of the inner product in Eq.(2.17), and can be used as a basis to express any operator of the system. Therefore, supposing that the system can evolve towards a unique steady state, the state at time t of the system, $\rho(t)$, could be described by the following equation:

$$\rho(t) = \sum_i c_i(t)\rho_i = \rho_{ss} + \sum_{i\neq 0} c_i(0)e^{\lambda_i t}\rho_i \tag{2.59}$$

where, in order to guarantee that $\rho(t)$ is a density matrix with all the properties character-

ising it, we require the steady-state density matrix to satisfy the equation

$$\rho_{ss} = \rho_0/\mathrm{Tr}(\rho_0) \tag{2.60}$$

while $\mathrm{Tr}(\rho_i) = 0$ for $i \neq 0$. Moreover, the eigenvalues can be in general complex and we can picture them in terms of their real and imaginary parts. While the latter gives a frequency, the former is associated with a rate and to satisfy $e^{\mathcal{L}t}\rho_i = e^{\lambda_i t}\rho_i \to 0$ for $t \to +\infty$, the real part of the Liouvillian spectrum must be non zero and negative when $i \neq 0$. In this way, the state of the system approaches the steady-state density matrix, characterised by unitary trace $\mathrm{Tr}(\rho_{ss}) = 1$ and $\mathrm{Re}[\lambda_i]$ thus represent relaxation rates towards the steady-state. To discuss about the dynamics of the system and the identification of the spectral features connected to symmetry-breaking in dissipative phase transitions, it is useful to sort the Liouvillian eigenspectrum by absolute value of the real part as

$$|\,\mathrm{Re}[\lambda_0]| < |\,\mathrm{Re}[\lambda_1]| < \ldots < |\,\mathrm{Re}[\lambda_n]| \tag{2.61}$$

where $\lambda_0 = 0$ and the steady-state density matrix is an eigenstate of the Liouvillian superoperator associated with such an eigenvalue

$$\mathcal{L}\rho_{ss} = 0. \tag{2.62}$$

For a finite size system, the steady state is always unique. However, in the thermodynamic limit of an infinite number of particles and in open systems displaying critical behavior associated with spontaneous symmetry breaking, the zero eigenvalue acquires a degeneracy and, as a consequence, the set of eigenmatrices associated with $\lambda = 0$ describes alternative steady states toward which the system could evolve [109].

To understand better this concept, it is useful to take the example of a dissipative phase transition. As said, while for systems with a finite dimension N, the admitted steady state is always unique, for $N \to +\infty$, the system undergoes a transition from a phase where some parameter ξ is less than a critical value, $\xi < \xi_c$, to another phase when this value is overcome. The phase transition is usually signalled by the divergence or discontinuous change in the expectation value of a ξ-independent observable O of the system when ξ

approaches the critical value. Namely,

$$\lim_{\xi\to\xi_c}\left|\frac{\partial^M}{\partial\xi^M}\lim_{N\to+\infty}\mathrm{Tr}[\rho_{ss}(\xi,N)O]\right|=+\infty \tag{2.63}$$

where M is the order of the phase transition. As discussed above, phase transitions have been studied in closed systems, but they also exist in open systems. As an example, the lasing transition [120, 121, 122, 123] is a second order phase transition where the order parameter ξ is the pump strength and the observable is the photon number. In the $\gamma = 0$ Dicke model discussed in section 1.4 that we will consider in chapter 3, $\xi = g$ and the g-independent observable would be $O = S^z$.

As noted, O does not depend on ξ, therefore any discontinuous behavior derives from the steady state density matrix. Moreover, if the phase transition is connected to a spontaneous symmetry-breaking in the steady state, and given a symmetry-breaking observable (such as S^x in the Dicke model), the dynamics of such an observable is described by another relevant eigenvalue of the Liouvillian. This is λ_1, according to the sorting process in Eq.(2.61), and it is often referred to as Liouvillian gap or asymptotic decay rate [124, 125, 109]. This is the smallest non zero eigenvalue in absolute value and its real part describes the slowest timescale of the dynamics. Therefore, once entering the symmetry-broken phase for $\xi > \xi_c$, the system adopts a new steady state and such fact must imply a vanishing of the Liouvillian gap across the entire $\xi > \xi_c$ region, given the fact that the steady state is always associated with a vanishing eigenvalue. If the system is in the thermodynamic limit where true symmetry-breaking occurs, then, depending on the initial conditions, the system can access multiple steady states, say n, in the symmetry-broken phase. Therefore, the zero eigenvalue will be n-fold degenerate, meaning that $\lambda_0 = \lambda_1 = \ldots = \lambda_{n-1} = 0$ [109].

Since the driven-dissipative cavity QED realization of the Dicke model has a second order $\mathbb{Z}_2$ symmetry breaking phase transition, we are going to discuss first the spectral properties associated with $\mathbb{Z}_2$ symmetry and subsequently those regarding a symmetry operator that can be considered its generalisation, $\mathbb{Z}_n$. The spectrum of the superoperator $\mathcal{Z}_2 = \mathbb{Z}_2 \cdot \mathbb{Z}_2^\dagger$ (where the $\cdot$ is replaced with an operator such as the density matrix ρ) is composed by two eigenvalues ± 1, so that $\mathcal{Z}_2\rho_0 = \rho_0$ and $\mathcal{Z}_2\rho_1 = -\rho_1$. In the normal phase $\xi < \xi_c$, the steady state is unique and the only zero eigenvalue of $\mathcal{L}$ is $\lambda_0 = 0$ while $\mathcal{Z}_2\rho_{ss} = \rho_{ss}$. In the symmetry-broken phase, while the feature of $\lambda_0 = 0$ persists, also the Liouvillian

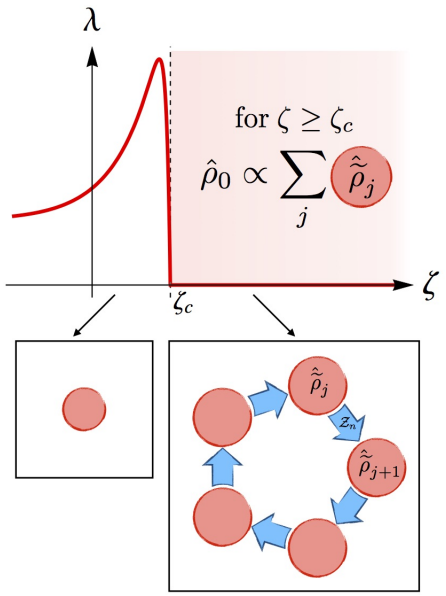

Fig. 2.4. Plot showing the absolute value of the Liouvillian gap λ as a function of the order parameter ξ. In the normal phase below threshold, the relaxation rate is finite and non-0 describing an absolutely stable and unique steady state. In the symmetry-broken phase, the gap closes throughout the entire region $\xi > \xi_c$ and the system is found in a superposition of ξ-dependent steady states. The symmetry superoperator acts as a map leading from the state $\tilde{\rho}_j$ to $\tilde{\rho}_{j+1}$ and so on. Reprinted figure from Ref. [109] with permission from F. Minganti *et al.*, Phys. Rev. A **98**, 042118, 2018. Copyright (2018) by the American Physical Society.

gap λ_1 vanishes and the system could be in any mixture of the two eigenmatrices of the symmetry superoperator $\mathcal{Z}_2$. As an example, the system could reach the following states:

$$\rho_{\pm} = \frac{\rho_0 \pm \rho_1}{\mathrm{Tr}[\rho_0]} \tag{2.64}$$

and these density matrices are symmetry-breaking steady states of the density matrix equation of motion. In addition, the symmetry superoperator can be seen as a map connecting one type of steady state with the other type, according to $\mathcal{Z}_2\rho_{\pm} = \rho_{\mp}$.

For a system with N finite, we remark that only one steady state is admitted, which obeys the symmetry, and that is

$$\rho_{ss}(\xi \geq \xi_c, N) \approx \frac{\rho_+(\xi \geq \xi_c, N) + \rho_-(\xi \geq \xi_c, N)}{2} \tag{2.65}$$

so that the resulting steady state density matrix $\rho_{ss}(\xi \geq \xi_c, N)$ has unit trace in virtue of

Eq.(2.64) and Eq.(2.60).

If we extend to the generic case $\mathcal{Z}_n = \mathbb{Z}_n \cdot \mathbb{Z}_n^\dagger$, the spectrum is given by $\lambda_j = e^{2i\pi j/n}$, where $j = 0, ..., n-1$ and the $\xi > \xi_c$ phase is characaterised by a set of eigenmatrices ρ_j that obey the conditions $\mathcal{L}\rho_j = 0$ and $\mathcal{Z}_n\rho_j = \lambda_j\rho_j$. As in the previous case, one can define a set of density matrices $\{\tilde{\rho}_i\}$ with $i = 0, ..., n-1$, superpositions of the eigenmatrices ρ_j, and where each $\tilde{\rho}_i$ is mapped to the $\tilde{\rho}_k$ by applying one or more times the symmetry superoperator $\mathcal{Z}_n$, according to

$$\tilde{\rho}_l = \mathcal{Z}_n^l \sum_{j=0}^{n-1} \frac{\rho_j}{\mathrm{Tr}[\rho_0]} = \sum_{j=0}^{n-1} \frac{\lambda_j^l \rho_j}{\mathrm{Tr}[\rho_0]} \tag{2.66}$$

and where this operation is graphically expressed in Fig.(2.4). Finally, as an extension of Eq.(2.65), for a finite size system, the unique steady state is given by

$$\rho_{ss}(\xi \geq \xi_c, N) \approx \sum_{l=0}^{n-1} \frac{\tilde{\rho}_l(\xi \geq \xi_c, N)}{n} \tag{2.67}$$

To make a connection with the case of a symmetry such as U(1), this could be seen as the limit $n \to +\infty$ of the symmetry operator $\mathbb{Z}_n$. As we have discussed above, the U(1) symmetry breaking process is often graphically represented by means of an energy landscape as a function of the order parameter, see Fig.(2.3). While, the evolution of the energy functional describes a symmetry breaking in the ground state of a Hamiltonian model, the evolution of the Liouvillian spectrum, specifically of the Liouvillian gap, represents the symmetry breaking process in the nonequilibrium steady state of a dissipative system. Nevertheless, the behavior of the system is similar in both cases: for values of the order parameter less than the critical value, a non-zero (real-valued) eigenvalue, indicating a net decay of the system towards the unique (symmetry-preserving) steady state (see Fig.(2.4)), is mirrored by the behaviour that small fluctuations of the order parameter will decay leading the system towards the unique (symmetry-preserving) ground state, see Fig.(2.3). For values of the order parameter greater than the critical value, the system enters a symmetry-broken phase identified by an extra vanishing eigenvalue (in addition to $\lambda_0 = 0$) and the emergence of multiple steady states, as shown in Fig.(2.4). This phenomenon is reflected by an analogous behavior in the energy landscape in Fig.(2.3) undergoing a transition to the typical Mexican hat shape which highlights the emergence of a valley composed by an

infinite number of minima (ground states) with 0 energy. In both pictures, the behavior above threshold is associated to the emergence of a Goldstone mode.

2.5 Mean field approximation and Cumulant expansion

In this section, we are going to discuss first a commonly used approach to describe phase transitions in light-matter systems, the mean-field approximation. While atomic systems collectively and identically coupled to single electromagnetic field modes, typically the fundamental $\mathrm{TEM}_{0,0}$, are well described by mean-field theory, light-matter systems in multimode regimes need beyond mean-field treatment because with multiple distinct photon modes, one has multiple channels for fluctuations, and this fact implies that their role in the dynamics becomes more relevant. To describe the effects involved in the system dynamical behavior due to the electromagnetic fields and their contribution, different methods can be employed [105, 126, 127, 128, 20, 16]. Among those, we are going to treat the cumulant expansion [129, 130, 131, 132, 20, 21, 16]. But before discussing this aspect, let us first focus on the mean-field approximation and its meaning.

Considering the scenario of an atomic ensemble coupled to the electromagnetic field in a cavity, the simplest configuration studied both in theory and in experiments consists in assuming all atoms uniformly interacting with a single electromagnetic mode, as discussed before. This assumption is adequate when the size of the atomic cloud is within a fraction of the wavelength of the light mode. This picture leads to the concept of cooperative atomic emission described by Dicke [1]. In that case, instead of dealing with many individual field-mediated atom-atom interactions, each atom can be thought as being influenced by an average field, generated by the behavior of all the other atoms. This fact formally means that when writing equations of motion for the atoms and the field, correlations between pairs or more atoms, as well as correlations between the field and atoms are neglected.

To formally introduce this concept, let us take any two observables, A and B. Then, neglecting correlations between A and B means that expectation values of products of these operators reduce to products of single operator expectation values, i.e.,

$$\langle\langle AB\rangle\rangle_C = \langle AB\rangle - \langle A\rangle\langle B\rangle = 0 \tag{2.68}$$

alternatively, $\langle AB\rangle = \langle A\rangle\langle B\rangle$. The left hand side of the above equation is the second

order cumulant and expresses the degree of correlation between the variables A and B. Assuming a vanishing cumulant means that the variables are uncorrelated and the mean value of the product can be expressed by the product of the mean values. Moreover, as well as setting the second cumulant to zero, all higher order cumulants are considered vanishing. This assumption is known as mean field approximation [115, 131]. As explained futher in the following, this can be regarded as the most basic level of approximation, or better, as the zeroth order of a perturbative expansion in the inverse of the number of particles N involved in the system.

While we have already discussed the Dicke model with only cavity dissipation, and the derivation of equations for the expectation values of photonic and spin operators where the mean field approximation is applied, in section 1.1, let us include additional decay processes, such as single-spin decays as well as atomic dephasing [20]. The dynamics is captured by

$$\dot{\rho} = -i[H, \rho] + \kappa \mathcal{D}[a] + \sum_i \gamma_\downarrow \mathcal{D}[\sigma_i^-] + \gamma_\phi \mathcal{D}[\sigma_i^z] \tag{2.69}$$

where H is given by Eq.(1.1). From Eq.(1.1) and Eq.(2.69), one can compute coupled equations of motion for the expectation values of atom and field operators:

$$\begin{aligned} \langle \dot{a} \rangle &= -(i\omega_c + \kappa)\langle a \rangle - i2g\sqrt{N}\langle \sigma^x \rangle \\ \langle \dot{\sigma}^+ \rangle &= (i\omega_z - \gamma_T)\langle \sigma^+ \rangle - \frac{2ig}{\sqrt{N}} \mathrm{Re}[\langle a\sigma^z \rangle] \end{aligned} \tag{2.70}$$

with $\gamma_T = \gamma_\phi + \gamma_\downarrow$. It is important to remember that when one includes processes occurring at the single-atom level, as those described by the rates $\gamma_\downarrow$ and γ_ϕ, the collective spin representation cannot be used due to the violation of the total spin length conservation law. As it is shown, Eq.(2.70) explicitly depends on the correlation $\langle a\sigma^z \rangle$. Therefore, one should include the equation governing the dynamics of that term as well. However, the inclusion of that equation implies that additional possibly higher order correlations may arise, and one would need to include equations for those terms. This fact evidently leads to an infinite set of coupled equations. By applying the rule in Eq.(2.68), one can reduce the correlation function as $\langle a\sigma^z \rangle = \langle a \rangle \langle \sigma^z \rangle$, thus providing a closed set of mean field equations. These equations are similar to the Maxwell-Bloch equations found in laser theory [2, 133, 134, 67]. It is relevant to stress that, the mean field version of Eq.(2.70), is

strictly valid in the limit of an infinite number of atoms $N \to \infty$. In this limit, corrections to the mean field solution of Eq.(2.70) scaling with the number as $1/N$ vanish. When the number N is finite and large, a more accurate description of the dynamics is reached by including two-operators correlation functions, i.e. assuming that together with the first order cumulant, the mean value, also the second order cumulant, or variance, is non zero, while for N finite and small, increasing order cumulants are to be accounted for.
As a general rule, when one wants to truncate the hierarchy at some order, say n, this means setting the corresponding $n+1$-th order cumulant to zero and express the $n+1$-th order correlation function as a combination of products of lower order correlations [131]. For most systems, mean field theory is sufficient to capture the behavior, but there are cases where beyond mean field corrections and, in particular, different levels of truncation in the cumulant expansion are required, depending on the characteristics of the environment [135]. In all cases, in the limit $N \to \infty$, the equations will tend to their mean-field version, meaning that each higher order correlation becomes a product of single-operator expectation values.
There are two issues to carefully analyse when one wants to work with a cumulant expansion:

1. the non-commutative nature of quantum operators in the expectation.

2. the probability distribution of the measurement outcomes of the observables.

Regarding 1), all models in QED involve non-commuting operators. In particular, if one considers the Dicke model and aims at writing beyond mean field equations, there can be cases involving expectations of two or more spin operators requiring some strategy in the decoupling procedure, since the standard rule [131] strictly holds for classical variables. As explained in the next chapter, re-ordering strings of spin operators exploiting the canonical commutation relations allows to cast the correlation function in a form where the decoupling rule for classical cumulants becomes possible [98].
The discussion about point 2) needs to be postponed to chapter 3 and 4, as the concept becomes clearer when discussing the actual problems.

Chapter 3

Atom-only theories for U(1) symmetric cavity-QED models

In chapter 1, we have introduced and discussed a class of Dicke models with U(1) symmetry (section 1.4), describing spins coupled to two cavity modes that undergo a spontaneous symmetry breaking phase transition to a superradiant state above a critical light-matter interaction strength. While, in chapter 2, in the framework of quantum systems coupled to an environment, we discussed what conditions are needed to trace out some degrees of freedom, in particular those of the environment, with the aim of studying the dynamics of the system only. We have also discussed the spectral features indicative of spontaneous symmetry breaking in dissipative open quantum systems.

Here, we are going to make use of the concepts introduced in those previous chapters. Specifically, we are going to formulate first a Redfield theory associated with the whole family of U(1)-symmetric models, where both cavity modes are traced out. We are then going to discuss the limitations of such formalism for the present class of problems. To advance our investigation, we will thus focus on a single model within that class and compute an higher order correction term in the density matrix equation, employing the diagrammatic expansion described in section 2.3. Once we have obtained the equation, we will assess the solutions and the eigenspectrum of the underlying Liouvillian dynamics, comparing the results with the predictions of the full atom-cavity problem.

3.1 Derivation of the Redfield theory for a class of U(1) Dicke models

We begin by recalling the class of generalised Dicke Hamiltonians with U(1) symmetry, Eq.(1.38), and the equation of the dynamics, Eq.(1.29):

$$\dot{\rho} = -i[H, \rho] + \kappa(\mathcal{D}[a] + \mathcal{D}[b]), \tag{3.1}$$

$$H = \omega_A a^\dagger a + \omega_B b^\dagger b + \omega_0 S^z + g\left[\left(a^\dagger + i\gamma b^\dagger\right) S^- + \left(b^\dagger + i\gamma a^\dagger\right) S^+ + \text{H.c.}\right]. \tag{3.2}$$

As a quick reminder, the above model describes a spin ensemble, represented by the collective operator $\mathbf{S} = (S^x, S^y, S^z)$, uniformly coupled to two photon modes of a cavity, a and b, whose frequency can be tuned to reach perfect degeneracy. The parameter γ spanning in the range $0 \leq \gamma \leq 1$ identifies the class of models with U(1) symmetry whose generators are presented in section 1.4 as well as their mean-field analysis.

As discussed, solving the multimode limit of the above models, accounting also for spatial structure of the TEM modes, represents a challenging task due to the exponential growth of Hilbert space dimension. Therefore, it is essential to restore to effective theories explicitly depending on a reduced number of degrees of freedom. Before focusing on such a complex model, it is appropriate to start from the above two-mode problem.

The derivation of such an effective theory lies on a specific condition. As discussed in a previous chapter (section 1.3), in experiments realizing light-matter couplings via Raman pumping, there is typically an overall distinction of energy scales between the atomic and field degrees of freedom, $\omega_{\text{cav}}, \kappa \gg \omega_0, g\sqrt{N}$, which allows for adiabatic elimination of faster cavity variables [90, 91]. We thus next consider how to eliminate the cavity degrees of freedom and get an equation of motion for the slower atomic variables.

An easier route for atom-only dynamical equations is perhaps to start from the equations of motion for the expectation values of atoms and fields, given in Eqs(1.39-1.42) that are

reproposed here for simplicity:

$$\begin{aligned}
\dot{\alpha} &= -\left(i\omega_A + \frac{\kappa}{2}\right)\alpha + g\left(\gamma S^+ - iS^-\right) \\
\dot{\beta} &= -\left(i\omega_B + \frac{\kappa}{2}\right)\beta + g\left(\gamma S^- - iS^+\right) \\
\dot{S}^+ &= i\omega_0 S^+ - 2g\left[i\left(\alpha^* + \beta\right) + \gamma\left(\alpha - \beta^*\right)\right] S^z \\
\dot{S}^z &= g\left\{\left[i\left(\alpha^* + \beta\right) + \gamma\left(\alpha - \beta^*\right)\right] S^- + c.c\right\}
\end{aligned} \tag{3.3}$$

Let us take the $\gamma = 0$ version of those equations as a reference. If we solve the first two equations for the steady states of the photon operators and substitute their values in the remaining equations for the spins, we find the following equation for the collective spin operator:

$$\dot{\mathbf{S}} = \{\mathbf{S}, H_{\text{eff}}\} \tag{3.4}$$

where, the braces $\{X, Y\}$ here describe Poisson brackets, since we are considering the classical dynamics of the spin vector S, and the effective Hamiltonian in the case $\omega_A = \omega_B = \omega$ is given by $H_{\text{eff}} = \omega_0 S^z + 2g^2\omega(S^z)^2/(\omega^2 + \kappa^2/4)$. The elimination of the field variables a and b from these mean field equations provides the wrong result, as Eq.(3.4) describes a purely Hamiltonian dynamics, missing the damped relaxation to the steady state due to dissipation. A similar result was observed in [91] for the single mode $\mathbb{Z}_2$ Dicke model. The case studied in [91] is in fact an example showing how eliminating faster field variables from semiclassical equations or within a formalism involving a quantum model, such as the Redfield theory, led to two significantly different outcomes, with the latter approach being successful in recovering dissipative dynamics.

Coming back to our two-mode problem, with the above finding, we need to change strategy and proceed by eliminating the cavity field from a full quantum model and then derive mean-field equations for the spins. To this end, the total Hamiltonian, Eq.(3.2), might be separated in an unperturbed part, H_0, plus the interaction term between atoms and cavity field, H_I, that is $H_{\text{Dicke}} = H_0 + H_I$. In the unperturbed part, we consider an expanded Hilbert space given by the inclusion of two external reservoirs of bosonic modes, A_k and

B_k. The expressions of H_0 and H_I are given by

$$H_0 = \omega_A a^\dagger a + \omega_B b^\dagger b + \omega_0 S^z + \sum_k \left[\mu_k A_k^\dagger A_k + \nu_k B_k^\dagger B_k + g_k \left(a^\dagger A_k + b^\dagger B_k + \text{H.c.}\right)\right] \tag{3.5}$$

$$H_I = g\left[\left(a^\dagger + i\gamma b^\dagger\right) S^- + \left(b^\dagger + i\gamma a^\dagger\right) S^+ + \text{H.c.}\right]. \tag{3.6}$$

where, in Eq.(3.5), the bosonic modes A_k and B_k satisfy canonical commutation relations of harmonic oscillators, with spectral density of the modes being given by $\sum_k g_k^2 \pi\delta(\nu_k - \nu) = \kappa/2$, and similarly for μ_k.

The equation of motion governing the atom dynamics can be accessed through the Redfield formula, Eq.(2.34) [90]

$$\dot{\rho}_t = -\int_0^t dt' Tr_B \left\{[H_I(t), [H_I(t'), \rho_t(t)]]\right\}, \tag{3.7}$$

where the trace is performed over the cavity variables and the coupling term between spins and fields, H_I, is in the interaction picture with respect to H_0

$$H_I(t) = g\left[S^+(t)X(t) + S^-(t)X^\dagger(t)\right]. \tag{3.8}$$

In the above expression, we separate the photonic, $X(t)$, from the matter component $S^\pm(t)$, with $X(t) = a(t) + b^\dagger(t) - i\gamma\left(b(t) - a^\dagger(t)\right)$ and $S^\pm(t) = S^\pm e^{\pm i\omega_0 t}$. The time integral can be solved by inserting the two-time correlations of cavity mode operators $\langle X(t)X(t')\rangle$, $\langle X^\dagger(t)X^\dagger(t')\rangle$, $\langle X(t)X^\dagger(t')\rangle$, $\langle X^\dagger(t)X(t')\rangle$ and another set with the same correlation functions where the time arguments are swapped. The explicit time-dependence of these correlations can be found by means of coupled Heisenberg-Langevin equations for the cavity (a, b) and the extra-cavity mode operators (A_k, B_k). We thus start by writing time-dependent equations for a and A_k; the same approach applies to b and B_k:

$$\begin{cases} \dot{a} = -i[a, \omega_A a^\dagger a + \sum_k g_k(a^\dagger A_k + \text{H.c.})] = -i\omega_A a - i\sum_k g_k A_k, \\ \dot{A}_k = -i[A_k, \mu_k A_k^\dagger A_k + g_k(a^\dagger A_k + \text{H.c.})] = -i\mu_k A_k - i g_k a \end{cases} \tag{3.9}$$

Solving Eq. (3.9) for A_k yields: $A_k(t) = A_k(0)e^{-i\mu_k t} - i g_k \int_0^t dt' e^{-i\mu_k(t-t')} a(t')$, and then

substituting in the equation for $\dot{a}$ leads to the following:

$$\dot{a} = -i\omega_A a - i\sum_k g_k A_k(0)e^{-i\mu_k t} - \sum_k g_k^2 \int_0^t dt' e^{-i\mu_k(t-t')}a(t'). \tag{3.10}$$

The density of states of the free-space modes, introduced earlier in this section, $\sum_k g_k^2 e^{-i\mu_k(t-t')} = \frac{\kappa}{2}\delta(t-t')$ will be used to further simplify Eq.(3.10), together with the identification of a stochastic force $\xi_A(t)$ in the second term of Eq.(3.10). This stochastic force is a white noise term, described by the following properties: $\langle \xi_A(t)\rangle = 0$, $\langle \xi_A(t)\xi_A^\dagger(t')\rangle = \delta(t-t')$. Therefore Eq.(3.10) can be written as,

$$\dot{a} = -i\omega_A a + \xi_A(t) - \int_0^t dt' \frac{\kappa}{2}\delta(t-t')a(t'). \tag{3.11}$$

We note that with the identification $\xi_A(t) = -i\sum_k g_k A_k(0)e^{-i\mu_k t}$, the relations below follow

$$\begin{cases} \langle \xi_A(t)\xi_A^\dagger(t')\rangle = \sum_k g_k^2 e^{-i\mu_k(t-t')}\langle A_k(0)A_k^\dagger(0)\rangle, \\ \langle \xi_A^\dagger(t')\xi_A(t)\rangle = \sum_k g_k^2 e^{-i\mu_k(t-t')}\langle A_k^\dagger(0)A_k(0)\rangle, \end{cases} \tag{3.12}$$

and Eq.(3.12) imply that the two-time commutator of ξ_A yields the density of states of the external environment, namely,

$$[\xi_A(t), \xi_A^\dagger(t')] = \sum_k g_k^2 e^{-i\mu_k(t-t')}[A_k(0), A_k^\dagger(0)] = \frac{\kappa}{2}\delta(t-t'). \tag{3.13}$$

Therefore, after the above considerations, Eq.(3.10) becomes:

$$\dot{a} + \left(i\omega_A + \frac{\kappa}{2}\right)a = \xi_A(t), \tag{3.14}$$

whose complete solution is given by:

$$a(t) = a(0)e^{-\left(i\omega_A + \frac{\kappa}{2}\right)t} + \int_0^t dt' e^{-\left(i\omega_A+\frac{\kappa}{2}\right)(t-t')}\xi_A(t'). \tag{3.15}$$

In the limit $t \to \infty$, the homogeneous solution in the above expression vanishes, leaving the integral term. Thus, we finally have all the ingredients to evaluate the two-time correlation

of cavity operator a:

$$\begin{aligned}\langle a(t)a^\dagger(t')\rangle &= \int_0^t d\tau \int_0^{t'} d\tau' e^{-\left(i\omega_A+\frac{\kappa}{2}\right)(t-\tau)} e^{\left(i\omega_A-\frac{\kappa}{2}\right)(t'-\tau')} \langle \xi_A(\tau)\xi_A^\dagger(\tau')\rangle \\ &= \frac{\kappa}{2}\int_0^{\min(t,t')} d\tau e^{-i\omega_A(t-t')-\frac{\kappa}{2}(t+t'-2\tau)} = e^{-i\omega_A(t-t')-\frac{\kappa}{2}|t-t'|},\end{aligned} \tag{3.16}$$

where the property $\langle \xi_A(\tau)\xi_A^\dagger(\tau')\rangle = \frac{\kappa}{2}\delta(t-t')$ is used on the first line of Eq.(3.16) and the decaying behavior over time results from the upper limit of the integral, $\min(t,t')$, namely:

$$t+t'-2\min(t,t') = \begin{cases} t+t'-2t' = t-t' & t > t' \\ t+t'-2t = t'-t & t < t' \end{cases} \tag{3.17}$$

The same approach allows to find two-time correlations for cavity mode b. Summarising, the following expressions are essential to compute Eq.(3.7), together with the time-dependence of the raising/lowering spin operators $S^\pm = S^\pm e^{\pm i\omega_0 t}$:

$$\begin{cases} \langle a(t)a^\dagger(t')\rangle = e^{-i\omega_A(t-t')-\frac{\kappa}{2}|t-t'|} \\ \langle b(t)b^\dagger(t')\rangle = e^{-i\omega_B(t-t')-\frac{\kappa}{2}|t-t'|} \end{cases} \tag{3.18}$$

These and similar terms with time arguments swapped are the only terms we care about, as mixed $\langle ab\rangle$ correlators are neglected because the cavity modes are non-interacting and $\langle a^\dagger(t)a(t')\rangle = \langle b^\dagger(t)b(t')\rangle = 0$ when calculated on the vacuum state of the cavity modes. Thus, upon substituting the form of the interaction Eq.(3.8) in Eq.(3.7) and performing cyclic permutations on the photonic operators X, we end up with the following combinations of cavity mode correlations

$$\begin{cases} \langle X(t)X(t')\rangle = i\gamma\left(\langle a(t)a^\dagger(t')\rangle - \langle b(t)b^\dagger(t')\rangle\right) \\ \langle X^\dagger(t)X^\dagger(t')\rangle = i\gamma\left(\langle b(t)b^\dagger(t')\rangle - \langle a(t)a^\dagger(t')\rangle\right) \\ \langle X(t)X^\dagger(t')\rangle = \langle a(t)a^\dagger(t')\rangle + \gamma^2\langle b(t)b^\dagger(t')\rangle \\ \langle X^\dagger(t)X(t')\rangle = \langle b(t)b^\dagger(t')\rangle + \gamma^2\langle a(t)a^\dagger(t')\rangle \end{cases} \tag{3.19}$$

where, for convenience, we recall that, in the Born-Markov approximation, the to-

tal system $\rho_t = \rho(t) \otimes \rho_B$ is in a fully separable state (see Eq.(2.32)), so that the above expectation values are measurements on the state of the environment, namely $\langle O(t)O(t')\rangle = \mathrm{Tr}_B\left[O(t)O(t')\rho_B\right]$. By finally inserting Eq.(3.19) in Eq.(3.7) and pushing the lower limit of the integral to $-\infty$, the Redfield master equation can be easily computed, yielding the following expression in the Schroedinger picture

$$\begin{aligned}\dot{\rho} = -2g^2 \Big[& i\gamma \left(Q_+^A - Q_+^B\right)\left(S^+S^+\rho - S^+\rho S^+\right) + i\gamma\left(Q_-^B - Q_-^A\right)\left(S^-S^-\rho - S^-\rho S^-\right) + \\ & \left(Q_+^B + \gamma^2 Q_+^A\right)\left(S^-S^+\rho - S^+\rho S^-\right) + \left(Q_-^A + \gamma^2 Q_-^B\right)\left(S^+S^-\rho - S^-\rho S^+\right) + \\ & i\gamma\left(Q_-^{A*} - Q_-^{B*}\right)\left(\rho S^+S^+ - S^+\rho S^+\right) + i\gamma\left(Q_+^{B*} - Q_+^{A*}\right)\left(\rho S^-S^- - S^-\rho S^-\right) + \\ & \left(Q_+^{B*} + \gamma^2 Q_+^{A*}\right)\left(\rho S^-S^+ - S^+\rho S^-\right) + \left(Q_-^{A*} + \gamma^2 Q_-^{B*}\right)\left(\rho S^+S^- - S^-\rho S^+\right)\Big] + \\ & - i\omega_0\left[S^z, \rho\right],\end{aligned} \tag{3.20}$$

where $Q_\pm^{A(B)} = \frac{1}{\kappa + 2i\left(\omega_{A(B)} \pm \omega_0\right)}$ are rates associates to the spin-flip processes and the (*) indicates the complex conjugate of those coefficients.

Equation (3.20) has a non secularised form since it explicitly includes terms oscillating fast in the interaction picture, namely $S^{+2}(t) = S^{+2}e^{2i\omega_0 t}$ and $S^{-2}(t) = S^{-2}e^{-2i\omega_0 t}$. As a note, non secularised master equations cannot typically achieve a Lindblad form. However, in [91] it is shown that secularising the density matrix equation of motion to obtain a Lindblad form prevents from observing the $\mathbb{Z}_2$ breaking phase transition of the Dicke model, while the non secularised form provides an accurate description.

In the next section, we will derive mean field equations from Eq.(3.20) and conduct a preliminary analysis on the stability phase diagram, comparing it with the complete atom-field problem.

3.1.1 Mean-field EOM and linear stability analysis

An effective reduced theory must fulfill some requirements to be reliable and a robust alternative to its full model: it must be Hermitian, trace-preserving and preserve the symmetry of the problem. Eq.(3.20) satisfies all of the above conditions, thus allowing to compute the time evolution of the expectation value of any observable $\hat{A}$ of the system, as $\langle \dot{A}\rangle = Tr\left[\dot{\rho}A\right]$. Being a reduced description for the atomic degrees of freedom only,

it will be sufficient to compute equations of motion for $\langle S^\alpha \rangle$ with $\alpha = z, \pm$. The general form of these equations is given by:

$$\begin{aligned}\left\langle \dot{S}^z \right\rangle = -2g^2 \Big\langle & Q_+^A \left(i\gamma S^+ S^+ - \gamma^2 S^- S^+ \right) - Q_+^B \left(i\gamma S^+ S^+ + S^- S^+ \right) + \\ & Q_-^A \left(i\gamma S^- S^- + S^+ S^- \right) + -Q_-^B \left(i\gamma S^- S^- - \gamma^2 S^+ S^- \right) - \\ & Q_-^{A*} \left(i\gamma S^+ S^+ - S^+ S^- \right) + Q_-^{B*} \left(i\gamma S^+ S^+ + \gamma^2 S^+ S^- \right) \\ & -Q_+^{A*} \left(i\gamma S^- S^- + \gamma^2 S^- S^+ \right) + Q_+^{B*} \left(i\gamma S^- S^- - S^- S^+ \right) \Big\rangle, \end{aligned} \tag{3.21}$$

$$\begin{aligned}\left\langle \dot{S}^- \right\rangle = -i\omega_0 \left\langle S^- \right\rangle - 2g^2 \Big\langle & 2i\gamma S^z S^+ \left(Q_+^B - Q_+^A \right) - 2S^z S^- \left(Q_-^A + \gamma^2 Q_-^B \right) \\ & +2i\gamma S^+ S^z \left(Q_-^{A*} - Q_-^{B*} \right) + 2S^- S^z \left(Q_+^{B*} + \gamma^2 Q_+^{A*} \right) \Big\rangle, \end{aligned} \tag{3.22}$$

where the equation for S^+ is simply obtained by Hermitian conjugation of that for S^-.

To get a closed set of equations of motion, we make the mean field ansatz. Firstly, we assume no correlations between the spins, meaning that a mean-field decoupling of two-spin correlations in products of single expectation values $\langle S^\alpha S^\beta \rangle = \langle S^\alpha \rangle \langle S^\beta \rangle$ is performed. This operation corresponds to setting the second order cumulant of the spin operators equal to 0, $\langle S^\alpha S^\beta \rangle_C = \langle S^\alpha S^\beta \rangle - \langle S^\alpha \rangle \langle S^\beta \rangle = 0$. To analyze the stability of the phases of the system with the variation of the model parameters, one procedure typically adopted is the linearization of the equations of motion around a specific steady state attractor. We perturb the steady state solution, $\langle S^\alpha \rangle_{SS}$, by adding a fluctuation term $\delta S^\alpha = a e^{i\lambda t} + b^* e^{-i\lambda^* t}$, expressed by a complex-valued parameter λ (if the operator is real, $a = b$ is required). According to this specific definition for the perturbation, the imaginary part of λ, and particularly its sign, reveals the nature of the fluctuation. Specifically, the sign of $\mathrm{Im}(\lambda)$ reveals whether the perturbation will grow ($\mathrm{Im}(\lambda < 0)$), indicating an unstable steady state, or decay exponentially ($\mathrm{Im}(\lambda \geq 0)$), signaling a stable solution. The behavior depends on the matter-light coupling strength g for the regime of parameters chosen, according to Eq.(1.13).

The replacement of expressions of the form $\langle S^\alpha \rangle = \langle S^\alpha \rangle_{SS} + \delta S^\alpha$, for the spin variables $\langle S^z \rangle$ and $\langle S^\pm \rangle$ in Eqs.(3.21-3.22) then provides an eigenvalue problem in the parameter λ. In the following, we analyse linear stability of the normal and inverted state, $\langle S^z \rangle_{SS} = \mp N/2$, $\langle S^\pm \rangle_{SS} = 0$, by studying the change of sign in the imaginary part of the eigenvalues of the

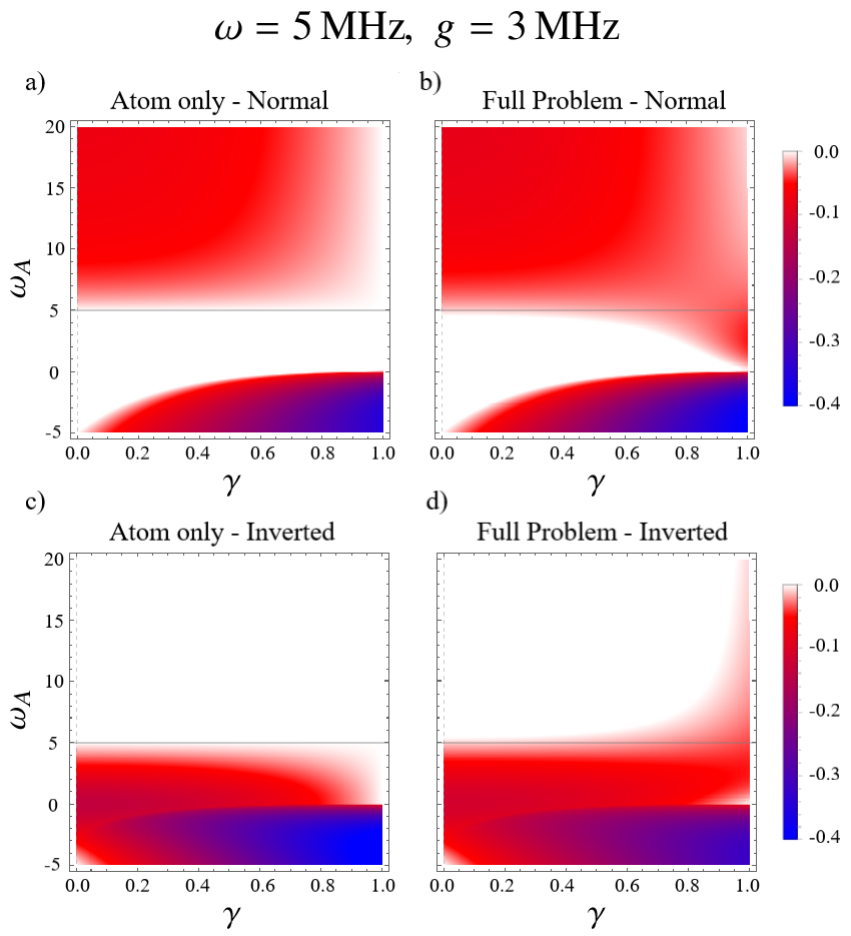

Fig. 3.1. Linear stability diagram of the normal and inverted state evaluated from the atom-only and full problem. All diagrams are obtained by fixing the value of detuning of one mode and the coupling strength above threshold ($g_c = 2$ kHz) while spanning over γ and a range of detunings of the second mode. The color scale is chosen so that $\mathrm{Im}(\lambda) = 0$ and $\mathrm{Im}(\lambda) > 0$ (i.e. stable states) are shown in white, while the red/blue regions indicate $\mathrm{Im}(\lambda) < 0$ (instability). The grey line identifies the class of models describing degenerate modes, $\omega_A = \omega_B = 5$ MHz. Parameters of the system are $\kappa = 8.1$ MHz, $\omega_0 = 47$ kHz and $N = 10^5$ atoms.

following matrix:

$$\begin{pmatrix} \omega_0 - iN\epsilon & -\gamma N\chi \\ \gamma N\chi^* & -(\omega_0 + iN\epsilon^*) \end{pmatrix}, \tag{3.23}$$

where $\epsilon = 2g^2\left(Q_+^A\gamma^2 + Q_+^B - Q_-^{A*} - Q_-^{B*}\gamma^2\right)$ and $\chi = 2g^2\left(Q_-^A - Q_-^B - Q_+^{A*} + Q_+^{B*}\right)$. The

eigenvalues are given by:

$$\lambda_{1,2} = \frac{1}{2}\left[z - z^* \pm \sqrt{z^2 + z^{*2} + 2|z|^2 - 4|\xi|^2}\right], \tag{3.24}$$

where, for brevity, $z = \omega_0 - iN\epsilon$ and $\xi = \gamma N\chi$. The imaginary part of these eigenfrequencies can be studied as a function of the cavity detuning and the parameter γ spanning the family of U(1)-symmetric models. Figure (3.1) shows the comparison between the linear stability diagrams of the normal and inverted state described by the two theories (atom-only and full model of Eq.(3.3)) in the region of parameters spanned by γ and cavity detuning. If we focus either on the normal, panel a) and b), or the inverted phase, panel c) and d), of Fig.(3.1), while the atom only and full problem show matching results in regions away from perfect mode degeneracy and for values of γ in $(0, 0.5)$ roughly, substantial differences emerge outside those parameter regions. For example, selecting the stability diagrams of the normal state in the limit of degenerate cavity modes $\omega_A = \omega_B$ (grey line), the atom only theory Eq.(3.20) predicts a stable normal state for all values of γ, while the full atom-field problem [17] reveals an unstable normal state in the same region. Moreover, away from the grey line in Fig.(3.1), in the region $0 < \omega_A < 5$ and $0.6 < \gamma < 1$, the Redfield theory Eq.(3.20) fails to match the results of the coupled light-matter problem, while an agreement is found in the range of small γ. The same observations apply to the analysis of the inverted state. This different behavior occurring in the small and large γ regions could be attributed to the validity conditions of the Redfield theory that start to break down away from the weak coupling limit, here in the region of larger γ.

As discussed, the most striking difference occurs in the proximity of the degeneracy line in Fig.(3.1), where for the value of light-matter coupling chosen, the system is supposed to be in the superradiant phase. The Redfield theory provides instead a picture with all spins either pointing down in the z axis, thus being in the normal state $S^z = -N/2$ or pointing up, thus in the inverted state $S^z = +N/2$. This observation is supported by a complementary analysis of the solution of Eq.(3.20), as we discuss in the next section.

3.1.2 2^{nd} order Redfield theory of the $\gamma = 0$ Dicke model

As anticipated, here we expand the previous results on the linear stability phase diagram with an analysis on the behavior of the steady state predicted by the Redfield equation

Eq.(3.20), as one vary the atom-photon coupling. We select and discuss the $\gamma = 0$ model of the family of Hamiltonians with U(1) symmetry. This choice is justified by the fact that studying such a model allows to capture all essential features of the family and, at the same time, it has the simplest interaction structure to compute a Redfield master equation. As for the procedure described in section 3.1, we begin by reporting the two-mode model along with the equation of motion of the composite light-matter system:

$$\dot{\rho}_t = -i\left[H, \rho_t\right] + \frac{\kappa}{2}\left(\mathcal{L}\left[a\right] + \mathcal{L}\left[b\right]\right), \tag{3.25}$$

$$H = \omega_A a^\dagger a + \omega_B b^\dagger b + \omega_0 S^z + g\left[\left(a^\dagger + b\right)S^- + \text{H.c.}\right]. \tag{3.26}$$

With regard to the interaction term, this describes a co-rotating coupling with one mode, here a, and a counter-rotating coupling with the other, b. As shown in [17], this configuration realises a U(1) symmetry and the resulting model becomes invariant under a transformation U such as $\rho \rightarrow U\rho U^\dagger$, with:

$$U = \exp\left[i\theta(S^z + a^\dagger a - b^\dagger b)\right], \tag{3.27}$$

which transforms atom and cavity operators as follows, $(a, b, S^\pm) \rightarrow (ae^{i\theta}, be^{-i\theta}, S^\pm e^{\mp i\theta})$. A Redfield theory in the present case is readily obtained by means of Eq.(3.25) and Eq.(3.26), knowing the analytical form of the cavity correlations, Eq.(3.18), or equivalently by setting $\gamma = 0$ in Eq.(3.20), yielding:

$$\begin{aligned}\dot{\rho} = -2g^2 \Big[&Q_-^A\left(S^+S^-\rho - S^-\rho S^+\right) + Q_-^{A*}\left(\rho S^+S^- - S^-\rho S^+\right) + \\ &Q_+^B\left(S^-S^+\rho - S^+\rho S^-\right) + Q_+^{B*}\left(\rho S^-S^+ - S^+\rho S^-\right)\Big] - i\omega_0\left[S^z, \rho\right].\end{aligned} \tag{3.28}$$

In this case, to derive the equation above, the number of two-time correlations of cavity mode operators reduces to $\langle\hat{X}(t)\hat{X}^\dagger(t')\rangle$, $\langle\hat{X}^\dagger(t)\hat{X}(t')\rangle$ and the same expectations with inverted time arguments.

As observed in the conclusions of section 3.1, at a fixed value of coupling g, the Redfield theory describes atomic spins all polarised in the normal/inverted state whereas the complete model of Ref.[17] predicts a superradiant state, see Fig.(3.1). It thus appears that the Redfield equation misses a transition to the superradiant phase of the model. If

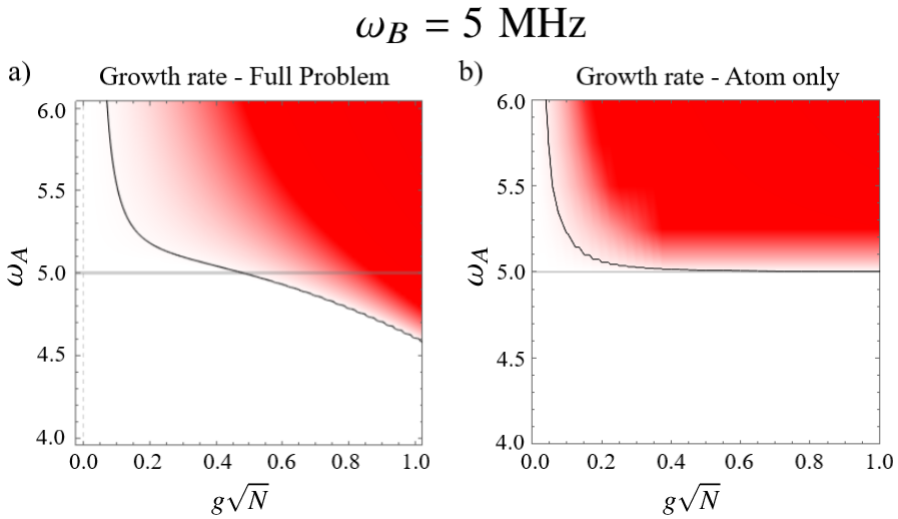

Fig. 3.2. Linear stability diagram of the normal state evaluated from the atom-only and full atom photon problem for the $\gamma = 0$ Dicke model. Here the horizontal axis represents the span over $g\sqrt{N}$ and the grey line identifies the degeneracy line, $\omega_A = \omega_B = 5$ MHz. The black line defining the contour between regions of stability of the phases: white (normal), red (superradiant). Following the grey line across the $g\sqrt{N}$ range, the system undergoes a phase transition at $g\sqrt{N} = 0.44$ MHz according to the full problem [17] while it stays in the normal state according to the atom-only theory. Parameters of the system are $\kappa = 8.1$ MHz and $\omega_0 = 47$ kHz.

we restrict the linear stability analysis to the $\gamma = 0$ model and study the evolution of the phase diagram with the light-matter coupling $g\sqrt{N}$, we would find the results shown in Fig.(3.2). Let us follow the degeneracy line $\omega_A = \omega_B$ across the entire $g\sqrt{N}$ range. From the comparison with the complete atom-photon problem, it is clear that the full problem indicates a transition from normal to superradiant phase highlighted by the change of stability of the normal state, while the atom only theory does not show the same result.

To show that the lack of transition is not just a feature of mean field theory but it is true of the full quantum state of the Redfield theory, it is useful to express it in Lindblad form:

$$\dot{\rho} = -i[H_{2\mathrm{RE}}, \rho] + 4g^2 \left(\mathrm{Re}[Q_-]\mathcal{L}[S^-] + \mathrm{Re}[Q_+]\mathcal{L}[S^+]\right), \tag{3.29}$$

where $Q_- = Q_-^A$, $Q_+ = Q_+^B$, and $H_{2\mathrm{RE}} = \omega_0 S^z + 2g^2(\mathrm{Im}[Q_-]S^+S^- + \mathrm{Im}[Q_+]S^-S^+)$ commutes with S^z and is thus diagonal in the basis of S^z. It is worth noting that in this case, the Redfield theory is automatically of Lindblad form, without the need for secularisation. It is useful to remind here that once fixed the number of atoms N, the

total spin is $S = N/2$ and the manifold of states that the atoms can populate during their dynamics is represented by the basis $|SM\rangle$ of the eigenstates of the operator S^z with eigenvalues $M = -S, ..., S$, that is $S^z |M\rangle = M |M\rangle$. Because of the U(1) symmetry, the steady state is diagonal in the S^z basis and this implies $\rho = \sum_M P_M |M\rangle \langle M|$, where $P_M = \rho_{MM}$ are the diagonal elements of the density matrix. At this point, if one writes the equation of the dynamics of the diagonal elements P_M of ρ, taking the reference equation (3.28), the following equation is found:

$$\dot{P}_M = 4g^2 \left\{ Q'_- \left[\left(f^M\right)^2 P_{M+1} - \left(f^{M-1}\right)^2 P_M \right] + Q'_+ \left[\left(f^{M-1}\right)^2 P_{M-1} - \left(f^M\right)^2 P_M \right] \right\}, \tag{3.30}$$

where $f^M = \sqrt{(S-M)(S+M+1)}$ represents the action of the ladder spin operators and the primed prefactors are the real parts of the corresponding rates of spin-flip processes, $Q'_\pm = \mathrm{Re}[Q_\pm]$. Solving for the steady state Eq.(3.30), we see that the ratio of the populations of two levels such as M and $M+1$ is given by $P_M/P_{M+1} = \mathrm{Re}[Q_-]/\mathrm{Re}[Q_+]$ but that expression lacks an explicit dependence on g, unique indicator of the onset of the transition at $g = g_c$. Furthermore, at large N the system is always found either in the normal state $\langle S^z \rangle = -N/2$ for $\mathrm{Re}[Q_-] > \mathrm{Re}[Q_+]$, or the inverted state $\langle S^z \rangle = +N/2$ if $\mathrm{Re}[Q_-] < \mathrm{Re}[Q_+]$, but no intermediate values of S^z can be reached when increasing the coupling strength.

There are two aspects behind the absence of a phase transition in this reduced theory. First of all, the U(1) symmetry implies that both the steady state and the effective Hamiltonian $H_{2\mathrm{RE}}$ always commute with S^z; therefore the state of the system depends on the dissipative terms only. The second point is that each term in the dissipators equally depends on g^2 so that the ratio of populations of two magnetic levels M,$M \pm 1$ has no surviving g dependence to trigger the phase transition.

In conclusion, while Eq.(3.20) associated with the general class of U(1) models and its particular $\gamma = 0$ case contemplate clear dissipative effects, in contrast to Eq.(3.4) obtained eliminating the cavity from the mean field equations, they do not recover a g-dependent phase transition. An important aspect to keep in mind for the discussions that will follow in the chapter is that standard Redfield theory predicts correct critical behavior in the case of the $\mathbb{Z}_2$ Dicke model [91].

In the following, we will analyse an higher order contribution to the equation of motion of the reduced density operator by means of the diagrammatic technique described in section 2.3.

3.2 Derivation of 4^{th} order Keldysh-Redfield theory:$\gamma = 0$

The previous sections have shown how a second order Redfield theory misses a symmetry-breaking phase transition in a class of generalised two-mode Dicke models with U(1) symmetry in both the mean field dynamics and its quantum solution. Before proceeding, it is important at this stage to stress that the Redfield theory is supported by assumptions such as a weak coupling between the system under consideration, the atoms, and the environment to be eliminated, the cavity modes. Moreover, in experiments it is typically observed a certain degree of separation between the timescales governing the atom and cavity dynamics, $\kappa \gg g\sqrt{N}, \omega_0$. Therefore, under these assumptions, one derives a Redfield equation considering the coupling parameter g as a perturbative parameter and, in this framework, Eq.(3.20) represents the second order of a perturbative expansion in g.

Once outlined those premises, in order to shed light on the reasons why Eq.(3.20) or its particular case Eq.(3.28) fail to recover the superradiance phase transition, we decide to go beyond the second order Redfield equation. To this aim, we will make use of the approach based on Keldysh diagrams [99], introduced and discussed in section 2.3. We are going to derive the next leading order term, the fourth order, and here we briefly recall the basic concepts needed for this derivation.

As a quick reminder, the technique is a time-dependent perturbation theory where each order of the expansion is graphically represented by a set of irreducible Keldysh diagrams. Writing the Dyson expansion with these diagrams as a reference guarantees that the resulting density-matrix equation accounts for all essential terms at a given order, avoiding any double counting of contributions.

In order to evaluate the state of the system density matrix, we have to solve Eq.(2.52) that we report here in the interaction picture:

$$\dot{\rho}(t) = \int_{t_0}^{t} dt_1 \rho(t_1) \Sigma(t_1, t), \tag{3.31}$$

where $\Sigma(t_1, t)$ is the self-energy superoperator that can be identified with the complete set of irreducible diagrams, some of which are shown in Fig.(2.2). Importantly, diagrams, such as those drawn in Fig.(2.2) or Fig.(3.4), are said irreducible because they correspond to true second and fourth order processes, respectively, as they cannot be reduced to products of lower order contributions. The Keldysh approach is used to evaluate the density matrix equation of the atoms up to fourth order finding first $\Sigma(t_1, t)$ up to that order, and then assuming a Markov approximation where $\rho(t_1) \simeq \rho(t)$ to get a time-local equation of motion for ρ.

We recall that, at a given order, each diagrammatic contribution to the self-energy is represented by two horizontal solid lines corresponding to the system evolving freely. These branches enclose the density matrix from the left (bottom line) and the right (top line). Then, a number of vertices, shown as purple dots on the solid lines, equal to the perturbative order being considered (n vertices at nth order) represents the number of time instants at which the interaction Hamiltonian, H_I, acts on the state of the system. Finally, dashed lines connecting pairs of vertices are interpreted as pairwise correlations of the environment (cavity modes), encoding the application of Wick's theorem.

What has been said is the overall meaning of a diagram without further specification about the form of the system-environment interaction. As we have seen in section 2.3, the application of a specific model, as Eq.(3.8), with well defined two-time correlations Eq.(3.19), determines the configurations of system operators assigned to those vertices connected by a dashed line (representing the two-time correlations) in each diagram. In the specific $\gamma = 0$ model, that observation would mean that only opposite spin operators $S^{\pm}$ are allowed if they are connected by dashed lines, according to Eqs.(3.18-3.19).

At fourth order in the expansion, there are 32 irreducible diagrams, with the first 16 displayed in Fig.(3.3). Because of the properties of the model we are considering, each diagram is translated into 4 contributions to the density matrix equation due to the fact that there are only 4 ways in which opposite spin operators can be distributed among the interaction vertices. This rule concerns with the $\gamma = 0$ Dicke model under study and it can change when analysing other light-matter models. The kind of integral one needs to

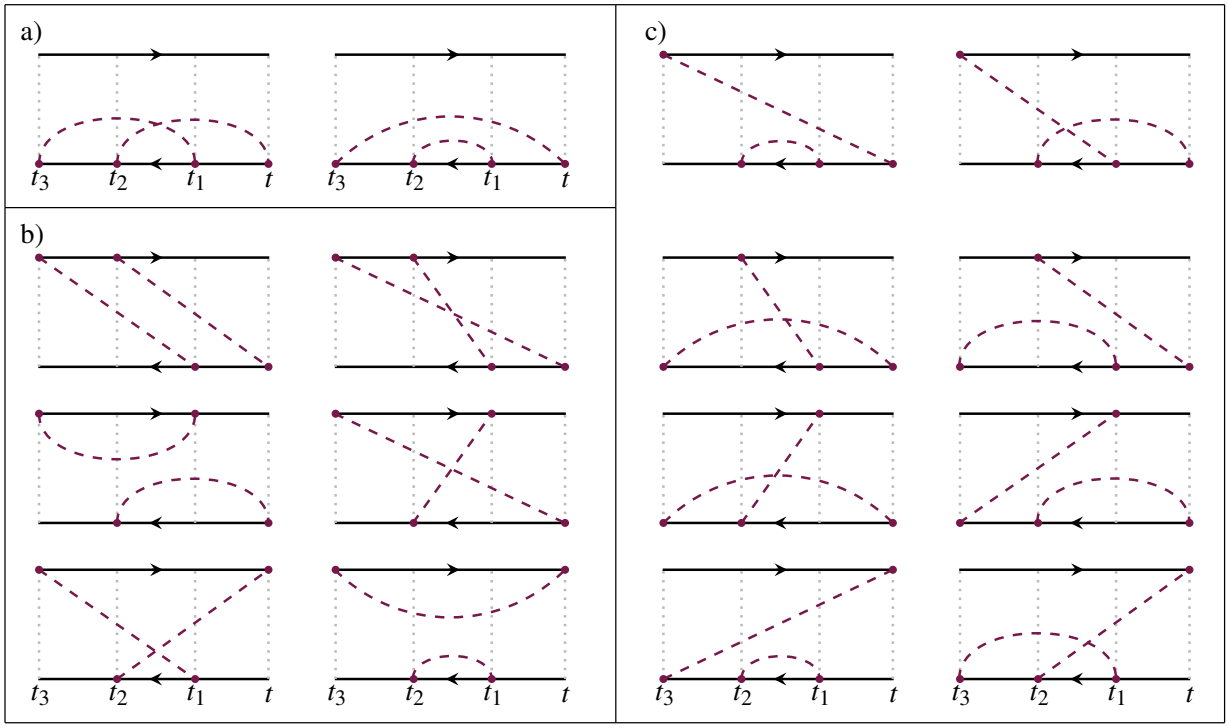

Fig. 3.3. 16 Keldysh diagrams at 4^{th} order. These are distributed in three groups (a,b,c) depending on the number of vertices on the bottom and top branch. The remaining 16 diagrams are obtained by swapping the vertices between the two lines. Reprinted figure with permission from R. Palacino and J. Keeling, Phys. Rev. Research **3**, L032016, 2021. Copyright (2021) by the American Physical Society.

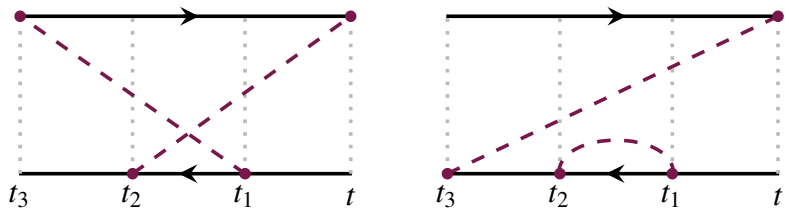

Fig. 3.4. A selection of diagrams at 4^{th} order. Reprinted figure with permission from R. Palacino and J. Keeling, Phys. Rev. Research **3**, L032016, 2021. Copyright (2021) by the American Physical Society.

solve within such a fourth order expansion is of the form:

$$\mathcal{L}^4\rho = Tr_B\left[\int_0^t dt_1\int_0^{t_1} dt_2\int_0^{t_2} dt_3 H_I(t_1)H_I(t_2)\rho(t_3)H_I(t_3)H_I(t)\right] \tag{3.32}$$

$$\mathcal{L}^4\rho = Tr_B\left[\int_0^t dt_1\int_0^{t_1} dt_2\int_0^{t_2} dt_3 H_I(t_1)H_I(t_2)H_I(t_3)\rho(t_3)H_I(t)\right]. \tag{3.33}$$

The first expression above refers to the left diagram in Fig.(3.4) while Eq.(3.33) corresponds to diagram on the right. As it emerges from the comparison of Eqs.(3.32-3.33) with Fig.(3.4), the number of vertices appearing on the lower (upper) branch of the path corresponds to the same number of interactions acting on the left (right) of ρ. H_I is the atom-cavity interaction extracted from Eq.(3.26) in the interaction picture:

$$H_I(t) = g\left[a^\dagger(t)S^-(t) + b(t)S^-(t) + \text{H.c.}\right], \tag{3.34}$$

and t_1, t_2, t_3 are dummy integration variables used to trace out the cavity degrees of freedom. Invoking the expressions of the cavity mode correlations, Eq.(3.18), and knowing that $S^\pm(t) = S^\pm e^{\pm i\omega_0 t}$, we can compute the terms corresponding to the diagrams in Fig.(3.4) as practical examples. These are given below in the Schroedinger picture,

$$\begin{aligned}&|Q_-|^2\kappa^{-1}S^-S^-\rho S^+S^+ + |Q_+|^2\kappa^{-1}S^+S^+\rho S^-S^- + Q_-Q_+^*Q_\Delta S^+S^-\rho S^-S^+ + Q_-^*Q_+Q_\Delta^* S^-S^+\rho S^+S^-\\ &- Q_+^2Q_\Sigma S^+S^-S^+\rho S^- - Q_-^2Q_\Sigma S^-S^+S^-\rho S^+ - Q_-^3S^+S^-S^-\rho S^+ - Q_+^3S^-S^+S^+\rho S^-,\end{aligned} \tag{3.35}$$

where we have used $Q_\mp = \left[\kappa + 2i\left(\omega_{A(B)} \mp \omega_0\right)\right]^{-1}$, $Q_\Sigma = \left[\kappa + i\left(\omega_A + \omega_B\right)\right]^{-1}$, $Q_\Delta = \left[\kappa + i\left(\omega_A - \omega_B - 2\omega_0\right)\right]^{-1}$. Repeating the procedure for all the other diagrams, we find

the complete form of the fourth order contribution to the density matrix equation:

$$
\begin{aligned}
\mathcal{L}^{(4)}\rho = 4g^4\Big[& Q_-^3\big(2S^-S^-\rho S^+S^+ + 2S^+S^+S^-S^-\rho - 4S^+S^-S^-\rho S^+\big)+ \\
& Q_+^3\big(2S^+S^+\rho S^-S^- + 2S^-S^-S^+S^+\rho - 4S^-S^+S^+\rho S^-\big)+ \\
& Q_-Q_+Q_\Sigma\big(S^+S^-\rho S^+S^- + S^-S^+\rho S^-S^+ + S^+S^-S^-S^+\rho + S^-S^+S^+S^-\rho + \\
& \qquad - S^+S^-S^+\rho S^- - S^-S^+S^-\rho S^+ - S^-S^-S^+\rho S^+ - S^+S^+S^-\rho S^-\big)+ \\
& Q_-^2Q_\Sigma\big(S^+S^-S^+S^-\rho + S^+S^-\rho S^-S^+ - S^+S^+S^-\rho S^- - S^-S^+S^-\rho S^+\big)+ \\
& Q_+^2Q_\Sigma\big(S^-S^+S^-S^+\rho + S^-S^+\rho S^+S^- - S^-S^-S^+\rho S^+ - S^+S^-S^+\rho S^-\big)+ \\
& \frac{|Q_-|^2}{\kappa}\big(S^+S^-\rho S^+S^- + S^-S^-\rho S^+S^+ - S^+S^-S^-\rho S^+ - S^-S^+S^-\rho S^+\big)+ \\
& \frac{|Q_+|^2}{\kappa}\big(S^-S^+\rho S^-S^+ + S^+S^+\rho S^-S^- - S^-S^+S^+\rho S^- - S^+S^-S^+\rho S^-\big)+ \\
& Q_-Q_+^*Q_\Delta\big(4S^+S^-\rho S^-S^+ - 2S^+S^+S^-\rho S^- - 2S^-\rho S^-S^+S^+\big)+ \\
& \kappa^{-1}Q_-^2\big(S^-S^-\rho S^+S^+ + S^+S^-\rho S^+S^- - S^-\rho S^+S^-S^+ - S^+S^-S^-\rho S^+\big)+ \\
& \kappa^{-1}Q_+^2\big(S^+S^+\rho S^-S^- + S^-S^+\rho S^-S^+ - S^+\rho S^-S^+S^- - S^-S^+S^+\rho S^-\big)+ \\
& Q_-^2Q_\Delta\big(2S^+S^-\rho S^-S^+ - S^-\rho S^-S^+S^+ - S^+S^+S^-\rho S^-\big)+ \\
& Q_+^2Q_\Delta^*\big(2S^-S^+\rho S^+S^- - S^+\rho S^+S^-S^- - S^-S^-S^+\rho S^+\big) + \text{H.c}\Big],
\end{aligned}
\tag{3.36}
$$

It is important to note that it is sufficient to compute the terms corresponding to the 16 diagrams reported in Fig.(3.3), as the remaining contributions are their hermitian conjugates, represented by similar diagrams but with vertices swapped between the lower and upper solid lines.

It is useful to also note that Eq.(3.28) can be found directly from the second order diagrams in Fig.(2.2) and, in line with the notation of Eq.(2.44), Eq.(3.28) corresponds to the terms $\mathcal{L}^{(0)}\rho + \mathcal{L}^{(2)}\rho$ of the expansion, with $\mathcal{L}^{(0)}\rho = -i\omega_0[S^z, \rho]$.

With the fourth order contribution, the dynamics of the atomic system is described by the equation:

$$
\dot{\rho} = \mathcal{L}^{(0)}\rho + \mathcal{L}^{(2)}\rho + \mathcal{L}^{(4)}\rho. \tag{3.37}
$$

We refer to the sum of Eq.(3.28) and Eq.(3.36), or equivalently, Eq.(3.37) as fourth order Keldysh-Redfield equation, for brevity 4KRE.

Before turning our attention to the quantum solution of Eq.(3.37) and semiclassical analysis, we discuss the properties of the above density-matrix equation.
Eq.(3.28) and Eq.(3.36) are both Hermitian and preserve the trace. Furthermore, they both respect U(1) symmetry. In fact, the unitary part $\mathcal{L}^{(0)}\rho$, determined by the z component of the collective spin, is already symmetric and as concerns the dissipators at second and fourth order given by Eq.(3.28) and Eq.(3.36), symmetry-breaking operators such as $S^{\pm}$ always appear in pairs, therefore no explicit phase-dependent terms occur. Moreover, because of the U(1) symmetry, Eq.(3.37) is already in a secularised form, since it does not show any time-dependence in the interaction picture.
In second order theories, secularisation is a procedure commonly used to express a Redfield theory in Lindblad form [18], thus ensuring positivity [97, 91]. That is, removing those terms that are functions of time in the interaction picture. While the second order part, Eq.(3.28), can be easily manipulated and cast in a Lindblad form, as shown in Eq.(3.29), the fourth order contribution requires a detailed treatment to achieve the Lindblad form, that will be discussed in a following section.

3.2.1 Liouvillian

In this section, we explore the structure of Eq.(3.37) to gain information about the steady states of the equation and the soft modes arising in the symmetry-broken state. We may start to note that the U(1) symmetry property of Eq.(3.37) provides an important advantage when one wants to study the eigenspectrum of the Liouvillian superoperator. This benefit consists in the treatment of a Liouvillian which is a composition of decoupled subsectors that can be individually diagonalised, thus reducing the numerical effort. To better understand this concept, let us begin by writing the density matrix of the atoms as:

$$\rho = \sum_{k=-S}^{S} \sum_{M=-S-\min(k,0)}^{S-\max(k,0)} R_M^{(k)} \left|M\right\rangle \left\langle M+k\right|, \tag{3.38}$$

where, as a reminder $S = N/2$, M is the quantum number of the magnetic moment along the z-direction of the collective spin and the value of k identifies matrix elements of ρ, such as populations of the magnetic levels ($k = 0$) and off-diagonal elements or coherences as first ($k = \pm 1$), second ($k = \pm 2$) coherences and so on. When we substitute Eq.(3.38) into Eq.(3.37), the result is an equation of the motion for each element of the density matrix

whose evolution occurs within a specific k block and it is not influenced by other sectors:

$$\dot{R}^{(k)}_{M} = L^{(k)}_{M,M'} R^{(k)}_{M'}. \tag{3.39}$$

The above Eq.(3.39) can be equivalently represented by means of the following picture

$$\begin{pmatrix} \vdots \\ \hline \dot{\rho}^{(k=-1)} \\ \hline \dot{\rho}^{(k=0)} \\ \hline \dot{\rho}^{(k=1)} \\ \hline \vdots \end{pmatrix} = \left(\begin{array}{c|c|c|c|c} \ddots & \mathbf{0} & \dots & \dots & \dots \\ \hline \mathbf{0} & L^{(k=-1)} & \mathbf{0} & \dots & \dots \\ \hline \dots & \mathbf{0} & L^{(k=0)} & \mathbf{0} & \dots \\ \hline \dots & \dots & \mathbf{0} & L^{(k=1)} & \mathbf{0} \\ \hline \dots & \dots & \dots & \mathbf{0} & \ddots \end{array}\right) \cdot \begin{pmatrix} \vdots \\ \hline \rho^{(k=-1)} \\ \hline \rho^{(k=0)} \\ \hline \rho^{(k=1)} \\ \hline \vdots \end{pmatrix}$$

showing that the dynamics of specific elements of the density matrix is determined by single subsectors of the Liouvillian.

If we select the sector $k = 0$ for example, the dynamics of the population on the state $|M\rangle$ depends only on how much states $|M \pm 1\rangle$ and $|M \pm 2\rangle$ are populated, without being affected by coherences. In general, within a k sector, the dynamics of the elements $R^{(k)}_{M}$ is only affected by $R^{(k)}_{M\pm1}$, $R^{(k)}_{M\pm2}$ and this fact is due to the structure of the 4KRE. Specifically, for atoms populating the state M, some of the terms in the second order portion of the equation determine jumps in the levels $M \pm 1$ as $S^{+}\rho S^{-}$ and similar, while some of the terms in the fourth order part allow levels $M \pm 2$ to be populated because of couples of S^{+} and S^{-} operators acting on the state of the system. Therefore, for any sector k, the matrix $L^{(k)}_{M,M'}$ acquires a pentadiagonal structure with five bands, written as:

$$L^{(k)}_{M,M'} = A^{(k)}_{M}\delta_{M,M'} + B^{(k)}_{M}\delta_{M,M'-1} + C^{(k)}_{M}\delta_{M,M'-2} + D^{(k)}_{M}\delta_{M,M'+1} + E^{(k)}_{M}\delta_{M,M'+2}. \tag{3.40}$$

or equivalently, in matrix form:

$$\mathbf{L}^{(k)} = \begin{pmatrix} A^{(k)}_{-S} & B^{(k)}_{-S} & C^{(k)}_{-S} & 0 & 0 \\ D^{(k)}_{-S+1} & \ddots & \ddots & \ddots & 0 \\ E^{(k)}_{-S+2} & \ddots & \ddots & \ddots & C^{(k)}_{S-2-k} \\ 0 & \ddots & \ddots & \ddots & B^{(k)}_{S-1-k} \\ 0 & 0 & E^{(k)}_{S-k} & D^{(k)}_{S-k} & A^{(k)}_{S-k} \end{pmatrix}. \tag{3.41}$$

To find the five functions $A_M^{(k)} \dots E_M^{(k)}$, we make use of $S^{\pm}|SM\rangle = f_{\pm}^M|SM \pm 1\rangle$, where $f_{\pm}^M = \sqrt{(S \mp M)\,(S \pm M + 1)}$ are the coefficient corresponding to the application of the spin operators, and $S^z|SM\rangle = M|SM\rangle$. Furthermore, by noting the equivalence $f_-^M = f_+^{M-1}$, we might choose to express the coefficients in terms of only f_+^M, henceforth denoted as f^M, thus finding:

$$
\begin{aligned}
A_M^{(k)} =& i\omega_0 k - 2g^2\left[Q_-(f^{M-1})^2 + Q_-^*(f^{M+k-1})^2 + Q_+(f^M)^2 + Q_+^*(f^{M+k})^2\right] \\
&+ 4g^4\Big[2(Q_-)^3(f^{M-1})^2(f^{M-2})^2 + 2(Q_-^*)^3(f^{M+k-1})^2(f^{M+k-2})^2 + \\
&2(Q_+)^3(f^M)^2(f^{M+1})^2 + 2(Q_+^*)^3(f^{M+k})^2(f^{M+k+1})^2 + \\
&Q_-Q_+Q_\Sigma\left((f^{M-1})^2(f^{M+k-1})^2 + (f^M)^2(f^{M+k})^2 + 2(f^M)^2(f^{M-1})^2\right) + \\
&Q_-^*Q_+^*Q_\Sigma^*\left((f^{M-1})^2(f^{M+k-1})^2 + (f^M)^2(f^{M+k})^2 + 2(f^{M+k})^2(f^{M+k-1})^2\right) +
\end{aligned}
\tag{3.42}
$$

$$
\begin{aligned}
&(Q_-)^2 Q_\Sigma \left((f^{M-1})^4 + (f^{M-1})^2 (f^{M+k})^2\right) + (Q_-^*)^2 Q_\Sigma^* \left((f^{M+k-1})^4 + (f^M)^2 (f^{M+k-1})^2\right) + \\
&(Q_+)^2 Q_\Sigma \left((f^M)^4 + (f^M)^2 (f^{M+k-1})^2\right) + (Q_+^*)^2 Q_\Sigma^* \left((f^{M+k})^4 + (f^{M+k})^2 (f^{M-1})^2\right) + \\
&2\frac{|Q_-|^2}{\kappa} (f^{M-1})^2 (f^{M+k-1})^2 + 2\frac{|Q_+|^2}{\kappa} (f^M)^2 (f^{M+k})^2 + \\
&4Q_- Q_+^* Q_\Delta (f^{M+k})^2 (f^{M-1})^2 + 4Q_-^* Q_+ Q_\Delta^* (f^M)^2 (f^{M+k-1})^2 + \\
&\left(\frac{(Q_-)^2 + (Q_-{}^*)^2}{\kappa}\right) (f^{M-1})^2 (f^{M+k-1})^2 + \left(\frac{(Q_+)^2 + (Q_+{}^*)^2}{\kappa}\right) (f^M)^2 (f^{M+k})^2 + \\
&2(Q_-)^2 Q_\Delta (f^{M+k})^2 (f^{M-1})^2 + 2(Q_-^*)^2 Q_\Delta^* (f^M)^2 (f^{M+k-1})^2 + \\
&2(Q_+)^2 Q_\Delta^* (f^M)^2 (f^{M+k-1})^2 + 2(Q_+^*)^2 Q_\Delta (f^{M+k})^2 (f^{M-1})^2 \Big],
\end{aligned}
$$

$$
\begin{aligned}
B_M^{(k)} =& 2g^2 \left(Q_- + Q_-^*\right) f^M f^{M+k} - 4g^4 \Big[4(Q_-)^3 f^M f^{M+k} (f^{M-1})^2 + 4(Q_-^*)^3 f^M f^{M+k} (f^{M+k-1})^2 + \\
&Q_- Q_+ Q_\Sigma \left((f^M)^3 f^{M+k} + f^M f^{M+k} (f^{M+1})^2\right) + Q_-^* Q_+^* Q_\Sigma^* \left(f^M (f^{M+k})^3 + f^M f^{M+k} (f^{M+k+1})^2\right) + \\
&(Q_-)^2 Q_\Sigma (f^M)^3 f^{M+k} + (Q_-^*)^2 Q_\Sigma^* f^M (f^{M+k})^3 + \\
&(Q_+)^2 Q_\Sigma f^M f^{M+k} (f^{M+1})^2 + (Q_+^*)^2 Q_\Sigma^* f^M f^{M+k} (f^{M+k+1})^2 + \\
&\frac{|Q_-|^2}{\kappa} \left(f^M f^{M+k} (f^{M-1})^2 + f^M f^{M+k} (f^{M+k-1})^2 + (f^M)^3 f^{M+k} + f^M (f^{M+k})^3\right) + \\
&2Q_- Q_+^* Q_\Delta f^M f^{M+k} (f^{M+k+1})^2 + 2Q_-^* Q_+ Q_\Delta^* f^M f^{M+k} (f^{M+1})^2 + \\
&\frac{(Q_-)^2}{\kappa} \left(f^M (f^{M+k})^3 + f^M f^{M+k} (f^{M-1})^2\right) - \frac{(Q_-{}^*)^2}{\kappa} \left((f^M)^3 f^{M+k} + f^M f^{M+k} (f^{M+k-1})^2\right) + \\
&(Q_-)^2 Q_\Delta f^M f^{M+k} (f^{M+k+1})^2 + (Q_-^*)^2 Q_\Delta^* f^M f^{M+k} (f^{M+1})^2 + \\
&(Q_+)^2 Q_\Delta^* f^M f^{M+k} (f^{M+1})^2 + (Q_+^*)^2 Q_\Delta f^M f^{M+k} (f^{M+k+1})^2 \Big],
\end{aligned} \tag{3.43}
$$

$$
C_M^{(k)} = 4g^4 \left[2(Q_-)^3 + 2(Q_-^*)^3 + \frac{(Q_- + Q_-^*)^2}{\kappa}\right] f^M f^{M+1} f^{M+k} f^{M+k+1}, \tag{3.44}
$$

$$
\begin{aligned}
D_M^{(k)} =& 2g^2\left(Q_+ + Q_+^*\right) f^{M-1} f^{M+k-1} - 4g^4\Big[4(Q_+)^3 (f^M)^2 f^{M-1} f^{M+k-1} + \\
& 4(Q_+^*)^3 (f^{M+k})^2 f^{M-1} f^{M+k-1} + Q_- Q_+ Q_\Sigma \left((f^{M-1})^3 f^{M+k-1} + f^{M-1}(f^{M-2})^2 f^{M+k-1}\right) + \\
& Q_-^* Q_+^* Q_\Sigma^* \left(f^{M-1}(f^{M+k-1})^3 + f^{M-1} f^{M+k-1}(f^{M+k-2})^2\right) + \\
& (Q_-)^2 Q_\Sigma f^{M-1} f^{M+k-1}(f^{M-2})^2 + (Q_-^*)^2 Q_\Sigma^* f^{M-1} f^{M+k-1}(f^{M+k-2})^2 + \\
& (Q_+)^2 Q_\Sigma (f^{M-1})^3 f^{M+k-1} + (Q_+^*)^2 Q_\Sigma^* f^{M-1}(f^{M+k-1})^3 + \\
& \frac{|Q_+|^2}{\kappa}\left((f^M)^2 f^{M-1} f^{M+k-1} + (f^{M+k})^2 f^{M-1} f^{M+k-1} + (f^{M-1})^3 f^{M+k-1} + f^{M-1}(f^{M+k-1})^3\right) + \\
& 2Q_- Q_+^* Q_\Delta f^{M-1} f^{M+k-1}(f^{M-2})^2 + 2Q_-^* Q_+ Q_\Delta^* f^{M-1} f^{M+k-1}(f^{M+k-2})^2 + \\
& \frac{(Q_+)^2}{\kappa}\left(f^{M-1}(f^{M+k-1})^3 + (f^M)^2 f^{M-1} f^{M+k-1}\right) + \\
& \frac{(Q_+{}^*)^2}{\kappa}\left((f^{M-1})^3 f^{M+k-1} + (f^{M+k})^2 f^{M-1} f^{M+k-1}\right) + \\
& (Q_-)^2 Q_\Delta f^{M-1} f^{M+k-1}(f^{M-2})^2 + (Q_-^*)^2 Q_\Delta^* f^{M-1} f^{M+k-1}(f^{M+k-2})^2 + \\
& (Q_+)^2 Q_\Delta^* f^{M-1} f^{M+k-1}(f^{M+k-2})^2 + (Q_+^*)^2 Q_\Delta f^{M-1} f^{M+k-1}(f^{M-2})^2\Big],
\end{aligned}
\tag{3.45}
$$

$$
E_M^{(k)} = 4g^4\left[2(Q_+)^3 + 2(Q_+^*)^3 + \frac{(Q_+ + Q_+^*)^2}{\kappa}\right] f^{M-1} f^{M-2} f^{M+k-1} f^{M+k-2}. \tag{3.46}
$$

As mentioned, a Liouvillian divided in independent blocks, each one having a diagonal form, as shown in Eq.(3.41), facilitates the numerical diagonalisation even in the large N limit. Thus to maintain the expressions as general as possible, for a given sector k, we might label eigenvalues and eigenvectors of the matrix Eq.(3.41) following the notation rule below:

$$
L_{M,M'}^{(k)} R_{n,M'}^{(k)} = \lambda_n^{(k)} R_{n,M}^{(k)}, \tag{3.47}
$$

where $R_{n,M}^{(k)}$ are eigenvectors of the k sector of the Liouvillian with eigenvalue $\lambda_n^{(k)}$. The eigenspectrum $\{\lambda_n^{(k)}\}$ is sorted by absolute value of the real part, according to the

discussion in section 2.4:

$$|\,\mathrm{Re}[\lambda_0^{(k)}]| < |\,\mathrm{Re}[\lambda_1^{(k)}]| < \cdots < |\,\mathrm{Re}[\lambda_n^{(k)}]| < \ldots \tag{3.48}$$

3.2.2 Steady state of 4KRE

As previously discussed, a reliable reduced theory has to fulfill specific requirements, such as Hermiticity and trace-preservation, properties provided by 4KRE. In addition to those, the theory has to predict the correct steady states and modes associated with the symmetry breaking of the model, as indicated by the results of the complete problem.

Here, we solve 4KRE to find the steady state of this effective theory. To this aim, we have to look into a particular sector of the Liouvillian superoperator, that is $L^{(k)} = L^{(0)}$.

The $k = 0$ block determines the dynamics of symmetry-respecting quantities as $\langle S^z\rangle$, $\langle S^z S^z\rangle$, $\langle S^+ S^-\rangle$, and in general those expectations of spin operators with equal number of spin-raising and spin-lowering operators. The eigenspectrum of this sector, in particular its real part, provides details about the relaxation rates to stationary states, such as $\langle S^z\rangle_{SS}$. For our purposes, we are going to discuss the physical meaning of the first two eigenvalues of this sector: $\lambda_0^{(0)}$ and $\lambda_1^{(0)}$.

Firstly, a steady state observable as $\langle S^z\rangle_{SS}$ can be computed by means of the 0 eigenvector, $R_{0,M}^{(0)}$, which is associated with $\lambda_0^{(0)} = 0$. This is shown in Fig.(3.5), as a function of the coupling strength $g\sqrt{N}$ in a range of increasing system sizes. In sharp contrast to the conclusions of 2RE highlighted in section 3.1.2, the inclusion of a higher-order contribution introduces a clear discontinuity in the steady-state behaviour as the atom-light coupling approaches the critical value. The stationary state predicted by 4KRE tends to the semiclassical result of the coupled atom-cavity problem [17] in the limit of $N \to \infty$, as shown in Fig.(3.5).

To test the accuracy of 4KRE in capturing the g-dependent steady state, we analysed and verified the convergence to the exact normal state $S^z = -N/2$ in the thermodynamic limit. This is shown in Fig.(3.6). According to the parameters used, the critical point is located at $g_c\sqrt{N} = 0.44$ MHz, therefore we choose three values of coupling below this point to observe how the steady state scales with the system size. As shown in Fig.(3.6), the points (closed circles) lie on a line at each of the $g\sqrt{N}$ values considered and it is thus possible to extract the steady state value (open circles) for $N \to \infty$, or equivalently $\frac{1}{N} \to 0$, as

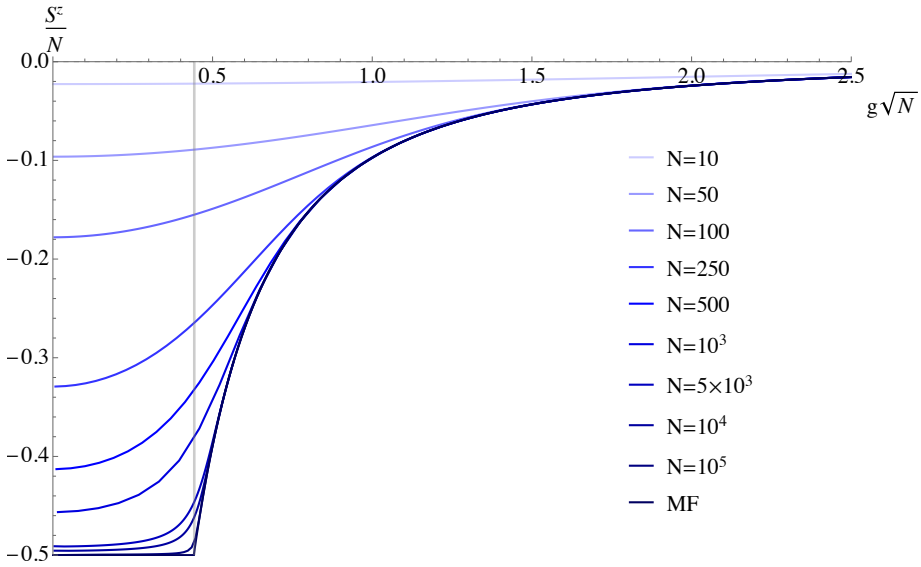

Fig. 3.5. Rescaled steady state of S^z as a function of light-matter coupling evaluated from 4KRE in a range of N values (threshold at $g_c\sqrt{N} = 0.44$ MHz). The results are compared with the mean field prediction of the full problem Eq.(3.3). Parameters used are $\omega_0 = 47$ kHz, $\kappa = 8.1$ MHz, $\omega = 5$ MHz.

the intercept of the three lines. As it is shown, all of those intercepts coincide with the expected normal state value.

Now we move forward with the second eigenvalue in the sorted list, $\lambda_1^{(0)}$. Recalling Eq.(2.59), the real part of a non vanishing eigenvalue represents the decay rate of some averaged observable towards its steady state value. In the present case, if one knows already the solution to the eigenvalue problem obtained by linearising Eqs.(1.39-1.42) [17], with respect to the g-dependent steady state, then when comparing with the eigenvalues of 4KRE one finds that $\mathrm{Re}[\lambda_1^{(0)}]$ describes the relaxation rate towards the stationary state of $\langle S^z \rangle$ at each value of coupling strength. Similarly to Fig.(3.5) for the steady state, the evolution of this eigenvalue with $g\sqrt{N}$ is shown in Fig.(3.7) for increasing values of N and compared to the mean-field result of the full problem [17]. As shown, the eigenvalue is gapped below and above the critical point and this indicates that, when perturbed, the system takes a finite time to reach the corresponding steady state attractor. While for finite N the spectrum always appear gapped, in the thermodynamic limit there is only one point where it is completely gapless and this occurs at the critical point. This happens to signal

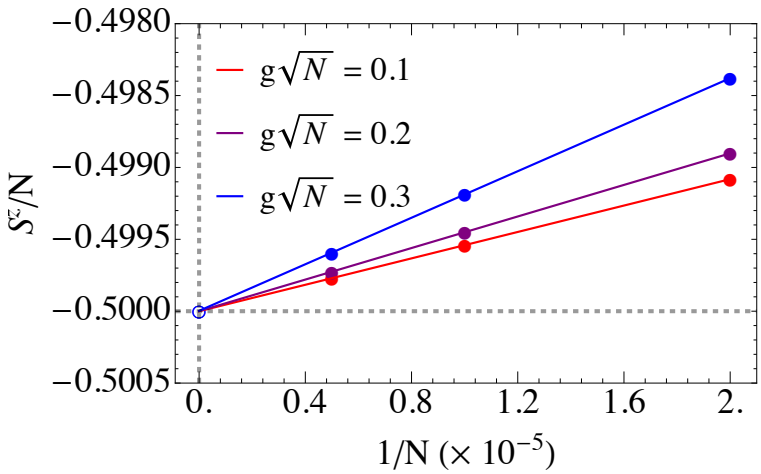

Fig. 3.6. Rescaled steady state value of S^z as a function of system size evaluated from 4KRE in a range of $g\sqrt{N}$ below threshold ($g_c\sqrt{N} = 0.44$ MHz). The closed circles corresponds to the steady state calculated at $N = 5\times10^4, 10^5, 2\times10^5$, while the open circles are the normal state at $N \to \infty$. Parameters used are $\omega_0 = 47$ kHz, $\kappa = 8.1$ MHz, $\omega = 5$ MHz. Reprinted figure with permission from R. Palacino and J. Keeling, Phys. Rev. Research **3**, L032016, 2021. Copyright (2021) by the American Physical Society.

a change of stability in the state of the system while going across threshold.

While $\lambda_1^{(0)}$ represents the eigenvalue with the smallest real part in the $k = 0$ sector, it does not describe the slowest timescale occurring in the system. In other words, it is not the Liouvillian gap, the eigenvalue with the smallest real part of all Liouvillian spectrum (excluding the zeroth eigenvalue of $k = 0$). To find the Liouvillian gap, it is necessary to look into another sector and this will be theme of the next section.

3.2.3 Liouvillian gap of 4KRE

In section 3.2.1 we have described the division in blocks of the Liouvillian due to the symmetry of 4KRE, with a $k = 0$ sector concerning the dynamics of symmetry-preserving observables and $k \neq 0$ yielding information about the behaviour of expectations as $\langle S^{\pm}\rangle$ ($k = \pm1$), $\langle S^{\pm^2}\rangle$ ($k = \pm2$) and so on.

As discussed in [109], the steady state characterising an open system is unique and symmetry-preserving below a critical value of some coupling parameter, whereas the same statement is in general not true in the symmetry-broken phase. Above threshold, the system can in fact be described by more than one steady state, with any superposition

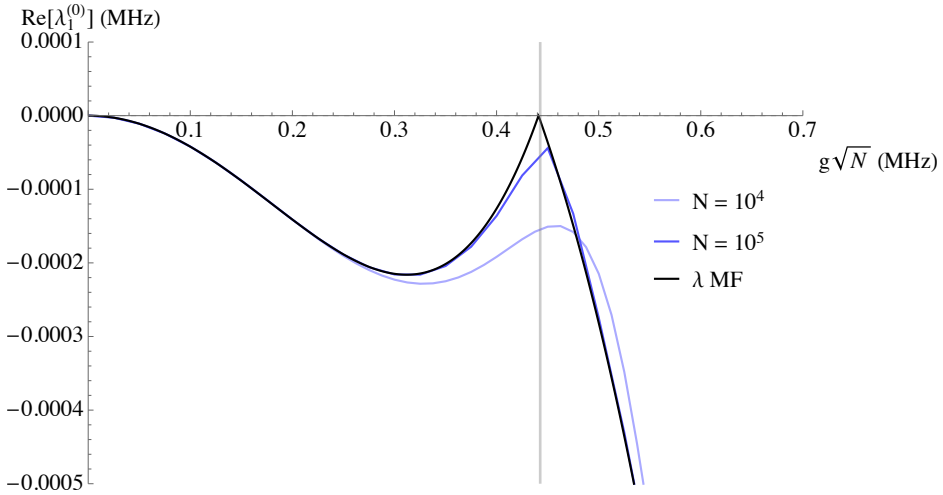

Fig. 3.7. First non-zero eigenvalue of the $k = 0$ sector in function of $g\sqrt{N}$ evaluated from 4KRE for three N values (threshold at $g_c\sqrt{N} = 0.44$ MHz) to show the convergence to the mean field prediction of the full problem Eq.(3.3). Parameters used are $\omega_0 = 47$ kHz, $\kappa = 8.1$ MHz, $\omega = 5$ MHz.

of those states being also a valid stationary state. This behaviour is associated with the emergence of an extra zero mode in correspondence of the symmetry-broken phase, the superradiant state in our case. This condition of an extra zero mode means the Liuovillian gap will vanish [109]. Since the vanishing Liouvillian gap is indicator of symmetry breaking, this eigenvalue must be related to the off-diagonal $k \neq 0$ sectors of the Liouvillian matrix.

By checking the magnitude in the spectra of different blocks to identify the smallest non zero eigenvalue, we find it in the $k = \pm 1$ complex conjugates sectors. According to our notation rule, we label it as $\lambda_0^{(1)}$. Analogously to Fig.(3.7), this is plotted in Fig.(3.8)a) as a function of the coupling strength, for large number N of atoms. A certain reduction of the gap is visible above threshold as we increase N, but it should be stressed that for any large but finite N, we would not observe perfect closure of the gap. Similarly to what we have done in Fig.(3.6) to test the convergence of the steady state predicted by 4KRE to the normal state at $N \to \infty$, we collect gap values at high system sizes in the symmetry-broken phase with the aim to first get an idea about the scaling law with $1/N$ and then extrapolate the Liouvillian gap at $N \to \infty$. As shown in Fig.(3.8)b), Re$[\lambda_0^{(1)}]$ scales linearly with the

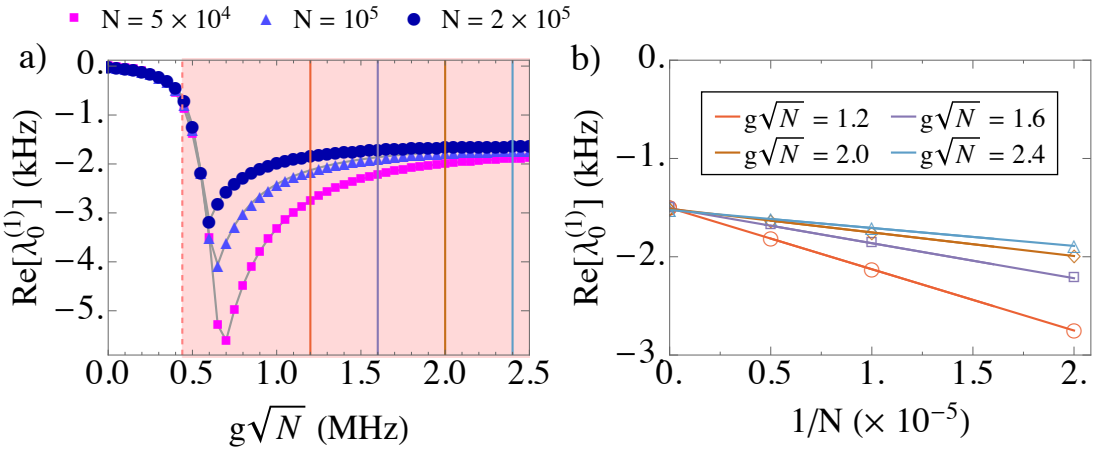

Fig. 3.8. a) Liouvillian gap as a function of $g\sqrt{N}$ for three values of number of atoms. The vertical dashed line corresponds to $g_c\sqrt{N} = 0.44$ MHz dividing the normal (white) from the superradiant phase (pink), while the solid lines are selected values of $g\sqrt{N}$ above the critical point used in b) to analyse the scaling law with the inverse of system size. The open geometrical shapes are the gap values evaluated for $N = 5 \times 10^4, 10^5, 2 \times 10^5$ and the intercepts show the extrapolated gap at $N \to \infty$ from the linear fitting. Parameters used are $\omega_0 = 47$ kHz, $\kappa = 8.1$ MHz, $\omega = 5$ MHz. Reprinted figure with permission from R. Palacino and J. Keeling, Phys. Rev. Research **3**, L032016, 2021. Copyright (2021) by the American Physical Society.

inverse of the system size, following $\lambda_0^{(1)} = A + B/N$, and the value of the gap at $N \to \infty$ corresponds to the intercept A extracted from the fitting. Surprisingly, the finite value of the intercept implies that a gap remains also when N approaches the thermodynamic limit.

To summarise the results so far, we have discussed the reasons why a standard second order Redfield theory is inadequate to describe the superradiance phase transition predicted by a class of two-mode Dicke models with U(1) symmetry, studied in [17]. We then derived and included in the analysis the fourth order term of the density matrix equation, referred to as 4KRE. This higher order Redfield equation is highly accurate with regards to the symmetric sector of the dynamics, thus catching steady states, relaxation rates of the long-time dynamics and the position of the threshold in the phase diagram. However, when compared to the mean field solution of the full atom-cavity problem, this higher order theory does not predict the gapless mode associated with the symmetry breaking in the thermodynamic limit.

3.2.4 Mean field and Cumulant expansion

As seen in the previous sections, the fourth order Keldysh-Redfield equation 4KRE, given by Eq.(3.37), has been derived and solved providing the results shown in Fig.(3.5) and Fig.(3.7) in terms of steady state solutions and eigenmodes associated with those solutions.

Here, we proceed by writing equations of motion for the expectation values of spin operators. To do so, we employ 4KRE, Eq.(3.37), to derive an equation for the mean value of a generic operator A, given as follows:

$$
\begin{aligned}
\left\langle \dot{A} \right\rangle = & -i\omega_0 \langle [A, S^z] \rangle - 2g^2 \langle Q_+^B [A, S^-] S^+ + Q_-^A [A, S^+] S^- + \text{h.c.} \rangle + \\
& 4g^4 \Big[\Big\langle 2{Q_-^A}^3 \left(\left[A, S^+\right] S^+ S^- S^- + S^+ \left[S^+, A\right] S^- S^- \right) \Big\rangle + \\
& \Big\langle 2{Q_+^B}^3 \left([A, S^-] S^- S^+ S^+ + S^- [S^-, A] S^+ S^+ \right) \Big\rangle + \\
& \langle Q_-^A Q_+^B Q^\Sigma \left(\left[A, S^+\right] S^- S^- S^+ + [A, S^-] S^+ S^+ S^- + \right. \\
& \left. S^+ [S^-, A] S^+ S^- + S^- \left[S^+, A\right] S^- S^+ \right) \rangle + \\
& \Big\langle {Q_-^A}^2 Q^\Sigma \left(\left[A, S^+\right] S^- S^+ S^- + S^- \left[S^+, A\right] S^+ S^- \right) \Big\rangle + \\
& \Big\langle {Q_+^B}^2 Q^\Sigma \left([A, S^-] S^+ S^- S^+ + S^+ [S^-, A] S^- S^+ \right) \Big\rangle + \\
& \left\langle \frac{Q_-^A Q_-^{A*}}{\kappa} \left(S^+ [S^-, A] S^+ S^- + S^+ \left[S^+, A\right] S^- S^- \right) \right\rangle + \\
& \left\langle \frac{Q_+^B Q_+^{B*}}{\kappa} \left(S^- \left[S^+, A\right] S^- S^+ + S^- [S^-, A] S^+ S^+ \right) \right\rangle + \\
& \langle 2 Q_-^A Q_+^{B*} Q^\Delta \left(S^- \left[S^+, A\right] S^+ S^- + S^- S^+ \left[A, S^+\right] S^- \right) \rangle + \\
& \left\langle \frac{{Q_-^A}^2}{\kappa} \left(S^+ \left[S^+, A\right] S^- S^- + S^+ S^- \left[A, S^+\right] S^- \right) \right\rangle + \\
& \left\langle \frac{{Q_+^B}^2}{\kappa} \left(S^- [S^-, A] S^+ S^+ + S^- S^+ [A, S^-] S^+ \right) \right\rangle + \\
& \Big\langle {Q_-^A}^2 Q^\Delta \left(S^- S^+ \left[A, S^+\right] S^- + S^- \left[S^+, A\right] S^+ S^- \right) \Big\rangle + \\
& \Big\langle {Q_+^B}^2 Q^{\Delta *} \left(S^+ S^- [A, S^-] S^+ + S^+ [S^-, A] S^- S^+ \right) + \text{h.c.} \Big\rangle \Big] .
\end{aligned}
\tag{3.49}
$$

Once Eq.(4.22) is obtained, one can substitute $A = S^{\pm}, S^z$ and solve the canonical com-

mutation relations for the collective spin to finally find:

$$\begin{aligned}\left\langle \dot{S}^{-}\right\rangle = &-i\omega_0 \left\langle S^{-}\right\rangle - 2g^2 \left\langle -2Q_{-}^{A} S^{z} S^{-} + 2Q_{+}^{B*} S^{-} S^{z}\right\rangle + \\ &8g^4 \left[\left\langle S^{-} S^{-} S^{+} \left(Q_{-}^{A} Q_{+}^{B} Q^{\Sigma} - 2Q_{+}^{B*3} - \frac{Q_{+}^{B} Q_{+}^{B*}}{\kappa} - \frac{Q_{+}^{B*2}}{\kappa}\right) + \right.\right. \\ &S^{+} S^{-} S^{-} \left(Q_{-}^{A*} Q_{+}^{B*} Q^{\Sigma*} - 2Q_{-}^{A3} - \frac{Q_{-}^{A} Q_{-}^{A*}}{\kappa} - \frac{Q_{-}^{A2}}{\kappa}\right) + \\ &\left.\left. S^{-} S^{+} S^{-} \left(Q_{-}^{A2} Q^{\Sigma} + Q_{+}^{B*2} Q^{\Sigma*} + 2Q_{-}^{A} Q_{+}^{B*} Q^{\Delta} + Q_{-}^{A2} Q^{\Delta} + Q_{+}^{B*2} Q^{\Delta}\right)\right\rangle\right],\end{aligned} \tag{3.50}$$

$$\begin{aligned}\left\langle \dot{S}^{z}\right\rangle = &-2g^2 \left\langle -Q_{+}^{B} S^{-} S^{+} + Q_{-}^{A} S^{+} S^{-} + Q_{-}^{A*} S^{+} S^{-} - Q_{+}^{B*} S^{-} S^{+}\right\rangle + \\ &8g^4 \left[\left\langle S^{z} S^{-} S^{+} \left(Q_{-}^{A} Q_{+}^{B} Q^{\Sigma} + Q_{+}^{B2} Q^{\Sigma}\right) + S^{z} S^{+} S^{-} \left(Q_{-}^{A} Q_{+}^{B} Q^{\Sigma} + Q_{-}^{A2} Q^{\Sigma}\right) + \right.\right. \\ &S^{+} S^{-} S^{z} \left(Q_{-}^{A*} Q_{+}^{B*} Q^{\Sigma*} + Q_{-}^{A*2} Q^{\Sigma*}\right) + S^{-} S^{+} S^{z} \left(Q_{-}^{A*} Q_{+}^{B*} Q^{\Sigma*} + Q_{+}^{B*2} Q^{\Sigma*}\right) + \\ &\left.\left. -S^{+} S^{z} S^{-} \left(2\frac{Q_{-}^{A} Q_{-}^{A*}}{\kappa} + \frac{Q_{-}^{A2}}{\kappa} + \frac{Q_{-}^{A*2}}{\kappa}\right) - S^{-} S^{z} S^{+} \left(2\frac{Q_{+}^{B} Q_{+}^{B*}}{\kappa} + \frac{Q_{+}^{B2}}{\kappa} + \frac{Q_{+}^{B*2}}{\kappa}\right)\right\rangle\right].\end{aligned} \tag{3.51}$$

The equation for $\left\langle \dot{S}^{+}\right\rangle$ is readily found by complex conjugation of Eq.(3.50).
So far, both Eq.(3.50) and Eq.(3.51) are exact, i.e. their derivation does not contemplate any approximation. One could first analyse the dynamics of Eq.(3.50) and Eq.(3.51) in a mean field framework. As seen in section 2.5, this approximation consists in substituting all second order and third order expectations with the products of the single-operator expectations, $\langle S^{\alpha} S^{\beta} S^{\gamma}\rangle = \langle S^{\alpha}\rangle\langle S^{\beta}\rangle\langle S^{\gamma}\rangle$. At this point, in addition to solving numerically the resulting mean field equations, one may perform a stability analysis of the solutions. With regards to the latter task, it appears that when Eq.(3.50) and Eq.(3.51) are linearised around the normal state, $\langle S^{\pm}\rangle_{SS} = 0, \langle S^{z}\rangle_{SS} = -N/2$, terms like $S^{+}S^{-}$ (involved also in products with S^{z}) prevent from completing the procedure. This means in practice that the term $\langle S^{+}\rangle\langle S^{-}\rangle$, once linearised around the normal state, becomes $(\langle S^{+}\rangle_{SS} + \delta S^{+})(\langle S^{-}\rangle_{SS} + \delta S^{-}) = \delta S^{+}\delta S^{-}$, while we are interested in terms that are linear in the perturbation.
We thus see that the eigenvalue equation obtained from standard linearisation of mean field Eq.(3.50) and Eq.(3.51) does not ever describe instability. This fact thus seems to prevent the observation of the phase transition in the stability phase diagram, in clear

contrast with the predictions of 4KRE that predict an instability, as shown in Fig.(3.5). The reason of this apparent failure lies in the structure of the solution of 4KRE. Indeed, while U(1) symmetry guarantees $\langle S^x \rangle = 0$ in the normal state, higher order moments such as $\langle (S^x)^2 \rangle \propto (\langle S^+ S^- \rangle + \langle S^- S^+ \rangle)$ can have a non-zero value. Therefore, a more adequate approach would require to derive dynamical equations for U(1)-symmetric correlation functions of spin operators. To this aim, the form of the steady state density matrix suggests the steps to take.

Let us then take a step back to the $k = 0$ sector. The probability distribution of the steady state is given by $P_M = R^{(0)}_{0,M}$ where $R^{(0)}_{0,M}$ is the eigenvector of Eq. (3.40), corresponding to eigenvalue $\lambda^{(0)}_0 = 0$. If we wish to visualise the dependence of P_M on the state with magnetic moment M throughout the range of coupling values, we observe a Gaussian-like type of distribution, as shown in Fig.(3.9), compatible with:

$$P_M \propto e^{-\frac{(M-\langle S^z \rangle_C)^2}{2\langle S^z S^z \rangle_C}}. \tag{3.52}$$

Expression 3.52 indeed describes the probability to find the steady state of the spin system at the expected $\langle S^z \rangle_C = \langle S^z \rangle$ value with uncertainty given by the second order cumulant of S^z, $\langle S^z S^z \rangle_C = \langle S^z S^z \rangle - \langle S^z \rangle^2$, at a given coupling strength $g\sqrt{N}$. For $g < g_c$, the distribution is one-sided as it is centered at $M = -N/2$ while in the $g > g_c$ region, the position of the peak moves, asymptotically approaching $M = 0$ in the limit of large $g\sqrt{N}$, consistent with the evolution of $\langle S^z \rangle$ with $g\sqrt{N}$ seen in Fig.(3.5). In addition to the shift of P_M, the distribution has a finite width that shrinks as N increases. This reduction of the width with N implies that $\langle S^z S^z \rangle_C \to 0$, thus $\langle S^z S^z \rangle \to \langle S^z \rangle^2$, leading to the conclusion that a single equation for the dynamics of $\langle S^z \rangle$ is sufficient to describe the critical behaviour at the thermodynamic limit. These observations justify the importance of cumulant equations to correctly catch the evolution of the steady state through threshold for finite size systems and they clarify how the mean field limit emerges at $N \to \infty$.

In light of the above findings, we thus derive equations for the first two moments of the steady-state probability distribution Eq.(3.52), namely for $\langle S^z \rangle$ and $\langle S^z S^z \rangle$, therefore truncating the expansion at the second cumulant, neglecting all higher order cumulants. The resulting equations will include third order and fourth order correlation functions of spin operators from the second order and fourth order terms in the density matrix equation, respectively, that need to be decoupled in products of lower order expectations.

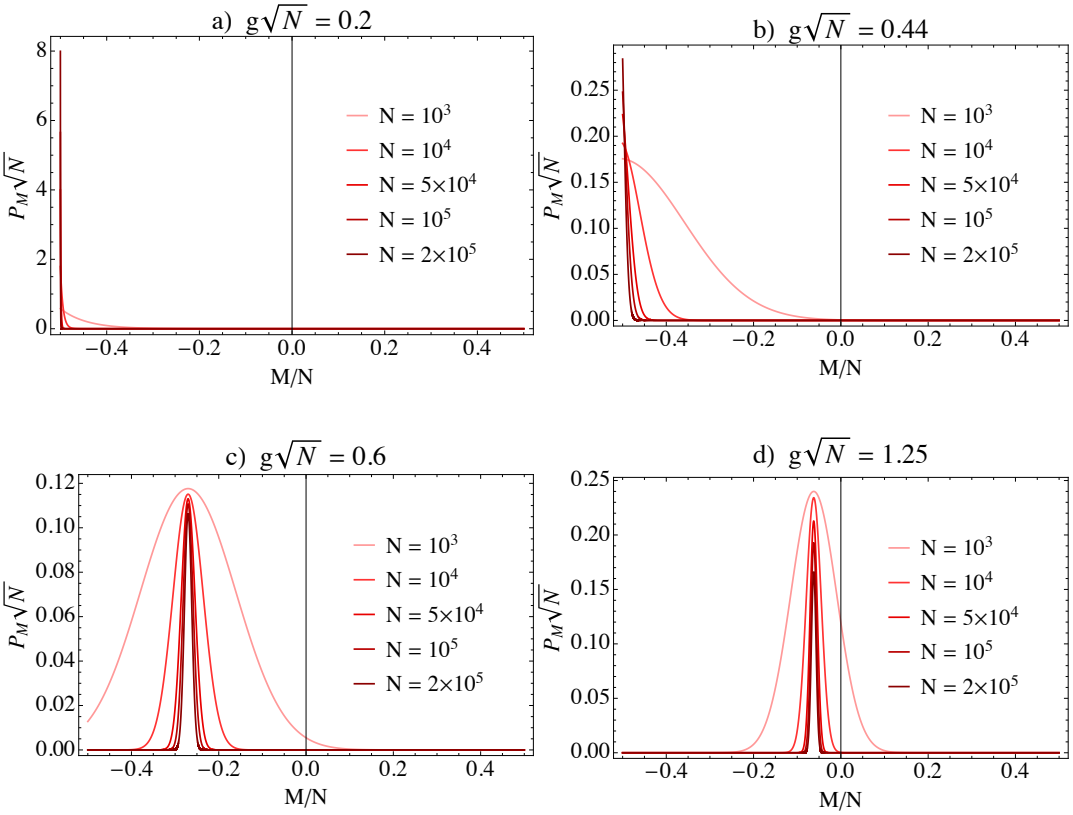

Fig. 3.9. N and g-dependent steady state probabilities plotted in function of M/N. a) Distributions below g_c, b) at $g = g_c$, c) and d) above g_c. Parameters used are $\omega_0 = 47$ kHz, $\kappa = 8.1$ MHz, $\omega = 5$ MHz. Reprinted figure with permission from R. Palacino and J. Keeling, Phys. Rev. Research **3**, L032016, 2021. Copyright (2021) by the American Physical Society.

A standard method to decouple higher order correlators is provided in [131]. However, that approach is strictly valid for classical variables, as we have discussed in section 2.5, while in our case the variables under consideration are non-commuting spin operators. Therefore, a strategy to take into account this property must be adopted before decoupling higher order moments according to the textbook rule [131]. Moreover, as observed above, since P_M depends exclusively on expectations of S^z, we need first to re-express spin variables in terms of S^z operators only. This is readily achieved by means of the identity $S^+S^- = S(S+1) - S^zS^z + S^z$, which relies on the conservation of the collective spin S length throughout the dynamics. Once all spin operators are expressed in terms of products of S^z, these operators commute, and so can be treated analogously to classical cumulants. In the following we give the protocol to derive the cumulant equations:

1. Re-ordering of non commuting operators so that S^+ and S^- are next to each other.

2. Applying the identity $S^+S^- = S(S+1) - S^zS^z + S^z$.

3. Standard decoupling of classical variables [131].

We provide some examples of correlators with three and four operators to treat with the above recipe. The first example is $\langle S^+S^zS^-\rangle$:

$$\begin{aligned}\left\langle S^+S^zS^-\right\rangle &= \left\langle S^zS^+S^-\right\rangle + \left\langle \left[S^+, S^z\right]S^-\right\rangle = \left\langle S^zS^+S^-\right\rangle - \left\langle S^+S^-\right\rangle \\ &= \langle S^z\left[S(S+1) - S^zS^z + S^z\right]\rangle - \langle S(S+1) - S^zS^z + S^z\rangle \\ &= S(S+1)\langle S^z\rangle - \langle S^zS^zS^z\rangle + 2\langle S^zS^z\rangle - S(S+1) - \langle S^z\rangle \\ &= S(S+1)\langle S^z\rangle - 3\langle S^z\rangle\langle S^zS^z\rangle + 2\langle S^z\rangle^3 + 2\langle S^zS^z\rangle - S(S+1) - \langle S^z\rangle\end{aligned} \tag{3.53}$$

On the right hand side of Eq.(3.53), in the first line, we manipulate the correlator making use of the commutation relation between spin operators (point 1.) with the aim of moving to a representation where we can exploit the conservation law of the spin length and thus use the identity in point 2. (second line in Eq.(3.53)). The new expression now contains products of S^z only which behave as classical variables and can be finally decoupled as prescribed in [131] (point 3.). Other examples, $\left\langle S^+S^{z2}S^-\right\rangle$ and $\langle S^+S^+S^-S^-\rangle$, similar to the previous case but with four operators, follow the same procedure:

$$\begin{aligned}&\left\langle S^+S^{z2}S^-\right\rangle = \left\langle S^+S^-S^{z2}\right\rangle + \left\langle S^+\left[S^{z2}, S^-\right]\right\rangle = \left\langle S^+S^-S^{z2}\right\rangle - \left\langle S^+S^zS^-\right\rangle - \left\langle S^+S^-S^z\right\rangle \\ &= \left\langle S^+S^-S^{z2}\right\rangle - 2\left\langle S^+S^-S^z\right\rangle - \left\langle S^+\left[S^z, S^-\right]\right\rangle = \left\langle S^+S^-S^{z2}\right\rangle - 2\left\langle S^+S^-S^z\right\rangle + \left\langle S^+S^-\right\rangle \\ &= \langle\left[S(S+1) - S^zS^z + S^z\right]S^zS^z\rangle - 2\langle S^z\left[S(S+1) - S^zS^z + S^z\right]\rangle + \\ &\quad \langle S(S+1) - S^zS^z + S^z\rangle \\ &= S(S+1)\langle S^zS^z\rangle - \langle S^zS^zS^zS^z\rangle + 3\langle S^zS^zS^z\rangle - 2S(S+1)\langle S^z\rangle - 3\langle S^zS^z\rangle + \\ &= S(S+1) + \langle S^z\rangle \\ &= S(S+1)\langle S^zS^z\rangle - 3\langle S^zS^z\rangle^2 + 2\langle S^z\rangle^4 + 9\langle S^z\rangle\langle S^zS^z\rangle - 6\langle S^z\rangle^3 - 2S(S+1)\langle S^z\rangle \\ &= -3\langle S^zS^z\rangle + S(S+1) + \langle S^z\rangle\end{aligned} \tag{3.54}$$

$$\begin{aligned}\left\langle S^{+}S^{+}S^{-}S^{-}\right\rangle &= \left\langle S^{+}S^{-}S^{+}S^{-}\right\rangle + \left\langle S^{+}\left[S^{+},S^{-}\right]S^{-}\right\rangle = \left\langle S^{+}S^{-}S^{+}S^{-}\right\rangle + 2\left\langle S^{+}S^{z}S^{-}\right\rangle \\ &= S^{2}\left(S+1\right)^{2} + 3\left\langle S^{z}S^{z}\right\rangle^{2} - 2\left\langle S^{z}\right\rangle^{4} + 5\left\langle S^{z}S^{z}\right\rangle - 2S\left(S+1\right)\left\langle S^{z}S^{z}\right\rangle \\ &- 12\left\langle S^{z}\right\rangle\left\langle S^{z}S^{z}\right\rangle + 8\left\langle S^{z}\right\rangle^{3} + 4S\left(S+1\right)\left\langle S^{z}\right\rangle - 2S\left(S+1\right) - 2\left\langle S^{z}\right\rangle\end{aligned} \tag{3.55}$$

Following that approach, we derive coupled EOMs for the first two moments of S^{z}:

$$\begin{aligned}\frac{d}{dt}\left\langle S^{z}\right\rangle = 2g^{2}&\left\{\alpha_{2}^{B}\left[S(S+1) - \left\langle S^{z}S^{z}\right\rangle - \left\langle S^{z}\right\rangle\right] - \alpha_{2}^{A}\left[S(S+1) - \left\langle S^{z}S^{z}\right\rangle + \left\langle S^{z}\right\rangle\right]\right\} + \\ &2g^{4}\left\{\gamma_{4}^{A}\left[S(S+1)\left\langle S^{z}\right\rangle - 3\left\langle S^{z}\right\rangle\left\langle S^{z}S^{z}\right\rangle + 2\left\langle S^{z}\right\rangle^{3} + \left\langle S^{z}S^{z}\right\rangle\right] + \right. \\ &\gamma_{4}^{B}\left[S(S+1)\left\langle S^{z}\right\rangle - 3\left\langle S^{z}\right\rangle\left\langle S^{z}S^{z}\right\rangle + 2\left\langle S^{z}\right\rangle^{3} - \left\langle S^{z}S^{z}\right\rangle\right] - \\ &\delta_{4}^{A}\left[S(S+1)\left\langle S^{z}\right\rangle - 3\left\langle S^{z}\right\rangle\left\langle S^{z}S^{z}\right\rangle + 2\left\langle S^{z}\right\rangle^{3} + 2\left\langle S^{z}S^{z}\right\rangle - S(S+1) - \left\langle S^{z}\right\rangle\right] - \\ &\left.\delta_{4}^{B}\left[S(S+1)\left\langle S^{z}\right\rangle - 3\left\langle S^{z}\right\rangle\left\langle S^{z}S^{z}\right\rangle + 2\left\langle S^{z}\right\rangle^{3} - 2\left\langle S^{z}S^{z}\right\rangle + S(S+1) - \left\langle S^{z}\right\rangle\right]\right\},\end{aligned} \tag{3.56}$$

$$\begin{aligned}\frac{d}{dt}\left\langle S^{z}S^{z}\right\rangle = 2g^{2}&\left\{\alpha_{2}^{B}\left[2S(S+1)\left\langle S^{z}\right\rangle - 6\left\langle S^{z}\right\rangle\left\langle S^{z}S^{z}\right\rangle + 4\left\langle S^{z}\right\rangle^{3} - 3\left\langle S^{z}S^{z}\right\rangle + S(S+1) - \left\langle S^{z}\right\rangle\right] - \right. \\ &\left.\alpha_{2}^{A}\left[2S(S+1)\left\langle S^{z}\right\rangle - 6\left\langle S^{z}\right\rangle\left\langle S^{z}S^{z}\right\rangle + 4\left\langle S^{z}\right\rangle^{3} + 3\left\langle S^{z}S^{z}\right\rangle - S(S+1) - \left\langle S^{z}\right\rangle\right]\right\} + \\ 4g^{4}&\left\{\alpha_{4}^{A}\left[S^{2}(S+1)^{2} + 3\left\langle S^{z}S^{z}\right\rangle\left\langle S^{z}S^{z}\right\rangle - 2\left\langle S^{z}\right\rangle^{4} + 5\left\langle S^{z}S^{z}\right\rangle - 2S(S+1)\left\langle S^{z}S^{z}\right\rangle\right.\right. \\ &-12\left\langle S^{z}\right\rangle\left\langle S^{z}S^{z}\right\rangle + 8\left\langle S^{z}\right\rangle^{3} + 4S(S+1)\left\langle S^{z}\right\rangle - 2S(S+1) - 2\left\langle S^{z}\right\rangle\Big] + \\ &\alpha_{4}^{B}\left[S^{2}(S+1)^{2} + 3\left\langle S^{z}S^{z}\right\rangle\left\langle S^{z}S^{z}\right\rangle - 2\left\langle S^{z}\right\rangle^{4} + 5\left\langle S^{z}S^{z}\right\rangle - 2S(S+1)\left\langle S^{z}S^{z}\right\rangle\right. \\ &\left.+12\left\langle S^{z}\right\rangle\left\langle S^{z}S^{z}\right\rangle - 8\left\langle S^{z}\right\rangle^{3} - 4S(S+1)\left\langle S^{z}\right\rangle - 2S(S+1) + 2\left\langle S^{z}\right\rangle\right] + \\ &\beta_{4}^{A}\left[S^{2}(S+1)^{2} + 3\left\langle S^{z}S^{z}\right\rangle\left\langle S^{z}S^{z}\right\rangle - 2\left\langle S^{z}\right\rangle^{4} + \left\langle S^{z}S^{z}\right\rangle - 2S(S+1)\left\langle S^{z}S^{z}\right\rangle\right. \\ &\left.-6\left\langle S^{z}\right\rangle\left\langle S^{z}S^{z}\right\rangle + 4\left\langle S^{z}\right\rangle^{3} + 2S(S+1)\left\langle S^{z}\right\rangle\right] + \\ &\beta_{4}^{B}\left[S^{2}(S+1)^{2} + 3\left\langle S^{z}S^{z}\right\rangle\left\langle S^{z}S^{z}\right\rangle - 2\left\langle S^{z}\right\rangle^{4} + \left\langle S^{z}S^{z}\right\rangle - 2S(S+1)\left\langle S^{z}S^{z}\right\rangle\right. \\ &\left.+6\left\langle S^{z}\right\rangle\left\langle S^{z}S^{z}\right\rangle - 4\left\langle S^{z}\right\rangle^{3} - 2S(S+1)\left\langle S^{z}\right\rangle\right] -\end{aligned} \tag{3.57}$$

$$
\begin{aligned}
&\gamma_4^X \left[S^2(S+1)^2 + 3\langle S^zS^z\rangle\langle S^zS^z\rangle - 2\langle S^z\rangle^4 - \langle S^zS^z\rangle - 2S(S+1)\langle S^zS^z\rangle\right] + \\
&\gamma_4^A \left[S(S+1)\langle S^zS^z\rangle - 3\langle S^zS^z\rangle\langle S^zS^z\rangle + 2\langle S^z\rangle^4 + 3\langle S^z\rangle\langle S^zS^z\rangle - 2\langle S^z\rangle^3\right] + \\
&\gamma_4^B \left[S(S+1)\langle S^zS^z\rangle - 3\langle S^zS^z\rangle\langle S^zS^z\rangle + 2\langle S^z\rangle^4 - 3\langle S^z\rangle\langle S^zS^z\rangle + 2\langle S^z\rangle^3\right] - \\
&\delta_4^A \Big[S(S+1)\langle S^zS^z\rangle - 3\langle S^zS^z\rangle\langle S^zS^z\rangle + 2\langle S^z\rangle^4 + 9\langle S^z\rangle\langle S^zS^z\rangle - 6\langle S^z\rangle^3 \\
&\quad -2S(S+1)\langle S^z\rangle - 3\langle S^zS^z\rangle + S(S+1) + \langle S^z\rangle] - \\
&\delta_4^B \Big[S(S+1)\langle S^zS^z\rangle - 3\langle S^zS^z\rangle\langle S^zS^z\rangle + 2\langle S^z\rangle^4 - 9\langle S^z\rangle\langle S^zS^z\rangle + 6\langle S^z\rangle^3 \\
&\quad +2S(S+1)\langle S^z\rangle - 3\langle S^zS^z\rangle + S(S+1) - \langle S^z\rangle]\Big\} .
\end{aligned}
$$

where the coefficients appearing in Eq.(3.56) and Eq.(3.57) are defined as follows:

$$
\begin{aligned}
\alpha_2^{A(B)} &= Q_\mp + Q_\mp^*, \\
\alpha_4^{A(B)} &= 4\left(Q_\mp{}^3 + Q_\mp^{*\,3}\right) + \frac{1}{\kappa}\left(Q_\mp + Q_\mp^*\right)^2, \\
\beta_4^{A(B)} &= \frac{1}{\kappa}\left(Q_\mp + Q_\mp^*\right)^2 - 2\,\mathrm{Re}\left[(Q_\mp{}^2 + Q_-Q_+)Q_\Sigma\right], \\
\gamma_4^{A(B)} &= 8\,\mathrm{Re}\left[(Q_\mp{}^2 + Q_-Q_+)Q_\Sigma\right], \\
\gamma_4^X &= 2\,\mathrm{Re}\left[(Q_- + Q_+)^2Q_\Sigma + 2(Q_- + Q_+^*)^2Q_\Delta\right], \\
\delta_4^{A(B)} &= \frac{4}{\kappa}\left(Q_\mp + Q_\mp^*\right)^2 .
\end{aligned}
$$

When plotting the steady state solution of the above coupled system in function of the atom-photon coupling $g\sqrt{N}$ and comparing to the solution of 4KRE, $\langle S^z\rangle = \sum_M MP_M$, we observe that the two solutions are compatible across a range of N and $g\sqrt{N}$, as shown in Fig.(3.10)a). We also show comparison of the first non-zero eigenvalue in the $k = 0$ sector of the Liouvillian with the eigenvalue found by linearising Eq. (3.56) and Eq. (3.57) around the stationary states, Fig.(3.10)b).

It is useful to note that in the limit $N \to \infty$ the terms with the largest powers of S or $\langle S^z\rangle$ provide a stronger contribution while the remaining terms can be neglected. From this observation one has $\langle S^zS^z\rangle = \langle S^z\rangle^2$, compatible with the shrinking of the probability distribution in Fig.(3.9) and this implies that the dynamics can be described sufficiently

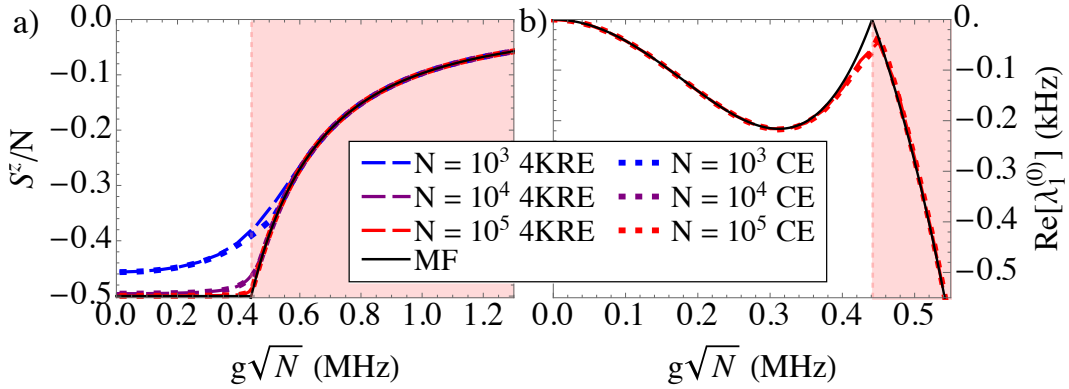

Fig. 3.10. a) Rescaled steady state with $g\sqrt{N}$ in a range of N, comparing 4KRE, the cumulant expansion (CE) and the mean field prediction of the full model. b) Real parts of the eigenvalue associated with the dynamics of S^z. The vertical pink dashed line corresponds to the threshold ($g_c\sqrt{N} = 0.44$ MHz) separating the normal (white) and the superradiant (pink) phase. The black solid line refers to the mean field prediction of the full problem as well as to the mean field limit Eq.(3.58) and Eq.(3.59) of 4KRE. Parameters used are $\omega_0 = 47$ kHz, $\kappa = 8.1$ MHz, $\omega = 5$ MHz. Reprinted figure with permission from R. Palacino and J. Keeling, Phys. Rev. Research **3**, L032016, 2021. Copyright (2021) by the American Physical Society.

well by the equation for $\langle S^z\rangle$ in such a limit. Equation (3.56) thus reduces to:

$$\partial_t\langle S^z\rangle = \left[-2g^2\mu + 2g^4\nu\,\langle S^z\rangle\right]\left[S^2 - \langle S^z\rangle^2\right], \tag{3.58}$$

where $\mu = 2\,\mathrm{Re}[Q_- - Q_+]$ and $\nu = 8\,\mathrm{Re}[(Q_- + Q_+)^2 Q_\Sigma] - 16\kappa^{-1}[\mathrm{Re}(Q_-)^2 + \mathrm{Re}(Q_+)^2]$. We can also linearise Eq.(3.58) and find the eigenvalue associated with the dynamics of $\langle S^z\rangle$ in the thermodynamic limit:

$$\lambda_{\mathrm{MF}} = 4g^2\mu\langle S^z\rangle_{\mathrm{ss}} + 2g^4\nu\left(S^2 - 3\langle S^z\rangle_{\mathrm{ss}}^2\right), \tag{3.59}$$

which appears in Fig.(3.10)b) as the solid black line. In the next section, we will go back to the form of 4KRE to investigate whether it could be manipulated to obtain a positive density matrix equation, thus in Lindblad form.

3.2.5 Lindblad form of 4KRE

As observed previously, Eq. (3.36) satisfies some requirements for an effective theory such as, Hermiticity and trace preservation. Also, the presence of equal numbers of raising

and lowering operators is an indicator of U(1) symmetry that the model mantains in its derivation and this confers the equation a secularised form. Here, we want to discuss whether the 4KRE describes a positive dynamics, or equivalently whether Eq. (3.36) can be cast in Lindblad form. Verifying that our equation of motion describes a positive dynamics means in practice diagonalising the Lindblad–Kossakowski matrix, constructed from Eq.(3.37) and searching for any non-positive eigenvalue in its real part. We follow the approach in [19] and begin with casting $\dot{\rho} = \mathcal{M}\rho$, in matrix form:

$$\dot{\rho}_{mn} = \mathcal{M}_{nmpq}\rho_{pq}. \tag{3.60}$$

We then rewrite Eq. (3.60) using a basis of linearly independent $N \times N$ matrices spanning the Hilbert space. To do this, two sets of basis matrices will be involved in the process. The first is the element basis O_i, with $i = 0, ...N^2 - 1$, whose definition is $[O_i]_{j,k} = \delta_{j,Q_{i,N}}\delta_{k,R_{i,N}}$ where $Q_{i,N}$ and $R_{i,N}$ are respectively the quotient and the remainder of i modulo N. The second set is the normalised generalised Gell–Mann (gGM) basis, γ_i, discussed in section 2.1, with $i = 0, ...N^2 - 1$. These basis matrices are defined by $Tr(\gamma_i\gamma_j) = \delta_{ij}$. The identity matrix is included in this set as $\gamma_0 = \mathbf{1}_N/\sqrt{N}$. Then the following N matrices, $p = 1 \ldots N$ are diagonal matrices with the first p diagonal elements set to 1, then the following element is $-p$, and the remaining elements set to 0, i.e. $\gamma_p = \text{diag}(1, 1, \ldots, -p, 0, 0, \ldots)/\sqrt{p(1+p)}$. The matrices remaining to complete the basis are off-diagonal, defined by:

$$[\gamma^x_{IJ}]_{ij} = \frac{1}{\sqrt{2}}(\delta_{iI}\delta_{jJ} + \delta_{iJ}\delta_{jI}), [\gamma^y_{IJ}]_{ij} = \frac{i}{\sqrt{2}}(\delta_{iI}\delta_{jJ} - \delta_{iJ}\delta_{jI}), \tag{3.61}$$

identified by ordered pairs of integers $I > J$. The reason to make use of two bases is because it is simplest to express $\mathcal{M}$ in the element basis, but the Lindblad–Kossakowski matrix can be found with a basis including explicitly the identity matrix as one of the elements. As said above, we start by writing the density matrix equation in terms of the element basis as:

$$\dot{\rho} = \sum_{i,j} L^O_{ij} O_i \rho O^\dagger_j. \tag{3.62}$$

We then sum over the quotient and remainders of i, j, and introduce the function $I(Q,R) = QN + R$, to obtain the matrix element of ρ:

$$\begin{aligned}\dot{\rho}_{nm} &= \langle n| \sum_{QR,Q'R'} L^O_{I(Q,R),I(Q',R')} O_{QR}\rho O_{R'Q'}|m\rangle \\ &= \sum_{R,R'} L^O_{I(n,R),I(m,R')}\rho_{RR'}.\end{aligned} \tag{3.63}$$

Therefore, comparing with Eq. (3.60), we get:

$$L^O_{I(n,p),I(m,q)} = \mathcal{M}_{nmpq}. \tag{3.64}$$

Finding L^γ in the generalised Gell–Mann basis implies a basis transformation, so we express the relation between the two set basis according to $O_i = X_{ij}\gamma_j$ where $X_{ij} = Tr(O_i\gamma_j)$. We thus finally find:

$$\dot{\rho} = \sum_{ij}\sum_{kl} L^O_{kl} X_{ki}\gamma_i\rho[X_{lj}\gamma_j]^\dagger \equiv \sum_{ij} L^\gamma_{ij}\gamma_i\rho\gamma_j, \tag{3.65}$$

where it is assumed $\gamma_i^\dagger = \gamma_i$ and $\mathbf{L}^\gamma$ relates to the element basis representation by means of the transformation X_{ij}: $\mathbf{L}^\gamma = \mathbf{X}^T\mathbf{L}^O\mathbf{X}^*$. Recalling that the generalised Gell–Mann basis includes the identity matrix as element 0, we can write the density matrix equation in the form of Eq.(2.24) [19]:

$$\dot{\rho} = -i[H,\rho] + \sum_{i,j=1}^{N^2-1} L^\gamma_{ij}\left(\gamma_i\rho\gamma_j - \frac{1}{2}\left\{\rho,\gamma_j\gamma_i\right\}\right), \tag{3.66}$$

where the Hamiltonian is defined as:

$$H = \sum_{i=1}^{N^2-1} \frac{L^\gamma_{0i} - L^\gamma_{i0}}{2i\sqrt{N}}\gamma^i. \tag{3.67}$$

Since our original aim was constructing the Lindblad–Kossakowski matrix from our atom-only theory, this is achieved by taking $\mathbf{L}^\gamma$ and excluding row and column 0. When we carry out this operation numerically and diagonalise the resulting submatrix, we find that the spectrum is not positive in its real part. This proves that 4KRE, despite being a

secularised equation, is not in Lindblad form. It is worth recalling that the Lindblad form is usually found by means of secularisation of the effective theory [97], that is removing time-dependent contributions in the interaction picture. In our case, the $U(1)$ symmetry, guaranteed by equal numbers of raising and lowering operators in the equation, implies that 4KRE is time-independent in the interaction picture. However, the 4KRE provides an equation for which secularisation does not guarantee positivity. It is worth mentioning that, the equation of motion of a reduced system, obtained with a Redfield theory, is a working tool in capturing the essential features of the dynamics even when the theory does not preserve positivity, as reported in several contexts [136, 93, 94, 95, 91].

3.2.6 Liouvillian spectrum: U(1) vs $\mathbb{Z}_2$ Dicke model

In section 3.2.3 we have analysed the spectral properties of 4KRE with particular interest to the Liouvillian gap and its scaling behaviour with system size. Here, starting from the results discussed in [91], we want to address the spectral characteristics of the Liouvillian superoperator of the single mode $\mathbb{Z}_2$ Dicke model. Let us begin by reproposing the Redfield (atom-only) equation of motion of the single-mode Dicke model and its matrix form [91]:

$$\begin{aligned}\dot{\rho} = -i[\omega_0 S^z, \rho] - g^2 \big\{ & Q_+(S^+S^+\rho - S^+\rho S^+) + Q_-(S^+S^-\rho - S^-\rho S^+) + \\ & Q_+(S^-S^+\rho - S^+\rho S^-) + Q_-(S^-S^-\rho - S^-\rho S^-) + \text{h.c.}\big\}\end{aligned} \tag{3.68}$$

$$\begin{aligned}\dot{\rho}_{M,M+k} = i\omega_0 k \rho_{M,M+k} - g^2 \Big\{ & \xi Q_+ \left(f^{M-1} f^{M-2} \rho_{M-2,M+k} - f^{M-1} f^{M+k} \rho_{M-1,M+k+1} \right) + \\ & Q_- \left(f^{M-1} f^{M-1} \rho_{M,M+k} - f^{M} f^{M+k} \rho_{M+1,M+k+1} \right) + \\ & Q_+ \left(f^{M} f^{M} \rho_{M,M+k} - f^{M-1} f^{M+k-1} \rho_{M-1,M+k-1} \right) + \\ & \xi Q_- \left(f^{M} f^{M+1} \rho_{M+2,M+k} - f^{M} f^{M+k-1} \rho_{M+1,M+k-1} \right) + \\ & \xi Q_-^* \left(f^{M+k+1} f^{M+k} \rho_{M,M+k+2} - f^{M-1} f^{M+k} \rho_{M-1,M+k+1} \right) + \\ & Q_-^* \left(f^{M+k-1} f^{M+k-1} \rho_{M,M+k} - f^{M} f^{M+k} \rho_{M+1,M+k+1} \right) + \\ & Q_+^* \left(f^{M+k} f^{M+k} \rho_{M,M+k} - f^{M-1} f^{M+k-1} \rho_{M-1,M+k-1} \right) + \\ & \xi Q_+^* \left(f^{M+k-2} f^{M+k-1} \rho_{M,M+k-2} - f^{M} f^{M+k-1} \rho_{M+1,M+k-1} \right) \Big\}\end{aligned} \tag{3.69}$$

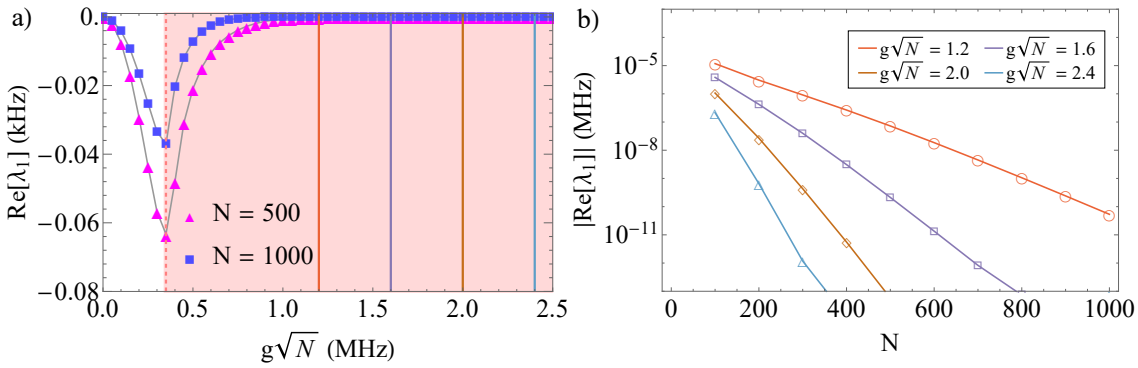

Fig. 3.11. Similar figure to Fig.(3.8) showing the spectral gap predicted by the second order Redfield equation of the single mode Dicke model with $\mathbb{Z}_2$ symmetry breaking. a) displays the gap closure with $g\sqrt{N}$ at fixed N while b) displays the scaling law with N at 4 values of $g\sqrt{N}$. Parameters used are $\omega_0 = 10$ kHz, $\kappa = 8.1$ MHz, $\omega = 5$ MHz. Reprinted figure with permission from R. Palacino and J. Keeling, Phys. Rev. Research **3**, L032016, 2021. Copyright (2021) by the American Physical Society.

where $Q_\pm = [\kappa + i(\omega \pm \omega_0)]^{-1}$ and it is possible to switch between the secularised, $\xi = 0$ and the unsecularised form, $\xi = 1$, of the equation.

With these results, the authors in [91] prove that the unsecularised form of the Redfield equation recovers the damped dynamics of the spin system, predicting the expected super-radiant phase transition. While that work reports on the solutions of the equation in terms of steady states, it does not however address the analysis of the soft modes arising from the $\mathbb{Z}_2$ symmetry-breaking; we thus carry out a complementary analysis by investigating the behavior of the spectral gap with the coupling strength and system size.

While in the U(1) case, the Liouvillian can be decomposed into independent sectors of the dynamics due to the symmetry of the problem, in the single-mode Dicke model, according to Eq.(3.69), no such division occurs in the density matrix equation. Therefore, studying the gap for comparably high N values is challenging due to the necessity of diagonalising the complete Liouvillian matrix.

As a consequence of the lack in a net separation of the sectors, we would just need to sort the spectrum according to the definition Eq.(2.61), remembering that the Liouvillian gap is the first non-zero eigenvalue with the smallest real part. This is shown in Fig.(3.11)a) for the $\mathbb{Z}_2$ Dicke model.

There are three key features arising from the comparison with Fig.(3.8): firstly, the second order Redfield theory is sufficient to describe a vanishing mode as one enters the

superradiant phase. Secondly, there is no need to compute the gap for large values of N if compared to the U(1) model, in order to prove that the gap is going to be effectively 0 for $N \to \infty$. In fact, when looking at Fig.(3.11), a closure appears even for 500 spins. Lastly, the scaling law of the gap with system size has a different form from that discussed in section 3.2.3 for the U(1) model. While for the two-mode problem, the variation of the gap is linear with the inverse of N, $\lambda_0^{(1)} = A + B/N$, in the single-mode case, the gap reduces exponentially when increasing the number of atoms, $\lambda_1 \propto \exp(-CN)$, as shown in Fig.(3.11)(b).

3.3 Conclusive remarks

Here, we summarise the results of the chapter and identify directions for future work.
The results of the theoretical study conducted in Ref.[17] on a class of Hamiltonians with U(1) symmetry, introduced and discussed in section 1.4, has been used as a reference for the validation of an effective atom-only theory derived in the context of the Redfield theory [90, 19].
From the comparison with the complete atom-cavity problem, it was found that the resulting density matrix equation of second order in the light-matter coupling (g^2) fails to predict the symmetry-breaking superradiant phase transition. The deviation from the predictions of the full atom-cavity model is corrected when we include the fourth order contribution (g^4) in this reduced atom-only description, derived with the technique of the irreducible Keldysh diagrams [99], introduced and discussed in section 2.3. The new theory, 4KRE, is Hermitian, preserves the trace, and respects the U(1) symmetry (this latter property is reflected by its secularised form, i.e. the equation is time-independent in the interaction picture). Moreover, the U(1) symmetry confers the Liouvillian a macro-structure made of independent sectors of the dynamics, with each one being a penta-diagonal matrix. We began by analysing the symmetry-preserving sector ($k = 0$) containing information about the dynamics of symmetric variables such as S^z. Within this sector, 4KRE recovers the steady state solutions and the relaxation rates towards those solutions predicted by the full problem, thus recovering the superradiance transition at the expected critical coupling strength.
We have proved how a "naive" mean field treatment is inadequate for finite size systems, while a cumulant expansion truncated at the second order is supported by the Gaussian

nature of the steady state probability distribution. The study of this probability reveals how a mean field approximation becomes justified in the limit of an infinite number of atoms.

In addition to the stationary solutions, our goal is identifying the low-energy mode, or Liouvillian gap, associated with the breaking of the U(1) and this information has to be searched for in the symmetry breaking sectors of the Liouvillian. By definition, the Liouvillian gap is the eigenvalue with the smallest (non-zero) real part, becoming vanishing in the symmetry-broken phase. In our case, this is to be found in the sectors adjacent to $\mathcal{L}^{(0)}$, that are the Hermitian conjugate matrices $\mathcal{L}^{(\pm 1)}$ ($k = \pm 1$). We find that the smallest eigenvalue in those sectors have a finite gap above the critical point which is expected even for large but finite system sizes. However, numerical evaluation of the gap value for $N \to \infty$ reveals that a finite gap persists also in that limit. To verify that an analogous issue was not occurring in the $k = 0$ sector, we tested the convergence of the steady state predicted by 4KRE to the exact normal state for $N \to \infty$, finding that it is fully recovered in that asymptotic limit.

To investigate the lack of a vanishing mode in this two-mode Dicke model with U(1) symmetry, we considered the single mode Dicke model with $\mathbb{Z}_2$ symmetry. In Ref.[91], the Dicke model is analysed from the point of view of the standard second order Redfield theory but the analysis of the vanishing modes is missing there. We thus address this aspect and find that the second order Redfield theory captures a vanishing mode above the critical point. It is worth noting that the way the spectral gap scales with system size is different, linear in the U(1) model and exponential in the $\mathbb{Z}_2$ problem.

The last aspect we covered in this chapter was whether 4KRE could be manipulated to provide an equation in Lindblad form. By numerically evaluating the Lindblad–Kossakowski matrix and its eigenspectrum, we found that, although 4KRE is in a secularised form (because of the U(1) symmetry), it does not describe a positive dynamics.

From the summary done above, we might try to connect the absence of a vanishing mode in this higher order atom-only theory with the aspects explored in this chapter.

First of all, we might ask whether such behavior could be due to the fact that contributions beyond the fourth order are needed to fully catch a vanishing mode in a two-mode model with continuous symmetry.

Moreover, while the second order contribution (2RE), which is naturally in a secularised form for symmetry reasons, can be written in Lindbald form, see Eq.(3.29), the fourth

Model	Perturbative order	Phase transition?	Lindblad form?	Zero mode?
1 mode $\mathbb{Z}_2$	2^{nd} order	✓	✗	✓
	4^{th} order [137]	✓	✗	✗
2 modes U(1)	2^{nd} order	✗	✓	✗
	4^{th} order	✓	✗	✗

order contribution, also automatically in a secularised form for the same reasons, does not preserve positivity. It is worth reminding that, typically, invoking the secular approximation provides a density matrix equation ensuring positivity, thus in Lindblad form. In this regard, we might ask whether this feature of 4KRE plays a role in preventing the observation of the vanishing mode or whether it is possible to verify that the inclusion of terms from higher order contributions in the diagrammatic expansion might restore the Lindblad form.

However, the hypothesis of a missing zero mode due to a non-positive dynamics is not sufficiently robust, since there is at least another example of non-positive Redfield theory, in the case of the single mode Dicke model with $\mathbb{Z}_2$ symmetry, capturing both the steady states and a vanishing Liouvillian gap, as we have noted.

Moreover, according to the conclusions reached in the master thesis by Oscar Chang [137], while the second order Redfield theory does predict a vanishing Liouvillian gap, the inclusion of the fourth order contribution evaluated with the Keldysh diagrammatic expansion causes the gap to acquire a non-vanishing value in the symmetry-broken phase. We thus report a second case where a fourth order Keldysh-Redfield theory fails to predict a zero mode associated with the symmetry breaking of the model.

For convenience, we collect the main points explored here in the table above for a better comparison between the models.

Chapter 4

Multimode Dicke model

In this chapter, we are going to study the dynamics of spin systems coupled to multiple light fields in a cavity-QED setup, thus realising a multimode regime of the $\mathbb{Z}_2$ Dicke model. The Hamiltonian is presented in section 1.5, Eq.(1.50) and reproduced here for convenience:

$$\begin{aligned} \dot{\rho} &= -i[H,\rho] + \kappa \sum_m \mathcal{D}[a_m] \\ H &= \sum_m \omega_m a_m^\dagger a_m + \omega_0 \sum_{i=1}^{N_E} S_i^z + g \sum_m \sum_{i=1}^{N_E} \eta_{im} S_i^x (a_m^\dagger + a_m). \end{aligned} \tag{4.1}$$

For an easy reference, we briefly recall the main parameters of the model: we have a total number N of spins-1/2, whose energy is proportional to ω_0, divided in N_E tightly localised ensembles within the cavity. Each ensemble is composed by M_i spins so that $\sum_{i=1}^{N_E} M_i = N$ and behaves as a collective spin $S_i = M_i/2$. The spin ensembles interact with, in principle, an infinite number of modes a_m, each one decaying at a rate κ. ω_m is the frequency detuning between each cavity mode and the pump, and the dispersion relation in the near degenerate regime is given by $\omega_m = \omega_c + \epsilon\delta\omega_m$, with $\epsilon \ll 1$ and ω_c is the bare cavity frequency. Lastly, η_{im} provides a coupling parameter between the ith spin ensemble and the mth mode, while g gives an overall coupling strength between atoms and modes.

As it will be discussed in more detail later in section 4.1, we are going to re-formulate the problem in terms of a new basis of modes to account for a finite set of modes, as opposed to the infinite basis defined in the model above. This formulation will be used to write

a Redfield theory, described in section 4.2, in order to reduce the number of degrees of freedom involved. We are then going to discuss mean field and cumulant equations of motion whose derivation and dynamics are described in sections 4.3 and 4.4, respectively. This chapter will present preliminary results obtained within a collaboration with Benjamin Lev's group at Stanford University. Starting from the consideration that the cavity QED system with multiple atomic ensembles realises frustrated spin models, the aim of the research project is to explore how good the cavity QED system is as a route to find the ground state of these models and how this ability scales with problem size and parameter configurations.

4.1 Supermode theory

As the multimode model given in Eq.(4.1) describes atomic spins coupled to a potentially infinite number of cavity modes, we should find a better description to make calculations and analysis simpler. It is worth noting that when one wishes to take into account the spatial structure of the cavity field, atoms do not interact with the electromagnetic modes in the same way; depending on the spatial profile of the field and the distribution of the atoms in the cavity, some spins are more strongly coupled to certain superpositions of modes and weakly with others [68, 64]. For brevity, we are going to refer to any superposition of modes with the term "supermode" [65].

Let us start to introduce a formal notion of supermode to then see how this formulation modifies the interaction with the spins. A supermode can be formally written as

$$\tilde{a} = \sum_{m=1}^{N_m} x_m a_m = \mathbf{x} \cdot \mathbf{a}, \tag{4.2}$$

a weighted sum of modes where the components of the vector $\mathbf{x} = (x_1, x_2, ..., x_{N_m})$ correspond to the weights of each mode and $\mathbf{a} = (a_1, a_2, ..., a_{N_m})$ is the vector of the cavity operators. According to the definition above, the commutation relation between two supermodes $\tilde{a}$ and $\tilde{b}$, identified by weight vectors $\mathbf{x}$ and $\mathbf{y}$ respectively, is $[\tilde{a}, \tilde{b}^\dagger] = \mathbf{x} \cdot \mathbf{y}$ and $[\tilde{a}, \tilde{b}] = [\tilde{a}^\dagger, \tilde{b}^\dagger] = 0$. This indicates that two supermodes are linearly independent when their weight vectors are orthogonal.

At this point, we can consider the idea of using supermodes as a basis to express the

interaction with the spin ensembles. As mentioned above, we want to introduce a basis where only a subset of supermodes can be considered effectively coupled to the spins, while the remaining set, being weakly coupled or decoupled, can be eliminated by means of the Redfield approach.

In such a basis, we begin by identifying those supermodes that are decoupled from the ensembles. When we substitute Eq.(4.2) in the Hamiltonian model Eq.(4.1), the coupling strength between a spin ensemble and the supermode becomes $\alpha_i = g \sum_{m=1}^{N_m} x_m \eta_{im}$, or in matrix notation, $\boldsymbol{\alpha} = \eta \mathbf{x}$ to indicate the coupling with each ensemble and η represents the matrix of the couplings η_{im}. For a supermode to be decoupled from one or more spin ensembles, its coupling strength with that/those ensembles must be vanishing, $\boldsymbol{\alpha} = 0$. This condition is satisfied by all those weight vectors belonging to the kernel of η, $\forall \mathbf{x} \in \ker(\eta)$. Therefore, all supermodes whose vector $\mathbf{x}$ belongs to the kernel of η are automatically decoupled from every ensemble. We thus know that, given the matrix η of the couplings from Eq.(4.1), when we construct a basis with a total number N_m of supermodes, $\text{rank}(\eta)$ is the number of supermodes that couples to the spins, while the remaining $N_m - \text{rank}(\eta)$ are decoupled supermodes.

The simplest picture we could consider is a supermode whose coupling with a spin ensemble is strictly peaked at the position of the ensemble. We would refer to such field as local supermode. In this picture, we would thus have N_E spin ensembles and supermodes, where each supermode spatially overlaps with a particular spin ensemble. The local supermode can be defined by means of the coupling strengths of the starting model Eq.(4.1) as:

$$A_i = \sum_{m=1}^{N_E} \eta_{im} a_m \tag{4.3}$$

with $i = 1, ..., N_E$. When we adopt this picture, the interaction term becomes $H_I = g \sum_{i=1}^{N_E} S_i^x (A_i + A_i^\dagger)$ which resembles the original form in Eq.(4.1) but with a finite number of fields, N_E, rather than infinite. However, the local supermodes do not describe linearly independent fields subject to canonical commutation laws, as the following expression shows:

$$[A_i, A_j^\dagger] = \sum_{mn} \eta_{im} \eta_{jn} [a_m, a_n^\dagger] = \sum_{mn} \eta_{im} \eta_{jn} \delta_{mn} = \sum_{m} \eta_{im} \eta_{jm} \neq \delta_{ij} \tag{4.4}$$

In order to find a basis with a finite number of field operators, actively involved in the interaction with the spins and obeying canonical commutation rules, we instead need a unitary transformation relating the new operators, the supermodes, and the old basis $\{a_m\}$:

$$b_m = \sum_{n=1}^{N_m} U^b_{mn} a_n. \tag{4.5}$$

The challenge is how to find the best unitary form U. In considering this, there is also a second question: if the modes are not degenerate, the first term in the Hamiltonian in Eq.(4.1) will mix supermodes. We should thus attempt to identify an appropriate way to find the relevant transform. One way to consider this is to note that the multimode Dicke model can be related to an Ising model by applying a transformation known as Lang-Firsov polaron transformation:

$$U_p = \exp\left[g \sum_{i=1}^{N_E} \sum_m \eta_{im} S^x_i \left(\frac{a^\dagger_m}{\omega_m - i\kappa} - \text{H.c.} \right) \right]. \tag{4.6}$$

This transformation applied to the cavity operators produces the following expression:

$$U_p a_m U_p^\dagger = a_m - g \sum_{i=1}^{N_E} \frac{\eta_{im} S^x_i}{\omega_m - i\kappa} \tag{4.7}$$

where the second term on the r.h.s would correspond to the steady state expectation value $\langle a_m \rangle$ obtained by solving the mean field equation of a_m. Thus, the effect of the polaron transform is to shift the cavity operator by the amount $\langle a_m \rangle$. When one applies the transformation to Eq.(4.1), the model becomes:

$$\begin{aligned} \dot{\rho} &= -i[H_p, \rho] + \kappa \sum_m \mathcal{D}\left[a_m - g \sum_{i=1}^{N_E} \frac{\eta_{im} S^x_i}{\omega_m - i\kappa} \right] \\ H_p &= \sum_m \omega_m a^\dagger_m a_m + i\frac{\omega_0}{2} \sum_{i=1}^{N_E} \left(S^{x-}_i D^\dagger_i - S^{x+}_i D_i \right) + \\ &\quad i\kappa g \sum_m \sum_{i=1}^{N_E} \eta_{im} S^x_i \left(\frac{a_m}{\omega_m + i\kappa} - \frac{a^\dagger_m}{\omega_m - i\kappa} \right) - \frac{g^2}{\omega_c} \sum_{i,j=1}^{N_E} J_{ij} S^x_i S^x_j. \end{aligned} \tag{4.8}$$

where $S_i^{x\pm} = S_i^y \pm iS_i^z$ and $D_i = \exp\left[g\sum_m \eta_{im}\left(\frac{a_m^\dagger}{\omega_m - i\kappa} - \text{H.c.}\right)\right]$. As a result of the transformation applied, the last term of Eq.(4.8) makes explicit the connection with the Ising model and the coupling matrix J_{ij} is given by

$$J_{ij} = \omega_c \sum_m \frac{\eta_{im}\eta_{jm}\omega_m}{\omega_m^2 + \kappa^2} \tag{4.9}$$

where the r.h.s resembles the result of the commutation relation between local supermodes seen above, Eq.(4.4), suggesting non local cavity-mediated interactions between ensembles. This justifies why the local supermode picture cannot represent a canonically valid basis of bosonic modes.

If we use a modified version of the coupling matrix η_{im} between modes and ensembles

$$\tilde{\eta}_{im} = \frac{\omega_c \eta_{im}}{\omega_m - i\kappa}, \tag{4.10}$$

to construct a $N_E \times N_E$ positive semi-definite matrix K similar to the connectivity matrix J above, but where ω_m in the expression 4.9 in the numerator is replaced by the bare pump-cavity detuning from the $\text{TEM}_{0,0}$ mode ω_c, i.e:

$$K_{ij} = (\tilde{\eta}\tilde{\eta}^\dagger)_{ij} = \omega_c^2 \sum_{m=1}^{N_m} \frac{\eta_{im}\eta_{jm}}{\omega_m^2 + \kappa^2}, \tag{4.11}$$

and whose eigensystem is defined by $K\mathbf{v}^m = \lambda_m \mathbf{v}^m$ ($\lambda_m \geq 0$), then the unitary matrix U_{mn}^b

$$U_{mn}^b = \begin{cases} \omega_c \lambda_m^{-1/2} \sum_{i=1}^{N_E} \frac{\mathbf{v}_i^m \eta_{in}}{\omega_n + i\kappa} & m \leq R \\ \mathbf{x}_n^m & m > R \end{cases} \tag{4.12}$$

can be given in terms of the eigensystem of the matrix K whose rank is $R = \text{rank}(K) = \text{rank}(\tilde{\eta})$ and $R \leq N_E$. Using Eq.(4.12) in Eq.(4.5) provides a set of supermodes b_m where the first R modes are considered to be interacting with the spin ensembles and the remaining $N_m - R$ are constructed using the basis of vectors of the kernel of $\tilde{\eta}$, the set $\{\mathbf{x}_n^m\}$. The latter will thus be supermodes decoupled from the spins. Let us refer to the coupled supermodes as "active" while those decoupled (or weakly coupled in a near-degenerate limit) as "inactive". To prove that this new set of operators describes

linearly independent harmonic oscillators, we calculate the following commutator using the definitions in Eq.(4.5) and Eq.(4.12)

$$\begin{aligned}[b_\mu, b_\nu^\dagger] &= \omega_c^2(\lambda_\mu\lambda_\nu)^{-1/2}\sum_{k,l=1}^{N_m}\sum_{i,j=1}^{N_E}\frac{\mathbf{v}_i^\mu\eta_{ik}}{(\omega_c+i\kappa)}\frac{\mathbf{v}_j^{\nu T}\eta_{lj}}{(\omega_c-i\kappa)}[a_k, a_l^\dagger] \\ &= \omega_c^2(\lambda_\mu\lambda_\nu)^{-1/2}\sum_{k=1}^{N_m}\sum_{i,j=1}^{N_E}\frac{\mathbf{v}_i^\mu\mathbf{v}_j^{\nu T}\eta_{ik}\eta_{kj}}{\omega_c^2+\kappa^2} \\ &= \frac{1}{(\lambda_\mu\lambda_\nu)^{1/2}}\mathbf{v}^{\nu T}K\mathbf{v}^\mu = \frac{\lambda_\mu}{(\lambda_\mu\lambda_\nu)^{1/2}}\mathbf{v}^{\nu T}\mathbf{v}^\mu = \frac{\lambda_\mu}{(\lambda_\mu\lambda_\nu)^{1/2}}\delta_{\mu\nu}\end{aligned} \tag{4.13}$$

in the passage from the second to the third line, we identify the expression of the matrix K_{ij} Eq.(4.11), and in the last line, we exploit the property of $\mathbf{v}^\mu$ which is an eigenvector of K with eigenvalue λ_μ.

When we use the new basis of supermodes, the model becomes:

$$\dot{\rho} = -i[H_b, \rho] + \kappa\sum_{m=1}^{N_m}\mathcal{D}[b_m] \tag{4.14}$$

$$H_b = \omega_c\sum_{m=1}^{N_m}b_m^\dagger b_m + \epsilon\sum_{m,n=1}^{N_m}\omega_{mn}b_m^\dagger b_n + \omega_z\sum_{i=1}^{N_E}S_i^z + g\sum_{i=1}^{N_E}\sum_{m=1}^{N_m}S_i^x(\alpha_{im}b_m + \alpha_{im}^* b_m^\dagger). \tag{4.15}$$

The couplings are given by $\alpha_{im} = \sum_{n=1}^{N_m}\eta_{in}U_{mn}^{b*}$, recalling that $\alpha_{im} = 0$ for $m > R$ (this reduces the upper limit in the sum of the interaction term to R, the number of supermodes involved in the dynamics with the spins) and $\omega_{mn} = \sum_{l=1}^{N_m}U_{ml}^b U_{nl}^{b*}\delta\omega_l$ are coupling constants between supermodes arising away from the perfect degeneracy configuration. With regards to this additional coupling term between supermodes, we see that the sum can be divided in three independent terms: the first, $\sum_{m,n=1}^{R}$ describing couplings between active supermodes, a second product of sums $\sum_{m,n=R+1}^{N_m}$ relative to couplings between inactive supermodes, and the third $\sum_{m=1}^{R}\sum_{n=R+1}^{N_m}$ which mixes active and inactive supermodes.

At this point, we observe that we may reduce further the number of degrees of freedom. In fact, we may formulate a Redfield theory which will depend on active modes and spin variables only, where we eliminate the weakly coupled inactive modes. This part will be discussed in the next section.

4.2 Atom-active supermodes Redfield theory

Here, we derive an effective atom-active mode theory where we trace out the weakly coupled inactive supermode variables. Let us refer to the inactive supermode operators with the notation $\{B_m\}$, with $m = R+1, ..., N_m$ while we will keep on using the notation $\{b_m\}$, $m = 1, ..., R$ for the active supermodes. We thus start by considering an extended version of the Hamiltonian in Eq.(4.15), which includes an external reservoir of harmonic oscillators A_k coupled to each set of supermodes, similar to the approach adopted in section 3.1:

$$\begin{aligned} H_b = H_0 + H_1 =& \omega_c \sum_{m=1}^{R} b_m^\dagger b_m + \omega_c \sum_{m=R+1}^{N_m} B_m^\dagger B_m + \epsilon \sum_{m,n=1}^{R} \omega_{mn} b_m^\dagger b_n + \\ & \epsilon \sum_{m,n=R+1}^{N_m} \omega_{mn} B_m^\dagger B_n + g \sum_{i=1}^{N_E} \sum_{m=1}^{R} \alpha_{im} S_i^x (b_m + b_m^\dagger) + \\ & \sum_k \omega_k A_k^\dagger A_k + \sum_k \sum_{m=1}^{R} g_{k,m} (b_m A_k^\dagger + b_m^\dagger A_k) + \\ & \sum_k \sum_{m=R+1}^{N_m} g_{k,m} (B_m A_k^\dagger + B_m^\dagger A_k) + \\ & \epsilon \sum_{m=1}^{R} \sum_{n=R+1}^{N_m} \omega_{mn} (b_m^\dagger B_n + b_m B_n^\dagger) \end{aligned} \tag{4.16}$$

where, as said, b_m and B_m are annihilation operators of the active and inactive modes, respectively. The spectral density of the A_k modes satisfies $\sum_k g_{k,m}^2 \pi \delta(\nu_k - \nu) = \kappa$.

In order to derive the Redfield equation, we have to identify the interaction Hamiltonian appearing in the standard Redfield formula. This is given by the interaction term between active and inactive modes in the model above, that is the last term in Eq.(4.16):

$$H_1 = \epsilon \sum_{m=1}^{R} \sum_{n=R+1}^{N_m} \omega_{mn} (b_m^\dagger B_n + b_m B_n^\dagger) \tag{4.17}$$

In our description, we are going to consider spins and active modes to be the system and all the other modes (inactive and extra-cavity modes) to be the bath. For the derivation of the Redfield equation, we are going to neglect the term proportional to ω_z in the Hamiltonian.

This approximation is at least valid deep in the superradiant phase. The master equation to be derived is re-proposed here for convenience:

$$\dot{\rho}_s = -\int_0^t dt' Tr_B([H_1(t), [H_1(t'), \rho(t)]]) \tag{4.18}$$

where H_1 is in the interaction picture with respect to H_0:

$$H_1(t) = \epsilon \sum_{m=1}^{R} \sum_{n=R+1}^{N_m} \omega_{mn}(b_m^\dagger(t)B_n(t) + b_m(t)B_n^\dagger(t)) \tag{4.19}$$

As a useful reminder, to evaluate the above integral Eq.(4.18), we will make use of two approximations: the Born approximation which assumes the total density matrix to be in a factorised state $\rho_{tot} = \rho_s \otimes \rho_B$ and the Markov approximation which allows to neglect memory effects in the state of the system, therefore considering ρ at the present time t in the integral. To proceed, we need to know the two-time correlation functions of the inactive modes $\langle B_p(t)B_q^\dagger(t')\rangle$ and the time dependence of the active modes $b_m(t)$. The correlations of the inactive modes can be found by first solving coupled equations of motion for the B_k and A_k modes, as we have also done in the U(1) symmetry problem in section 3.1. In the following we shall consider $\epsilon = 0$ in the unperturbed Hamiltonian H_0 for simplicity

$$\begin{aligned}\dot{B}_k &= -i[B_k, \omega_c \sum_{m=R+1}^{N_m} B_m^\dagger B_m] - i\sum_{k'} \sum_{m=R+1}^{N_m} g_{k',m}[B_k, B_m^\dagger A_{k'} + h.c] \\ &= -i\omega_c B_k - i\sum_{k'} g_{k',k}A_{k'}\end{aligned} \tag{4.20}$$

$$\begin{aligned}\dot{A}_{k'} &= -i[A_{k'}, \sum_k \omega_k A_k^\dagger A_k] - i\sum_k g_{k',k}[A_{k'}, B_k^\dagger A_k + h.c] \\ &= -i\omega_k A_{k'} - ig_{k',k}B_k\end{aligned} \tag{4.21}$$

The solution of Eq.(4.21),

$$A_k = A_k(0)e^{-i\omega_k t} - i\sum_{m=R+1}^{N_m} g_{k,m}\int_0^t dt' e^{-i\omega_k(t-t')}B_m(t'), \tag{4.22}$$

is then substituted into Eq.(4.20) to give

$$\begin{aligned}\dot{B}_k =& -i\omega_c B_k - i\sum_{k'} g_{k',k} A_{k'}(0) e^{-i\omega_{k'}t} - \sum_{k'} g_{k',k}^2 \int_0^t dt' e^{-i\omega_{k'}(t-t')} B_k(t') \\ =& -i\omega_c B_k + \xi_{A_k}(t) - \kappa B_k\end{aligned} \tag{4.23}$$

In the above Eq.(4.23), we used the expression of the bath spectral density $\sum_{k'} g_{k',k}^2 e^{-i\omega_{k'}(t-t')} = \kappa\delta(t-t')$ and identified the second term of the equation with the stochastic force $\xi_{A_k}(t)$, characterised by a vanishing expectation value, $\langle \xi_{A_k}(t)\rangle = 0$, and a two-time correlation function peaked at the present time t, $\langle \xi_{A_k}(t)\xi^\dagger_{A_{k'}}(t')\rangle = 2\kappa\delta(t-t')\delta_{kk'}$.

The complete solution of Eq.(4.23) is

$$B_k(t) = B_k^{OM}(t) + B_k^P(t) = B_k(0)e^{-(i\omega_c+\kappa)t} + \int_0^t dt' e^{-(i\omega_c+\kappa)(t-t')}\xi_{A_k}(t') \xrightarrow[t\to\infty]{} B_k^P(t) \tag{4.24}$$

and, in the long time limit, the B_k approaches the particular solution, $B_k^P(t)$. The two-time correlation of the inactive modes is thus given by

$$\begin{aligned}\langle B_k(t)B^\dagger_{k'}(t)\rangle =& \int_0^t d\tau \int_0^{t'} d\tau' \langle \xi_{A_k}(\tau)\xi^\dagger_{A_{k'}}(\tau')\rangle e^{-(i\omega_c+\kappa)(t-\tau)} e^{(i\omega_c-\kappa)(t'-\tau')} \\ =& e^{-i\omega_c(t-t')-\kappa|t-t'|}\delta_{kk'}\end{aligned} \tag{4.25}$$

Now we need to know the expression of the active mode operator in the interaction picture. This is given by:

$$b_m(t) = e^{iH_0t} b_m e^{-iH_0t} = U^\dagger e^{iUH_0U^\dagger t} U b_m U^\dagger e^{-iUH_0U^\dagger t} U \tag{4.26}$$

where we used the following transformation

$$U = \exp\left(\sum_{i=1}^{N_E}\sum_{m=1}^{R} \frac{g\alpha_{im}}{\omega_c} S_i^x (b_m^\dagger - b_m)\right). \tag{4.27}$$

For the above transformation to be unitary, we impose $\alpha_{im} \in \mathbb{R}$.

In order to attain the final form of the expression Eq.(4.26) necessary for solving Eq.(4.18),

we are going to evaluate first $Ub_mU^\dagger$:

$$Ub_mU^\dagger = b_m + \sum_{i,m'} \frac{g\alpha_{im'}}{\omega_c} S_i^x [b_{m'}^\dagger - b_{m'}, b_m] = b_m - \sum_{i=1}^{N_E} \frac{g\alpha_{im}}{\omega_c} S_i^x \tag{4.28}$$

where terms containing multiple commutators such as, $[b_{m'}^\dagger - b_{m'}, [b_{m''}^\dagger - b_{m''}, b_m]] = 0$ Then, we evaluate $UH_0U^\dagger$:

$$\begin{aligned}
UH_0U^\dagger =& U(\omega_c \sum_{m=1}^{R} b_m^\dagger b_m + g \sum_{i=1}^{N_E} \sum_{m=1}^{R} \alpha_{im} S_i^x (b_m + b_m^\dagger))U^\dagger \\
&= \omega_c \sum_m b_m^\dagger b_m + \sum_m \sum_{im'} g\alpha_{im'} S_i^x [b_{m'}^\dagger - b_{m'}, b_m^\dagger b_m] + \\
&+ \frac{1}{2}\frac{g^2}{\omega_c} \sum_{m,m',m''} \sum_{ij} \alpha_{im'}\alpha_{jm''} S_i^x S_j^x [b_{m'}^\dagger - b_{m'}, [b_{m''}^\dagger - b_{m''}, b_m^\dagger b_m]] + \\
&+ g \sum_{i,m} \alpha_{im} S_i^x (b_m + b_m^\dagger) + \frac{g^2}{\omega_c} \sum_{m,m'} \sum_{ij} \alpha_{im}\alpha_{jm'} S_i^x S_j^x [b_{m'}^\dagger - b_{m'}, b_m^\dagger + b_m] \\
&= \omega_c \sum_m b_m^\dagger b_m - \frac{g^2}{\omega_c} \sum_m \sum_{ij} \alpha_{im}\alpha_{jm} S_i^x S_j^x
\end{aligned} \tag{4.29}$$

where terms depending on inactive modes B_m and extra-cavity modes, A_k, in H_0 are neglected in the above formula as they commute with U. Moreover, the off-diagonal term coupling different active supermodes $b_m^\dagger b_n$ is removed in the form of H_0 by diagonalising the active supermodes. By taking the results in Eq.(4.28) and Eq.(4.29), the penultimate

passage gives

$$
\begin{aligned}
e^{iUH_0U^\dagger t}(b_m - \sum_i \frac{g\alpha_{im}}{\omega_c}S_i^x)e^{-iUH_0U^\dagger t} &= e^{iUH_0U^\dagger t}b_m e^{-iUH_0U^\dagger t} - e^{iUH_0U^\dagger t}\sum_i \frac{g\alpha_{im}}{\omega_c}S_i^x e^{-iUH_0U^\dagger t} \\
&= b_m + i\omega_c t\sum_{m'}[b^\dagger_{m'}b_{m'}, b_m] + \\
&+ \frac{i^2}{2}\omega_c^2 t^2 \sum_{m',m''}[b^\dagger_{m'}b_{m'}, [b^\dagger_{m''}b_{m''}, b_m]] + \ldots - \sum_i \frac{g\alpha_{im}}{\omega_c}S_i^x = \\
&= b_m e^{-i\omega_c t} - \sum_i \frac{g\alpha_{im}}{\omega_c}S_i^x
\end{aligned}
\tag{4.30}
$$

and the final step to obtain the time-dependence of the active mode consists in the outer application of the transform in Eq.(4.26):

$$
\begin{aligned}
b_m(t) =& U^\dagger(b_m e^{-i\omega_c t} - \sum_i \frac{g\alpha_{im}}{\omega_c}S_i^x)U \\
&= e^{-i\omega_c t}U^\dagger b_m U - U^\dagger \sum_i \frac{g\alpha_{im}}{\omega_c}S_i^x U \\
&= e^{-i\omega_c t}(b_m + \sum_{i,m'}\frac{g\alpha_{im'}}{\omega_c}S_i^x[b_{m'} - b^\dagger_{m'}, b_m]) - \sum_i \frac{g\alpha_{im}}{\omega_c}S_i^x = \\
&= b_m e^{-i\omega_c t} + \sum_i \frac{g\alpha_{im}}{\omega_c}S_i^x(e^{-i\omega_c t} - 1)
\end{aligned}
\tag{4.31}
$$

We now have all the elements to compute the Redfield equation. It will be sufficient to compute the integral of the first two terms of the double commutator, i.e $Tr_B\,(H_1(t)H_1(t')\rho)$

and $Tr_B\left(H_1(t)\rho H_1(t')\right)$ as the remaining terms are their hermitian conjugates.

$$\begin{aligned}
Tr_B\left(H_1(t)H_1(t')\rho_t\right) = \epsilon^2 \sum_{m,p=1}^{R}\sum_{n,q=R+1}^{N_m} \omega_{mn}\omega_{pq} Tr_B\Big[&(B_n^\dagger(t)b_m(t) + b_m^\dagger(t)B_n(t)) \\
&(B_q^\dagger(t')b_p(t') + b_p^\dagger(t')B_q(t')\rho_t)\Big] = \\
= \epsilon^2 \sum_{m,p=1}^{R}\sum_{n,q=R+1}^{N_m} \omega_{mn}\omega_{pq} Tr_B\Big[&b_m(t)B_n^\dagger(t)B_q^\dagger(t')b_p(t')\rho_t + \\
&b_m(t)B_n^\dagger(t)B_q(t')b_p^\dagger(t')\rho_t + b_m^\dagger(t)B_n(t)B_q^\dagger(t')b_p(t')\rho_t + \\
&b_m^\dagger(t)B_n(t)B_q(t')b_p^\dagger(t')\rho_t\Big] = \\
= \epsilon^2 \sum_{m,p=1}^{R}\sum_{n,q=R+1}^{N_m} \omega_{mn}\omega_{pq} \Big[&\langle B_n^\dagger(t)B_q^\dagger(t')\rangle b_m(t)b_p(t')\rho + \\
&\langle B_n^\dagger(t)B_q(t')\rangle b_m(t)b_p^\dagger(t')\rho + \langle B_n(t)B_q^\dagger(t')\rangle b_m^\dagger(t)b_p(t')\rho + \\
&\langle B_n(t)B_q(t')\rangle b_m^\dagger(t)b_p^\dagger(t')\rho\Big] = \\
\epsilon^2 \sum_{m,p=1}^{R}\sum_{n,q=R+1}^{N_m} &\omega_{mn}\omega_{pq}\langle B_n(t)B_q^\dagger(t')\rangle b_m^\dagger(t)b_p(t')\rho
\end{aligned} \tag{4.32}$$

where $\langle B_n^\dagger(t)B_q^\dagger(t')\rangle = \langle B_n^\dagger(t)B_q(t')\rangle = \langle B_n(t)B_q(t')\rangle = 0$ when calculated on the vacuum state of the bath. A similar procedure is used to get the form of the second term of the double commutator in Eq.(4.18):

$$Tr_B\left(H_1(t)\rho_t H_1(t')\right) = \epsilon^2 \sum_{m,p=1}^{R}\sum_{n,q=R+1}^{N_m} \omega_{mn}\omega_{pq}\langle B_q(t')B_n^\dagger(t)\rangle b_m(t)\rho b_p^\dagger(t') \tag{4.33}$$

We now provide the expressions of Eq.(4.32) and Eq.(4.33) integrated

$$\int_{-\infty}^{t} dt' Tr_B\left(H_1(t)H_1(t')\rho_t\right) = \epsilon^2 \sum_{m,p=1}^{R}\sum_{n,q=R+1}^{N_m} \omega_{mn}\omega_{pq}\int_{-\infty}^{t} dt' \langle B_n(t)B_q^\dagger(t')\rangle b_m^\dagger(t) b_p(t')\rho =$$
$$= \epsilon^2 \sum_{m,p=1}^{R}\sum_{n,q=R+1}^{N_m} \omega_{mn}\omega_{pq}\delta_{nq}\left[\frac{1}{\kappa}\left(b_m^\dagger b_p\rho + \sum_i \mathcal{S}_{ip} b_m^\dagger S_i^x\rho + \sum_i \mathcal{S}_{im} b_p S_i^x\rho + \right.\right.$$
$$\left.\sum_{ij}\tilde{J}_{ij}^{(mp)} S_i^x S_j^x\rho - \sum_i \mathcal{S}_{im} b_p S_i^x \rho e^{-i\omega_c t} - \sum_{ij}\tilde{J}_{ij}^{(mp)} S_i^x S_j^x \rho e^{-i\omega_c t}\right) +$$
$$\left.-\frac{1}{\kappa + i\omega_c}\left(\sum_i \mathcal{S}_{ip} b_m^\dagger S_i^x\rho e^{i\omega_c t} + \sum_{ij}\tilde{J}_{ij}^{(mp)} S_i^x S_j^x \rho e^{i\omega_c t} - \sum_{ij}\tilde{J}_{ij}^{(mp)} S_i^x S_j^x\rho\right)\right] \tag{4.34}$$

$$\int_{-\infty}^{t} dt' Tr_B\left(H_1(t)\rho_t H_1(t')\right) = \epsilon^2 \sum_{m,p=1}^{R}\sum_{n,q=R+1}^{N_m} \omega_{mn}\omega_{pq}\int_{-\infty}^{t} dt' \langle B_q(t')B_n^\dagger(t)\rangle b_m(t)\rho b_p^\dagger(t') =$$
$$= \epsilon^2 \sum_{m,p=1}^{R}\sum_{n,q=R+1}^{N_m} \omega_{mn}\omega_{pq}\delta_{nq}\left[\frac{1}{\kappa}\left(b_m\rho b_p^\dagger + \sum_i \mathcal{S}_{ip} b_m\rho S_i^x + \sum_i \mathcal{S}_{im} S_i^x\rho b_p^\dagger + \right.\right.$$
$$\left.+\sum_{ij}\tilde{J}_{ij}^{(mp)} S_i^x\rho S_j^x - \sum_i \mathcal{S}_{im} S_i^x\rho b_p^\dagger e^{i\omega_c t} - \sum_{ij}\tilde{J}_{ij}^{(mp)} S_i^x\rho S_j^x e^{i\omega_c t}\right) +$$
$$\left.-\frac{1}{\kappa - i\omega_c}\left(\sum_i \mathcal{S}_{ip} b_m\rho S_i^x e^{-i\omega_c t} + \sum_{ij}\tilde{J}_{ij}^{(mp)} S_i^x\rho S_j^x e^{-i\omega_c t} - \sum_{ij}\tilde{J}_{ij}^{(mp)} S_i^x\rho S_j^x\right)\right] \tag{4.35}$$

where $\mathcal{S}_{ip} = g\alpha_{ip}/\omega_c$ and $\tilde{J}_{ij}^{(mp)} = g^2\alpha_{im}\alpha_{jp}/\omega_c^2$.

Once the above are evaluated, the Redfield equation in the Schroedinger picture is given in the following:

$$\dot{\rho}_s = \epsilon^2 \sum_{m,p=1}^{R}\sum_{n=R+1}^{N_m} \omega_{mn}\omega_{pn}\left\{\left[\left(\frac{b_m}{\kappa} + \frac{i\sum_i g\alpha_{im}S_i^x}{\kappa(\kappa + i\omega_c)}\right)\rho_s, b_p^\dagger\right] + \text{H.c.}\right\} \tag{4.36}$$

The density matrix equation governing the dynamics of this coupled atom-active super-

mode system reads:

$$\dot{\rho}_s(t) = -i\left[\sum_{m=1}^{R}\omega_m b_m^\dagger b_m + \omega_z\sum_{i=1}^{N_E}S_i^z + g\sum_{i=1}^{N_E}\sum_{m=1}^{R}\alpha_{im}S_i^x(b_m+b_m^\dagger),\rho_s(t)\right] + \kappa\sum_{m=1}^{R}\mathcal{D}[b_m]$$
$$+\epsilon^2\sum_{m,p=1}^{R}\sum_{n=R+1}^{N_m}\omega_{mn}\omega_{pn}\left\{\left[\left(\frac{b_m}{\kappa}+\frac{i\sum_i g\alpha_{im}S_i^x}{\kappa(\kappa+i\omega_c)}\right)\rho_s, b_p^\dagger\right]+\text{H.c.}\right\}. \tag{4.37}$$

where the second line of Eq.(4.37) is the Redfield equation we have just derived and the square brackets in that line indicate a commutator. Let us indicate the prefactor on the second line of Eq.(4.37) with the notation $G^d_{mp} = \sum_{n=R+1}^{N_m}\omega_{mn}\omega_{pn}$. This prefactor and overall this Redfield term is describing the influence of the inactive supermodes on the system dynamics. The effect of the inactive modes manifests in the form of additional couplings between active supermodes, given by the prefactor G^d_{mp}, and between spins and active modes, given by $G^d_{mp}\sum_i g\alpha_{im}$. According to Eq.(4.37), the Redfield term is a combination of coherent and dissipative processes.

In the following sections, we will use Eq.(4.37) and the spin-active supermode Hamiltonian Eq.(4.15) to write a cumulant expansion up to second order in the expectation values of both spin and field operators.

4.3 Mean field equations

In this section, we provide the form of the mean field equations of motion for the expectation value of the spin ensembles $\langle S_i^\alpha\rangle$ and active supermodes $\langle b_m\rangle$ derived from Eq.(4.37). Given the expression of the dynamics of a state ρ:

$$\dot{\rho} = -i[H,\rho] + \sum_i\left(\alpha_i[A_i\rho, B_i^\dagger] + \text{H.c.}\right), \tag{4.38}$$

the equation of motion of the expectation value of a generic operator X is:

$$\begin{aligned}\langle \dot{X} \rangle &= \mathrm{Tr}\left(X\dot{\rho}\right) \\ &= \mathrm{Tr}\Big(-iX[H,\rho] + \sum_i \left(\alpha_i X[A_i\rho, B_i^\dagger] + \alpha_i^* X[B_i, \rho A_i^\dagger]\right)\Big) \\ &= \mathrm{Tr}\Big(i[H,X]\rho + \sum_i \left(\alpha_i [B_i^\dagger, X]A_i + \alpha_i^* A_i^\dagger [X, B_i]\right)\rho\Big) \\ &= i\langle [H,X]\rangle + \sum_i \left(\alpha_i \langle [B_i^\dagger, X]A_i\rangle + \alpha_i^* \langle A_i^\dagger [X, B_i]\rangle\right),\end{aligned} \tag{4.39}$$

where in the third line we perform cyclic permutations under the trace. This can be our reference point when computing the equation of any single operator or product of operators, as the above equation is formally exact. Mean field equations are obtained by first solving the above commutators with the generic operator chosen and then reducing correlations to products of single-operator expectation values, i.e. $\langle AB\rangle = \langle A\rangle\langle B\rangle$.

Considering that Eq.(4.37) is written in the form of Eq.(4.38), after proper identification of the operators A_i and B_i, we can use the above equation for $\langle \dot{X}\rangle$ in combination with the mean field ansatz to obtain a closed set of equations for the spin and supermode expectation values:

$$\begin{aligned}\langle \dot{b_m} \rangle &= -(i\omega_m + \kappa)\langle b_m\rangle - ig\sum_{i=1}^{N_E} \alpha_{im}\langle S_i^x\rangle - \epsilon^2 \sum_{n=1}^{R} G_{mn}^d \left(\frac{\langle b_n\rangle}{\kappa} + \frac{ig\sum_{i=1}^{N_E}\alpha_{in}\langle S_i^x\rangle}{\kappa(i\omega_c+\kappa)}\right) \\ \langle \dot{S_i^x} \rangle &= -\omega_z \langle S_i^y\rangle \\ \langle \dot{S_i^y} \rangle &= \omega_z\langle S_i^x\rangle - g\langle S_i^z\rangle \sum_{m=1}^{R} \alpha_{im}\left(\langle b_m\rangle + \langle b_m\rangle^*\right) \\ \langle \dot{S_i^z} \rangle &= g\langle S_i^y\rangle \sum_{m=1}^{R} \alpha_{im}\left(\langle b_m\rangle + \langle b_m\rangle^*\right).\end{aligned} \tag{4.40}$$

To study the evolution of these variables, we initialise the system slightly away from the normal phase $\langle S_i^z\rangle = -M/2$, $\langle S_i^{x,y}\rangle = \langle b_m\rangle = 0$ by adding a small randomly distributed perturbation, as the normal state is a stable configuration for the system. It is worth reminding that we consider a total number N of spins divided in N_E spin ensembles located at random positions within the cavity (each ensemble is a collective spin of length $S = M/2$) coupled to R active supermodes, with $N_E = R$. We observe the evolution of

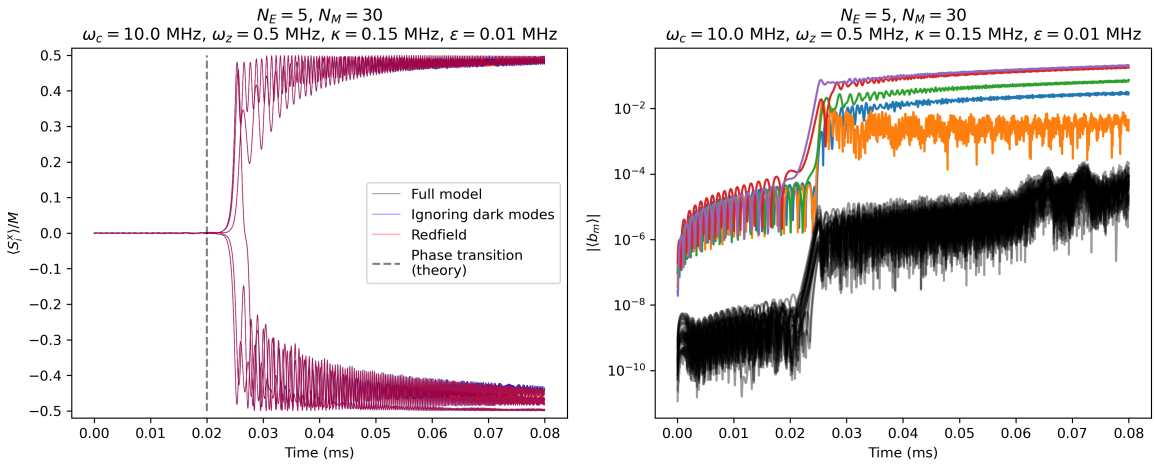

Fig. 4.1. (Left) Evolution of S_i^x over time evaluated from the full model in the original cavity basis (grey), with (red) and without (blue) inactive modes. (Right) The absolute value of the expectation of supermodes showing both inactive (black) and active (colored) mode solutions. There is a net difference in magnitude between active and inactive modes across the entire region, providing a picture where the inactive modes seem to have a weaker influence on the system. The data used to generate these figures have been obtained with permission from B.P. Marsh as part of the collaboration.

this system by increasing linearly the coupling strength with time according to the formula $g(t) = At$. Specifically, this is how we set the problem up: $4Mg_c^2 = \omega_z(\omega_c^2 + \kappa^2)/\omega_c$ gives the location of the critical point, $g(t) = \text{off}g_c + g_c rt$ so that $t_c = (1 - \text{off})/r$, where off $= 0.5$ is an offset and r is the rate we used to ramp the laser beam to threshold. Such settings will be also applied when evaluating the equations for the second order moments of the variables.

To establish to what extent the inactive supermodes shape the system dynamics, we could compare the solution obtained from: (1) the mean field theory of the full model in the original basis, (2) the problem with the Redfield term due to the inactive modes, and (3) a model where we ignore the inactive modes and care about spins and active modes only. The latter configuration corresponds to setting G_{mn}^d in the above equations to 0. This comparison is shown in Fig.(4.1) and Fig.(4.2). The cavity frequencies obey the linear dispersion $\omega_m = \omega_c + m\epsilon$ where $m = 1, \cdots, N_m$ and N_m is finite as given in Fig.(4.1), the cavity loss rate κ is kept constant, and the spin-cavity couplings η_{im} are obtained from a Gaussian distribution with unit variance. In the left panel of Fig.(4.1), the evolution of $\langle S_i^x \rangle$ rescaled for the number of atoms per clump is shown. Just after the critical point, some

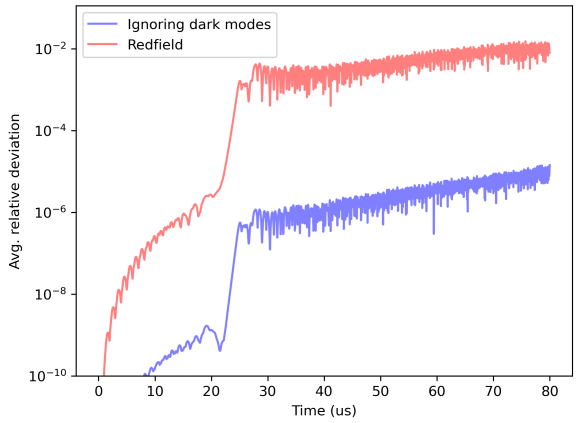

Fig. 4.2. Relative deviation of the solutions from the full model. Ignoring the inactive modes (blue) yields a solution closer to that of the full problem. The data used to generate these figures have been obtained with permission from B.P. Marsh as part of the collaboration.

of the spins acquire a polarization along the positive direction and adjust themselves in an oscillating manner to converge to 0.5, while the remaining do the same but selecting the opposite value -0.5. As shown in that panel in Fig.(4.1), for the choice of parameters we used, these $\langle S_i^x \rangle$ solutions obtained from the three models are in good agreement. When looking at the behaviour of the field $|\langle b_m \rangle|$, we observe a discontinuity as the coupling strength hits the critical value. We also see the amplitude of the active modes is orders of magnitude larger that that of the inactive modes. From this configuration, it appears that the inactive modes would not be really relevant for the system dynamics. This is also reflected by Fig.(4.2) where the deviation of the solutions (with and without the Redfield term) from that predicted by the full model is shown. Surprisingly, ignoring the inactive modes predicts a behavior closer to the full solution than when including them through the Redfield term in Eq.(4.37). We have varied parameters such as number of ensembles N_E, cavity loss rate κ and degree of dispersion ϵ and, in all cases, the model without the Redfield term ($G^d_{mn} = 0$ in Eq.(4.37)) due to the inactive supermodes performs better than when we include such a term.

Therefore, we will neglect the Redfield contribution when writing equations of motion for the second order moments of spins and active supermodes in the next section.

4.4 Cumulant equations

While the mean field approximation is strictly valid when the number of particles tends to infinity, realistic experimental configurations necessarily deal with finite numbers of particles. These can range from few atoms to several thousands; therefore, a more accurate method to describe finite-size effects is a cumulant expansion. As discussed in chapter 2, taking into account correlation functions of the system at all orders produce an infinite set of coupled equations. It is therefore necessary to operate a truncation of the expansion to close the hierarchy. As we have seen in chapter 3, the probability distribution of the steady state of 4KRE had a quasi-Gaussian profile which justified a truncation at the second order in the expansion. There, since the steady state was symmetric and diagonal in S^z, the probability was accurately identified by the first two moments of the S^z operator.
In the present case, with a system composed by atoms coupled to fields, making this evaluation is more difficult. We, however, start by computing equations for the second order correlations, which represent the next leading order in the expansion, to analyse the $1/M$ corrections to the mean field results. The first step is simply taking Eq.(4.39) and substituting to X the string of operators, variables of our linear system. We simplify any commutation relation appearing on the right hand side of Eq.(4.39) and get to a form with second and third order moments for the spin and supermode operators. It is also worth remembering that we should keep in mind the non-commuting nature of some operators.
Having said that, we need to identify a method to decouple 3-operator expectations including non-commuting operators, terms such as $\langle b_m S_i^\alpha S_i^\beta \rangle$. In the intermediate form of the equations, just before using a decoupling rule, we encountered third order correlations of that type in our derivation. We thus adopt the following rule:

$$\langle b_m S_i^\alpha S_i^\beta \rangle = \frac{1}{2}\left\langle b_m \left\{ S_i^\alpha, S_i^\beta \right\} \right\rangle + \frac{1}{2}\left\langle b_m \left[S_i^\alpha, S_i^\beta \right] \right\rangle = \frac{1}{2}\left\langle b_m \left\{ S_i^\alpha, S_i^\beta \right\} \right\rangle + \frac{i}{2}\varepsilon^{\alpha\beta\gamma}\left\langle b_m S_i^\gamma \right\rangle \tag{4.41}$$

with the anticommutator term to be decoupled according to the classical rule [131]. The reason why we factorise the anticommutator with the standard rule is because, given that $\langle X\rangle\langle Y\rangle = \langle Y\rangle\langle X\rangle$ and $\frac{1}{2}\langle\{X,Y\}\rangle = \frac{1}{2}\langle\{Y,X\}\rangle$, the anticommutator term behaves as a classical variable where decoupling does not break anything about operator ordering.
Only the equations for $\langle b_m S_i^y \rangle$, $\langle S_i^y S_i^y \rangle$, $\langle S_i^z S_i^z \rangle$ and $\langle S_i^x S_i^y \rangle$ presented 3-operator expecta-

tions to be decoupled according to Eq.(4.41). We provide these equations in the following:

$$\begin{aligned}\frac{d}{dt}\langle b_m S_i^y\rangle =& -(i\omega_m+\kappa)\langle b_m S_i^y\rangle + \omega_z\langle b_m S_i^x\rangle - g\sum_{m'=1}^{R}\alpha_{im'}\langle S_i^z\rangle\langle b_m b_{m'}\rangle \\ & - ig\sum_{j=1}^{N_E}\alpha_{jm}\langle S_j^x S_i^y\rangle - g\sum_{m'\neq m}^{R}\alpha_{im'}\langle S_i^z\rangle\langle b_m b_{m'}^\dagger\rangle - g\alpha_{im}\left(\langle S_i^z\rangle\langle b_m^\dagger b_m\rangle + \langle S_i^z\rangle\right)\end{aligned} \tag{4.42}$$

$$\frac{d}{dt}\langle S_i^y S_i^y\rangle = \omega_z\left(2\langle S_i^x S_i^y\rangle - i\langle S_i^z\rangle\right) - g\sum_{m=1}^{R}\alpha_{im}\left(2\langle S_i^z\rangle\langle b_m S_i^y\rangle + 2\langle S_i^z\rangle\langle b_m^\dagger S_i^y\rangle\right) \tag{4.43}$$

$$\frac{d}{dt}\langle S_i^z S_i^z\rangle = g\sum_{m=1}^{R}\alpha_{im}\left(2\langle S_i^z\rangle\langle b_m S_i^y\rangle + 2\langle S_i^z\rangle\langle b_m^\dagger S_i^y\rangle\right) \tag{4.44}$$

$$\begin{aligned}\frac{d}{dt}\langle S_i^x S_i^y\rangle =& \omega_z\left(\langle S_i^x S_i^x\rangle - \langle S_i^y S_i^y\rangle\right) \\ & - g\sum_{m=1}^{R}\alpha_{im}\left(\langle S_i^z\rangle\langle b_m S_i^x\rangle - \frac{i}{2}\langle b_m S_i^y\rangle + \langle S_i^z\rangle\langle b_m^\dagger S_i^x\rangle - \frac{i}{2}\langle b_m^\dagger S_i^y\rangle\right)\end{aligned} \tag{4.45}$$

In Eq.(4.42), in a previous passage, we exploit the commutators $[b_m, b_m^\dagger] = 1$ (line 2 of the equation). The final form of the above equations is finally achieved by keeping the $\mathbb{Z}_2$-symmetric variables only, after the decoupling procedure, as those are sufficient to see critical behavior in finite size systems.

The complete set of equations for the $\mathbb{Z}_2$-symmetric correlation functions is thus found:

$$
\begin{aligned}
\frac{d}{dt}\langle b_m^\dagger b_n\rangle &= (i\omega_m - i\omega_n - 2\kappa)\langle b_m^\dagger b_n\rangle + ig\sum_{i=1}^{N_E}(\alpha_{im}\langle b_n S_i^x\rangle - \alpha_{in}\langle b_m^\dagger S_i^x\rangle)\\
\frac{d}{dt}\langle b_m b_n\rangle &= -(i\omega_m + i\omega_n + 2\kappa)\langle b_m b_n\rangle - ig\sum_{i=1}^{N_E}(\alpha_{im}\langle b_n S_i^x\rangle + \alpha_{in}\langle b_m S_i^x\rangle)\\
\frac{d}{dt}\langle b_m S_i^x\rangle &= -(i\omega_m + \kappa)\langle b_m S_i^x\rangle - \omega_z\langle b_m S_i^y\rangle - ig\sum_{j=1}^{N_E}\alpha_{jm}\langle S_i^x S_j^x\rangle\\
\frac{d}{dt}\langle b_m S_i^y\rangle &= -(i\omega_m + \kappa)\langle b_m S_i^y\rangle + \omega_z\langle b_m S_i^x\rangle - g\sum_{m'=1}^{R}\alpha_{im'}\langle S_i^z\rangle\langle b_m b_{m'}\rangle - ig\sum_{j=1}^{N_E}\alpha_{jm}\langle S_j^x S_i^y\rangle\\
&\quad - g\sum_{m'\neq m}^{R}\alpha_{im'}\langle S_i^z\rangle\langle b_m b_{m'}^\dagger\rangle - g\alpha_{im}\left(\langle S_i^z\rangle\langle b_m^\dagger b_m\rangle + \langle S_i^z\rangle\right)\\
\frac{d}{dt}\langle S_i^z\rangle &= g\sum_{m=1}^{R}\alpha_{im}\left(\langle b_m S_i^y\rangle + \langle b_m^\dagger S_i^y\rangle\right)\\
\frac{d}{dt}\langle S_i^x S_j^x\rangle &= -\omega_z\langle\left\{S_i^x, S_j^y\right\}\rangle\\
\frac{d}{dt}\langle S_i^y S_j^y\rangle &= \omega_z\langle\left\{S_i^x, S_j^y\right\}\rangle - g\sum_{m=1}^{R}\left(\alpha_{im}\langle S_i^z\rangle\langle b_m S_j^y\rangle + \alpha_{jm}\langle S_j^z\rangle\langle b_m S_i^y\rangle + \text{h.c.}\right)\\
\frac{d}{dt}\langle S_i^z S_j^z\rangle &= g\sum_{m=1}^{R}\left(\alpha_{jm}\langle S_i^z\rangle\langle b_m S_j^y\rangle + \alpha_{im}\langle S_j^z\rangle\langle b_m S_i^y\rangle + \text{h.c.}\right)\\
\frac{d}{dt}\langle S_i^x S_i^y\rangle &= \omega_z\left(\langle S_i^x S_i^x\rangle - \langle S_i^y S_i^y\rangle\right) - g\sum_{m=1}^{R}\alpha_{im}\left(\langle S_i^z\rangle\langle b_m S_i^x\rangle - \frac{i}{2}\langle b_m S_i^y\rangle + \langle S_i^z\rangle\langle b_m^\dagger S_i^x\rangle - \frac{i}{2}\langle b_m^\dagger S_i^y\rangle\right)\\
\frac{d}{dt}\langle S_i^x S_j^y\rangle &= \omega_z\left(\langle S_i^x S_j^x\rangle - \langle S_i^y S_j^y\rangle\right) - g\sum_{m=1}^{R}\alpha_{jm}\left(\langle S_j^z\rangle\langle b_m S_i^x\rangle + \langle S_j^z\rangle\langle b_m^\dagger S_i^x\rangle\right)\\
\frac{d}{dt}\langle S_i^y S_i^x\rangle &= \omega_z\left(\langle S_i^x S_i^x\rangle - \langle S_i^y S_i^y\rangle\right) - g\sum_{m=1}^{R}\alpha_{im}\left(\langle S_i^z\rangle\langle b_m S_i^x\rangle + \frac{i}{2}\langle b_m S_i^y\rangle + \langle S_i^z\rangle\langle b_m^\dagger S_i^x\rangle + \frac{i}{2}\langle b_m^\dagger S_i^y\rangle\right)\\
\frac{d}{dt}\langle S_i^y S_j^x\rangle &= \omega_z\left(\langle S_i^x S_j^x\rangle - \langle S_i^y S_j^y\rangle\right) - g\sum_{m=1}^{R}\alpha_{im}\left(\langle S_i^z\rangle\langle b_m S_j^x\rangle + \langle S_i^z\rangle\langle b_m^\dagger S_j^x\rangle\right)
\end{aligned}
\tag{4.46}
$$

We note that the length of the collective spin in each ensemble is a constant of motion. In fact, by taking the equations for $\langle S_i^x S_i^x \rangle$, $\langle S_i^y S_i^y \rangle$, and$\langle S_i^z S_i^z \rangle$, we find the following condition: $\frac{d}{dt}\left(\langle S_i^x S_i^x \rangle + \langle S_i^y S_i^y \rangle + \langle S_i^z S_i^z \rangle\right) = 0$. Moreover, we note that the canonical commutation relation of spin components is satisfied, namely from the equations for $\langle S_i^x S_i^y \rangle$and$\langle S_i^y S_i^x \rangle$, we find $\frac{d}{dt}\langle [S_i^x, S_i^y] \rangle = i\frac{d}{dt}\langle S_i^z \rangle$. As a final observation, one might reduce the number of equations by removing the EOM for $\langle S_i^z S_j^z \rangle$ (including $i = j$) as those are decoupled from the other equations.

In contrast to the mean field scenario discussed before, here, the system can be exactly initialised in the normal state, without having to perturb it. Some plots are shown in Fig.(4.3) for the evolution of $\langle S_i^z \rangle$ and in Fig.(4.4) and Fig.(4.5) for the evolution of $\langle S_1^x S_j^x \rangle$ for 15 spin ensembles coupled to an equal number of supermodes. Those sets of figures show a discontinuity in correspondence of the predicted coupling threshold (here expressed as a function of time, as a reminder: $4Mg_c^2 = \omega_z(\omega_c^2 + \kappa^2)/\omega_c$, $g(t) = x_{\text{off}} g_c + g_c r t$ so that $t_c = (1 - x_{\text{off}})/r$, where $x_{\text{off}} = 0.5$ is an offset and r is the rate we used to ramp the spin system to threshold). As expected, the discontinuity becomes sharper with the number of atoms per ensemble, here represented by M in the figures, see for example Fig.(4.3). Moreover, for a fixed value of ramp rate, we see that the system develops oscillations of increasing amplitude in both types of solutions as we raise the number of atoms per ensemble. Collective phenomena become more visible in a physical system as one approaches the thermodynamic limit. In this case, the oscillations that the system develops throughout the dynamics are the reflection of the collective behavior which becomes more pronounced as M is raised. The oscillations observed are also influenced by the rate used to pump the system to the critical point, with variations in the solutions becoming more evident for higher ramp rates, as shown in the comparison between Fig.(4.4) and Fig.(4.5). Given a certain parameter configuration, each experimental run can yield a different outcome in terms of how many spin ensembles are measured on the state $|\uparrow\rangle_x$ or $|\downarrow\rangle_x$. This is thus reflected by how likely a given pattern of states $|\uparrow\rangle_x$ and $|\downarrow\rangle_x$ is in the single measurement process.

In order to compare theory to experiments, it would therefore be useful to find a way to predict the probability of the different spin alignment configurations. A first approximation of how this could be done is to ignore any constraints on the form of the spin vector, and regard S^x as free variables, constrained only by the covariance matrix $\langle S_i^x S_j^x \rangle$ we find in the time-evolved cumulant equations. Our aim is thus to realise random experiments

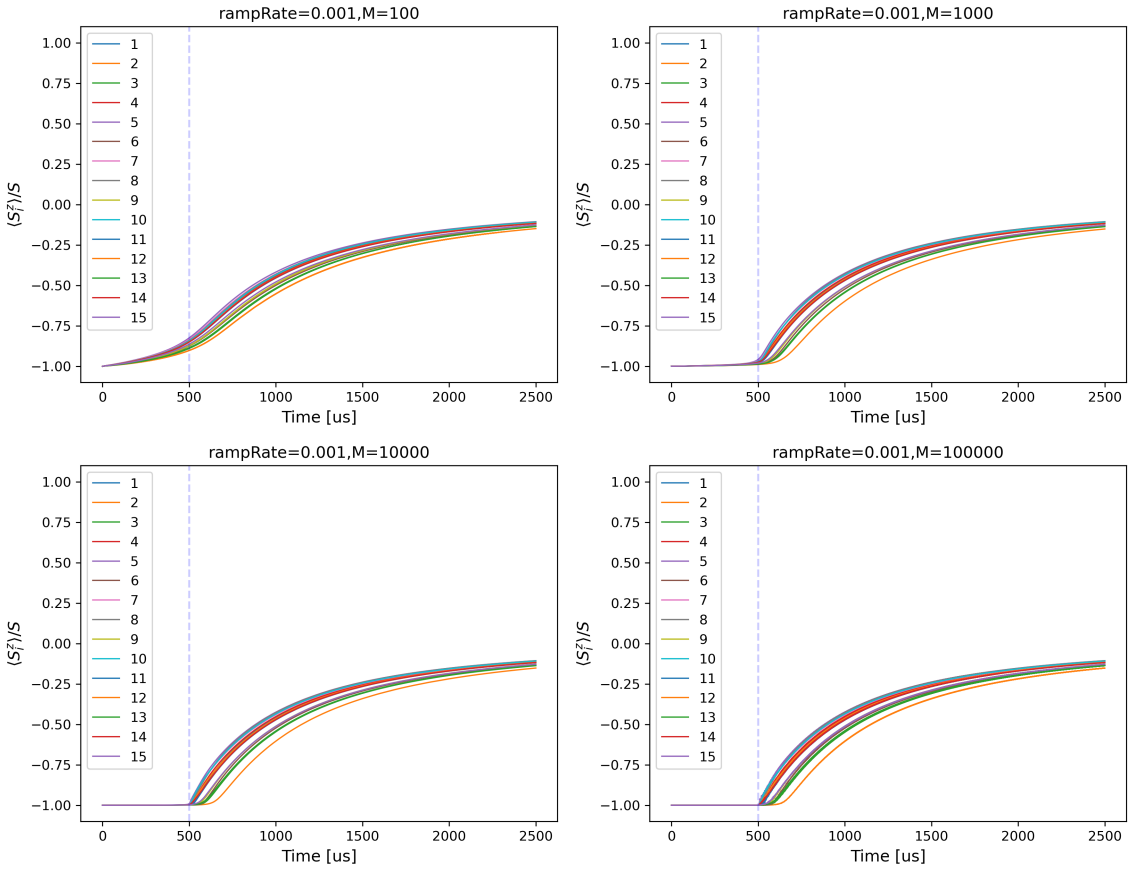

Fig. 4.3. Time evolution of the rescaled expectation of S_i^z for $N_E = 15$ ensembles driven to threshold (indicated by the vertical dashed line) at a rate $0.001\mu s^{-1}$. Each panel shows the behavior with a different number of atoms per ensemble M ($S = M/2$). Parameters of the system: $\omega_c = 5$ MHz, mode dispersion $\epsilon = 0.1$ MHz, $\kappa = 0.2$ MHz, $\omega_z = 0.5$ MHz

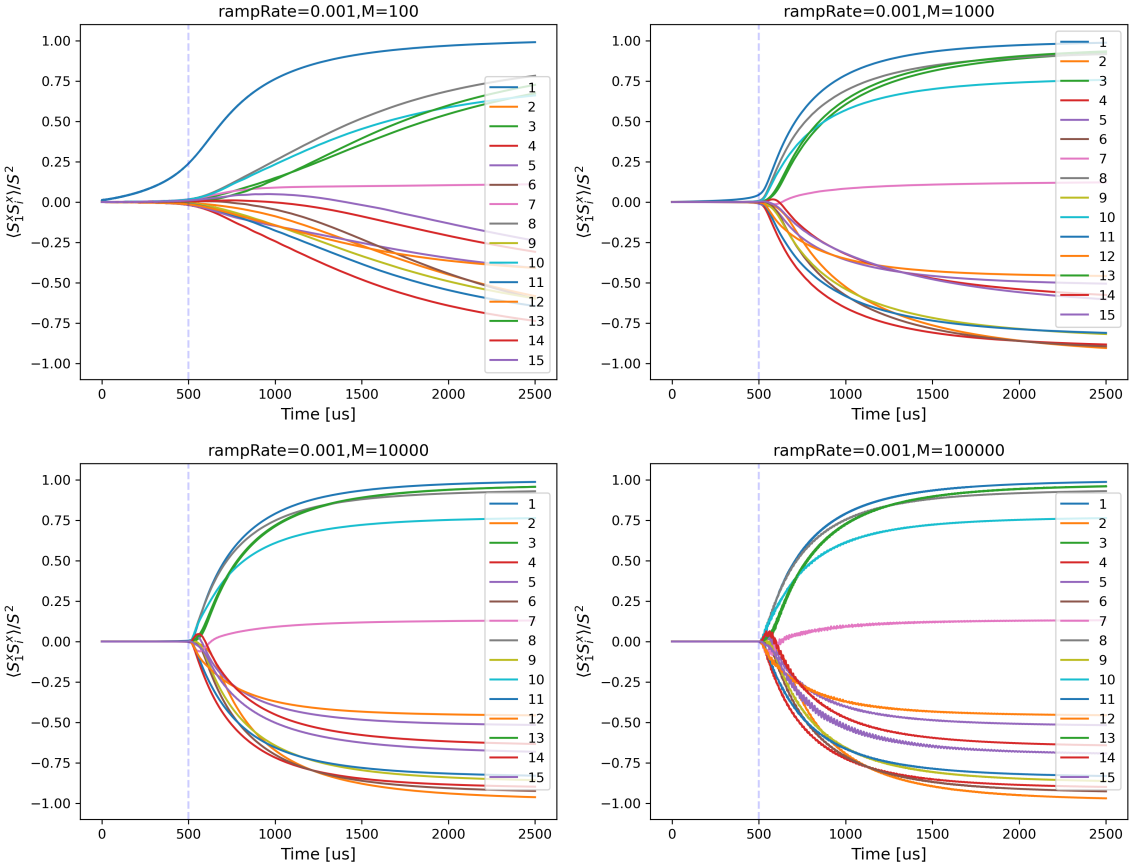

Fig. 4.4. Similar plots to Fig.(4.3) but for $\langle S_1^x S_j^x \rangle$ evaluated at a ramp rate of $0.001 \mu s^{-1}$.

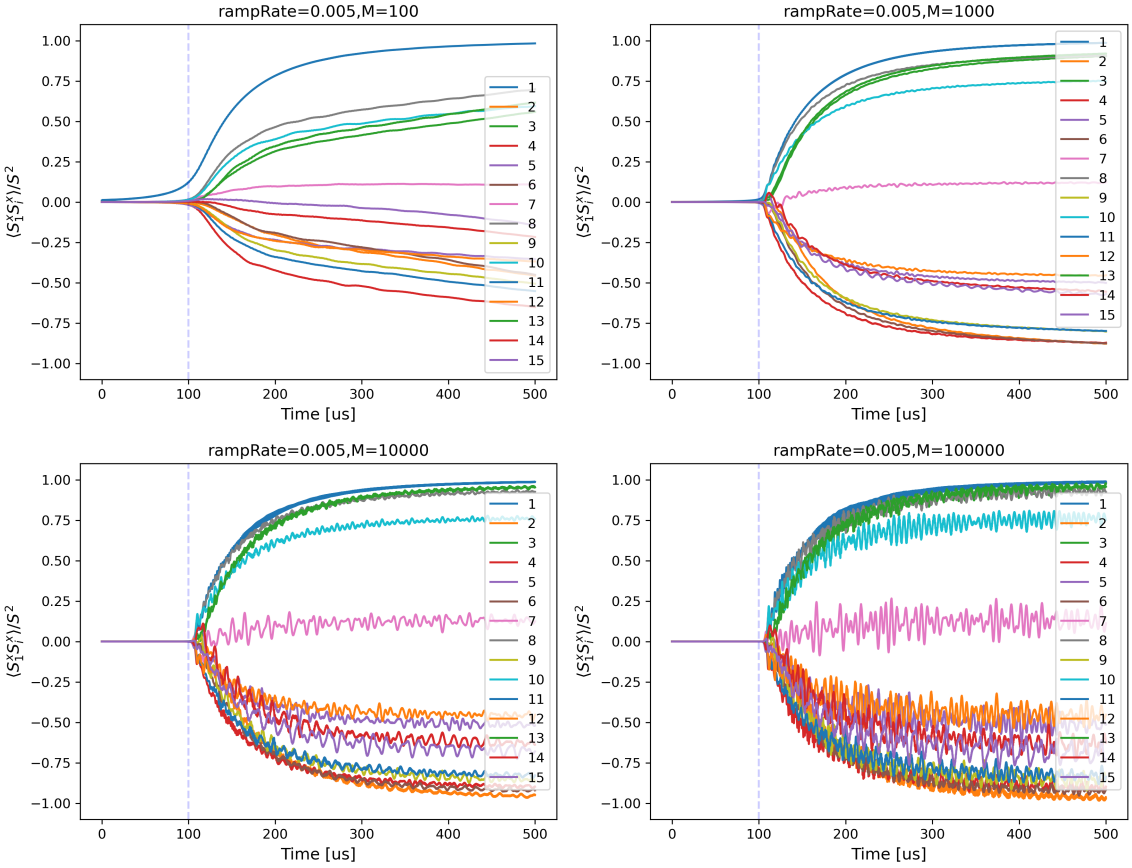

Fig. 4.5. Similar plots to Fig.(4.3) but for $\langle S_1^x S_j^x \rangle$ evaluated at a ramp rate of $0.005 \mu s^{-1}$.

that sample from the covariance matrix. We do this by constructing random variables $X' = \sqrt{S}X$, where X, corresponding to $\langle S_i^x \rangle$ ($i = 1, ..., N_E$), is drawn from a Gaussian distribution of unit variance and S is the covariance matrix of the correlations between spin ensembles evaluated at the final time, when the system reaches the stationary state. This operation has the effect that X' is a random variable, but its correlations relate to the covariance matrix. Since we are interested in the sign of the magnetisation acquired by the spins in the superradiant phase, we select the signs of the elements of the vector X', thus obtaining a vector of $+1$ and -1 entries. A vector with a given number of $+1$ and -1 entries is stored as a pattern, a measurement outcome in the experiment. The above procedure, corresponding to an actual measurement process in the experiment, is then repeated a large number of times ($N_{\text{samples}} \approx 10^5$) where, in each run, we collect all patterns corresponding to unique configurations, and we count how many times a given pattern is found. Thus, the probability of occurrence of a certain spin-alignment configuration is given by $P = \text{n}/N_{\text{samples}}$, where n is the number of times we find a specific pattern. As noted at the start, the Dicke model can be mapped to an Ising model. Therefore, our ultimate goal is to use the multimode cavity to solve a random Ising model and explore how well the spin patterns found in fact minimise this Ising model. In such a picture, one could thus see a relation between the steady state attractor in the cumulant dynamics and the ground state configuration of the underlying Ising model. In this way, one could compute the energies of all patterns stored as unique states, s_i ($i = 1, ..., N_E$), with the formula $E = -\frac{1}{2}\sum_{ij} J_{ij} s_i s_j$.

One thus has a set of probabilities of occurrences accompanied by a set of Ising energies associated with each single pattern of spin alignments. By recalling that all of this derives from the spin correlations $\langle S_i^x S_j^x \rangle$, solutions of the cumulant equations Eqs.(4.46), the question we might ask is: with the cumulant approach we adopted here, what is the probability for the cumulants to predict the ground state of the associated Ising model? The results are reported in Fig.(4.6). We considered a range of number of spins per ensemble ($N_E = 15$ ensembles) $M \in [100, 10^5]$ and four values for the laser's ramping up rate through threshold. Fig.(4.6) shows the sampling probability, resulting from the procedure described above, as a function of the Ising energy calculated by means of the unique states (patterns) collected during the procedure. The points in the graphs corresponding to the four ensemble sizes M are roughly organised in clusters with a certain separation in energy, starting from the ground state energy (black dashed line). If we focus on the

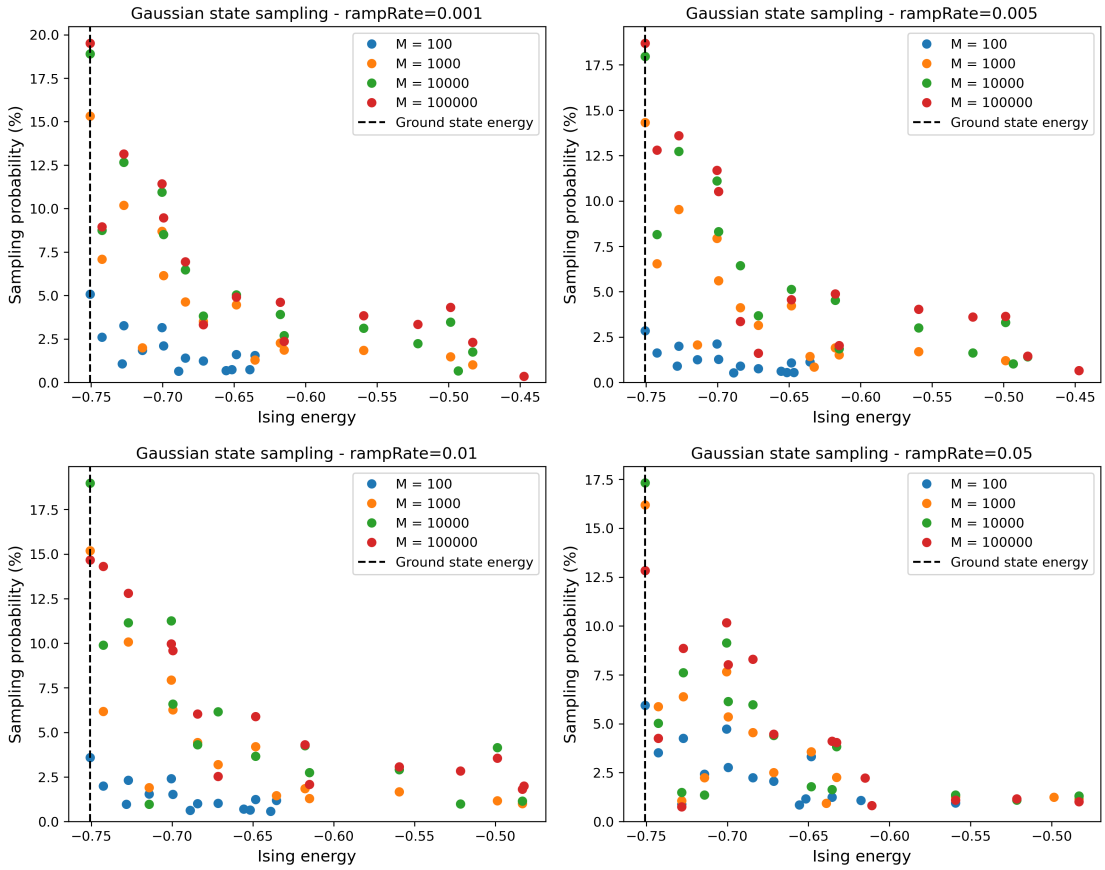

Fig. 4.6. Sampling probability as a function of the Ising energy for a range of M and ramp rates $[\mu s^{-1}]$. Parameters are as in Fig.(4.3).

vertical dashed line only in Fig.(4.6), we see that the sampling procedure based on the cumulant solutions predicts that the ground state configuration can be found in all M cases and ramp rates considered here. Moreover, it appears that as one increases the number of atoms per ensemble M, the probability of finding the ground state by the cumulants increases accordingly, when the system is ramped through threshold slowly, with a ramp rate of $0.001\mu s^{-1}$, the smallest rate considered here, as shown in Fig.(4.6). By keeping on focusing on the black dashed line, if we follow a single point M across the four plots, we see that for $M = 100$ atoms per ensemble (blue point), the probability is the lowest, staying at values in the range $(6\% - 2.5\%)$. The probability raises for $M = 1000$ (yellow) and $M = 10^4$ (green) atoms per ensemble, staying roughly constant at 15% and 17.5% as one increases the rate. In the case $M = 10^5$ (red), the probability declines from approximately 20% to roughly 13% when the system is ramped up faster (here $0.05\mu s^{-1}$).

To conclude, these preliminary results show that the cumulant method applied in this section predicts the ground state configuration of this spin model in a multimode cavity in a range of system sizes M. In the case considered here, the highest probabilities are found for higher number of atoms per ensemble M driven to threshold sufficiently slow. Further analysis has to be performed to search for the parameter configuration that optimises the probability. This can be done by analysing the dependence of the probability on the number of ensembles N_E, the position arrangement in the cavity and the number of spins per ensemble. An important question for future work is (1) to compare these predictions to other exact numerics, and thus (2) verify whether the approximation above is valid.

Chapter 5

Conclusions and outlook

In the present research thesis, I have worked on methods for the derivation of effective reduced theories in multimode cavity-QED models.

The thesis begins with an overview on the experimental realisations of the Dicke model by means of laser-driven atoms coupled to the electromagnetic field in an optical cavity. These realisations can involve Bose-Einstein condensates, thermal atomic gases, or even degenerate Fermi gases. In both types of setups, the coupled atom-field system undergoes a $\mathbb{Z}_2$ symmetry breaking phase transition from a configuration where atoms scatter photons incoherently as independent entities to a configuration where atoms cooperate to enhance this process. This behavior is known as superradiant phase transition. As atoms are exposed to a laser field of increasing intensity, at the critical value of the atom-cavity coupling strength, they will adopt one of two mutually exclusive configurations thus breaking the $\mathbb{Z}_2$ symmetry of the model.

While atoms interacting with a single electromagnetic mode of the cavity realise the standard $\mathbb{Z}_2$ Dicke model, such a physical configuration does not allow for a model with continuous symmetry breaking. To reach this goal, one has to model the coupling with more than a single cavity field. It is in fact possible to engineer effective Dicke models with U(1) symmetry where atoms interact with two or more photonic modes in a cavity. These driven-dissipative systems undergoing continuous symmetry breaking are expected to show low-energy excitations, known as Goldstone modes. Moreover, in order to be able to trace the presence of symmetry breaking effects, as the emergence of a Goldstone mode, in dissipative systems, one has to resort to the spectral theory of Liouvillian

superoperators. In fact, the occurrence of symmetry breaking is normally signalled by a vanishing eigenvalue in the symmetry broken sector of the Liouvillian.

However, theoretically solving many-body models, such as those describing the interaction of several thousands of atoms with multiple light modes, poses a concrete analytical and numerical challenge. Therefore, any chance to resort to an equivalent theory but in terms of fewer degrees of freedom is significantly helpful. As driven-dissipative systems rely on the concept of energy exchange with external environment, they are generally described within an open quantum systems formalism, based on the time evolution of the density matrix operator. In these cases, a widely used method to represent the dynamics of a reduced system, where some degrees of freedom are retained and others are traced out, is Redfield theory.

Taking the above background as a reference, the first research chapter (chapter 3) aimed at developing a Redfield atom-only theory for a class of two-mode Dicke models with U(1) symmetry. Surprisingly, this method fails to describe a superradiance phase transition, as the resulting equation predicts a steady state independent of the coupling strength, while the full atom-cavity problem predicts a change of state with the coupling strength. This issue is solved once a fourth order contribution is included in this atom-only theory. The approach used to derive the fourth order dissipator relies on a time-dependent perturbation theory based on irreducible Keldysh diagrams. When solved, this fourth order Keldysh-Redfield equation 4KRE converges to the expected steady states and recovers the mean field prediction of the full two-mode problem across the relevant region of atom-light coupling strength.

However, when the symmetry-broken sector of the underlying Liouvillian is diagonalised, 4KRE lacks the expected vanishing eigenvalue in the superradiant phase, signature of the U(1) symmetry breaking.

From the findings discussed in the chapter, several aspects might be explored for future work. Firstly, as we have seen in the case of standard second order Redfield theory, adding the next leading order proved to be essential for observing the expected steady states. This confirms that the fourth is the minimal order needed to observe a transition in these two-mode models. On the same line, one could thus try including the next leading order in the expansion (the sixth) to see if that could be considered as the minimal order needed to observe a gap closure, or at least, to be used for a more accurate extrapolated estimate at the thermodynamic limit.

It is worth noting that second order Redfield theory is sufficient when applied on the $\mathbb{Z}_2$ Dicke model, meaning that it recovers both steady states and a zero eigenvalue (Liouvillian gap), in the symmetry-broken region. Surprisingly, including a fourth order term obtained with the Keldysh diagrammatic technique still predicts the steady state but causes the Liouvillian gap to become open [137]. From these observations on the comparison U(1) versus $\mathbb{Z}_2$ model, it seems that this diagrammatic approach is a working tool when one examines the symmetric sector of the dynamics, the steady states and the eigenmodes determining the relaxation of the system towards those long-time solutions. In contrast, it fails on anything regarding the symmetry-broken sector of the dynamics. Further research on this aspect is needed in order to understand whether there are alternative approaches that give an effective theory that recovers the zero mode.

Reflecting on the nature of the symmetry, in the attempt of unveiling the reasons why the standard Redfield theory works on a model with discrete symmetry and fails on another with continuous symmetry, it might be worth to identifying other light-matter models with continuous symmetry and test whether a similar issue arises when deriving a reduced theory.

The last research chapter (chapter 4) focuses on the multimode Dicke model which, in principle, accounts for couplings between atoms and an infinite number of cavity modes. Therefore, on the same line of the research discussed in chapter 3, the strategy here is to resort to an equivalent but reduced picture of the system under study.

While in the previous research problem we were looking at the dynamics of a single collective spin coupled to the cavity, in this case, we are interested in the behavior of multiple spin ensembles coupled to the electromagnetic field in the cavity. As a consequence, each ensemble is supposed to interact more with a given set of modes and less with another, depending on the relative spatial overlap. This assumption leads to the reformulation of the problem in terms of spins interacting with superpositions of cavity modes, or supermodes. This reformulation has the advantage of still yielding the standard interaction form between atoms and the new basis of cavity modes, but accounting for a reduced number of fields. In particular, this picture can be further simplified by observing that some supermodes are strongly coupled to the spins and others weakly. One can thus provide a Redfield theory where the weakly interacting supermodes are traced out.

In order for this reduced atom-supermode theory to predict results resembling the measurement outcomes in the experiment in the most accurate way possible, one has to write

a set of dynamical equations accounting for effects due to the finite size of the physical system. While the mean field approximation is accurate in catching physical features when the number of particles tends to infinity, the formalism based on cumulant equations of motion is used to describe dynamics of systems with a finite number of particles, relevant for comparisons with experimental results. In the present case, one could exploit solutions of a second order cumulant expansion to construct a procedure to sample the probability of occurrence of a given measurement outcome. This is useful to understand how accurate the adopted cumulant approach is in finding the lowest energy configuration of the system, given some initial constraints.

To see whether the sampling procedure discussed can be further optimised, one could explore other parameter configurations. In particular, asking what is the optimal number M of atoms per ensemble, given a J_{ij} matrix defined by a given number of spin ensembles, that maximise the probability of finding the lowest-energy state of the model.

The truncation at second order in the cumulant expansion relies on the assumption that the steady state density matrix of this bipartite spin-supermode system is Gaussian, as also assumed in chapter 3 for the U(1)-symmetric atom-only system. Moreover, while in the U(1) symmetry problem, we deal with a restricted subspace of the total Hilbert space, the atomic sector, we found that the truncation at second order is actually supported by the Gaussian nature of the steady state density matrix. In a general light-matter model, like the spin-supermode system, even if the reformulation cares about a restricted subspace of the total Hilbert space, there is no net separation between the atomic and field sector. One should thus analyse the form of the distribution of the states and truncate the hierarchy of the equations at the order approximating best the steady state probability distribution.

Acknowledgements

This thesis is the result of four years of scientific research, stemming from an articulated path, alternating moments of solitary reflection and other of strong collaborative efforts. As the most significant memories are related to the latter aspect, I would like to thank here all the people that were involved in this path. I wish to begin by thanking my supervisor Dr. Jonathan Keeling for being a constant and solid guide throughout my doctoral years, and for his support during times of intense and rigorous scientific work. His dedication in research and his teachings are a source of deep inspiration to me.

Moreover, I am very grateful to Dr. Brendon Lovett for all the stimulating discussions at the group meetings that contributed to my progress throughout my PhD. I wish to thank Profs. Andrew Daley and Benjamin Lev for their helpful advices to my research projects and for their kind hospitality when I visited the Physics departments in Glasgow and Stanford. I am grateful for being part of an international collaboration involving Ben Lev's group, and I would particularly like to thank Brendan Marsh for his valuable help in the development of the project discussed in chapter 4 and his kindness. This experience made me realise the importance of the feedback between theory and experiments, and how one positively influences the other.

As a PhD candidate within the Scottish Doctoral Training Centre in Condensed Matter Physics (CM-CDT), a special acknowledgement goes to the CM-CDT for the generous financial support (Grant number: EP/L015110/1) and, in particular, to Dr. Chris Hooley, Julie Massey, and Debra Thompson for managing a successful and vibrant network of researchers.

I greatly enjoyed the opportunities to present my work at conferences and academic visits, which contributed to shaping the next steps in my research. In this regard, I remember with pleasure the time spent discussing science and our respective projects, and exploring California with Drs. François Damanet and Araceli Venegas-Gomez, thank you for that

great adventure! I wish to thank particularly François for his interest and advices while I was working on my first research project.
I am equally grateful to Kristín and all fellow PhD students in the CM-CDT group at the University of St. Andrews, Carolina, Dom, Kaycee and Dom, Cheng, James and Gerald for being part of a stimulating and fun environment. I am grateful for the nice time spent together in St. Andrews.
I wish to thank all my professors at the University of Palermo, in particular Profs. Roberto Passante, Lucia Rizzuto and Antonino Messina for shaping the person I am today.
From the personal side, I wish to express gratitude to my flatmates Michela and Matthew for all the fun nights watching Marvel movies. A special acknowledgement goes to my long-standing colleagues and friends in Palermo, in particular, Enza, Domenico, little Sofia and Leo for all their affection and support. I wish to finally thank Nicolò and Simona in Edinburgh, for their friendship during these years and all the wonderful times spent exploring Edinburgh.
Finally, I wish to dedicate this work to my brother Valerio, my parents, and Giuseppe, to whom goes my deepest gratitude, for their infinite support, patience and love they always demonstrated.

Bibliography

[1] R. H. Dicke. Coherence in spontaneous radiation processes. *Phys. Rev.* **93**, 99–110, Jan 1954.

[2] M. Gross and S. Haroche. Superradiance: An essay on the theory of collective spontaneous emission. *Phys. Rep.* **93**, 301–396, 1982.

[3] K. Hepp and E. H. Lieb. On the superradiant phase transition for molecules in a quantized radiation field: the Dicke maser model. *Ann. Phys.* **76**, 360 – 404, 1973.

[4] HJ Carmichael, CW Gardiner, and DF Walls. Higher order corrections to the dicke superradiant phase transition. *Phys. Lett. A* **46**, 47–48, 1973.

[5] Y. K. Wang and F.T. Hioe. Phase transition in the dicke model of superradiance. *Phys. Rev. A* **7**, 831, 1973.

[6] N. Lambert, C. Emary, and T. Brandes. Entanglement and the phase transition in single-mode superradiance. *Phys. Rev. Lett.* **92**, 073602, 2004.

[7] K Rzażewski, Kand Wódkiewicz, and W Żakowicz. Phase transitions, two-level atoms, and the a 2 term. *Phys. Rev. Lett.* **35**, 432, 1975.

[8] JM Knight, Y Aharonov, and GTC Hsieh. Are super-radiant phase transitions possible? *Phys. Rev. A* **17**, 1454, 1978.

[9] I. Bialynicki-Birula and K. Rzażewski. No-go theorem concerning the superradiant phase transition in atomic systems. *Phys. Rev. A* **19**, 301, 1979.

[10] P. Nataf and C. Ciuti. No-go theorem for superradiant quantum phase transitions in cavity qed and counter-example in circuit qed. *Nat. commun.* **1**, 1–6, 2010.

[11] A. Vukics and P. Domokos. Adequacy of the dicke model in cavity qed: A counter-no-go statement. *Phys. Rev. A* **86**, 053807, 2012.

[12] O. Viehmann, J. von Delft, and F. Marquardt. Superradiant phase transitions and the standard description of circuit qed. *Phys. rev. Lett.* **107**, 113602, 2011.

[13] VM Bastidas, C Emary, B Regler, and T Brandes. Nonequilibrium quantum phase transitions in the dicke model. *Phys. Rev. Lett.* **108**, 043003, 2012.

[14] F. Dimer, B. Estienne, A. S. Parkins, and H. J. Carmichael. Proposed realization of the Dicke-model quantum phase transition in an optical cavity QED system. *Phys. Rev. A* **75**, 013804, Jan 2007.

[15] K. Baumann, C. Guerlin, F. Brennecke, and T. Esslinger. Dicke quantum phase transition with a superfluid gas in an optical cavity. *Nature* **464**, 1301–1306, 2010.

[16] P. Kirton, M. M. Roses, J. Keeling, and E. G. Dalla Torre. Introduction to the Dicke Model: From Equilibrium to Nonequilibrium, and Vice Versa. *Adv. Quantum Technol.* **2**, 1800043, 2019.

[17] R. I. Moodie, K. E. Ballantine, and J. Keeling. Generalized classes of continuous symmetries in two-mode Dicke models. *Phys. Rev. A* **97**, 033802, Mar 2018.

[18] G. Lindblad. On the generators of quantum dynamical semigroups. *Commun. Math. Phys.* **48**, 119–130, 1976.

[19] H.-P. Breuer and F Petruccione. *The Theory of Open Quantum Systems*. Oxford University Press, Oxford, 2002.

[20] P. Kirton and J. Keeling. Suppressing and restoring the Dicke superradiance transition by dephasing and decay. *Phys. Rev. Lett.* **118**, 123602, mar 2017.

[21] P. Kirton and J. Keeling. Superradiant and lasing states in driven-dissipative dicke models. *New J. Phys.* **20**, 015009, 2018.

[22] K. B. Arnardottir, A. J. Moilanen, A. Strashko, P. Törmä, and J. Keeling. Multimode organic polariton lasing. *Phys. Rev. Lett.* **125**, 233603, 2020.

[23] J. Léonard, A. Morales, P. Zupancic, T. Esslinger, and T. Donner. Supersolid formation in a quantum gas breaking a continuous translational symmetry. *Nature* **543**, 87–90, mar 2017.

[24] L. Zou, D. Marcos, S. Diehl, S. Putz, J. Schmiedmayer, J. Majer, and P. Rabl. Implementation of the Dicke lattice model in hybrid quantum system arrays. *Phys. Rev. Lett.* **113**, 023603, 2014.

[25] S. Putz, D. O. Krimer, R. Amsuess, A. Valookaran, T. Noebauer, J. Schmiedmayer, S. Rotter, and J. Majer. Protecting a spin ensemble against decoherence in the strong-coupling regime of cavity QED. *Nat. Phys.* **10**, 720–724, 2014.

[26] A. Angerer, K. Streltsov, T. Astner, S. Putz, H. Sumiya, S. Onoda, J. Isoya, W. J. Munro, K. Nemoto, J. Schmiedmayer, et al. Superradiant emission from colour centres in diamond. *Nat. Phys.* **14**, 1168–1172, 2018.

[27] P Rabl, D DeMille, John M Doyle, Mikhail D Lukin, RJ Schoelkopf, and P Zoller. Hybrid quantum processors: molecular ensembles as quantum memory for solid state circuits. *Phys. Rev. Lett.* **97**, 033003, 2006.

[28] S. Genway, W. Li, C. Ates, B. P. Lanyon, and I. Lesanovsky. Generalized Dicke nonequilibrium dynamics in trapped ions. *Phys. Rev. Lett.* **112**, 023603, 2014.

[29] A. Safavi-Naini, R. Lewis-Swan, J. G. Bohnet, M. Gärttner, K. A. Gilmore, J. E. Jordan, J. Cohn, J. K. Freericks, A. M. Rey, and J. J. Bollinger. Verification of a many-ion simulator of the Dicke model through slow quenches across a phase transition. *Phys. Rev. Lett.* **121**, 040503, 2018.

[30] P. Nataf, A. Baksic, and C. Ciuti. Double symmetry breaking and two-dimensional quantum phase diagram in spin-boson systems. *Phys. Rev. A* **86**, 013832, 2012.

[31] A. A. Houck, H. E. Türeci, and J. Koch. On-chip quantum simulation with superconducting circuits. *Nat. Phys.* **8**, 292–299, 2012.

[32] A. Baksic and C. Ciuti. Controlling discrete and continuous symmetries in "superradiant" phase transitions with circuit qed systems. *Phys. Rev. Lett.* **112**, 173601, Apr 2014.

[33] N. Lambert, Y. Matsuzaki, K. Kakuyanagi, N. Ishida, S. Saito, and F. Nori. Superradiance with an ensemble of superconducting flux qubits. *Phys. Rev. B* **94**, 224510, 2016.

[34] M. Bamba, K. Inomata, and Y. Nakamura. Superradiant phase transition in a superconducting circuit in thermal equilibrium. *Phys. Rev. Lett.* **117**, 173601, 2016.

[35] J. Keeling and S. Kéna-Cohen. Bose–Einstein Condensation of Exciton-Polaritons in Organic Microcavities. *Ann. Rev. Phys. Chem.* **71**, 435–459, 2020.

[36] S. L. Cornish and D. Cassettari. Recent progress in bose-einstein condensation experiments. *Philos. Trans. Royal Soc. A PHILOS T R SOC A* **361**, 2699–2713, 2003.

[37] M. Kulkarni, B. Öztop, and H. E. Türeci. Cavity-mediated near-critical dissipative dynamics of a driven condensate. *Phys. Rev. Lett.* **111**, 220408, 2013.

[38] C. Maschler, I. B. Mekhov, and H. Ritsch. Ultracold atoms in optical lattices generated by quantized light fields. *Eur. Phys. J. D* **46**, 545–560, 2008.

[39] F. Mivehvar, F. Piazza, T. Donner, and H. Ritsch. Cavity qed with quantum gases: New paradigms in many-body physics. *Adv. Phys.* 70, 2021.

[40] F. Dalfovo, S. Giorgini, L. P. Pitaevskii, and S. Stringari. Theory of bose-einstein condensation in trapped gases. *Rev. Mod. Phys.* **71**, 463, 1999.

[41] K. Baumann, R. Mottl, F. Brennecke, and T. Esslinger. Exploring Symmetry Breaking at the Dicke Quantum Phase Transition. *Phys. Rev. Lett.* **107**, 140402, 2011.

[42] J. Léonard, A. Morales, P. Zupancic, T. Donner, and T. Esslinger. Monitoring and manipulating higgs and goldstone modes in a supersolid quantum gas. *Science* **358**, 1415–1418, 2017.

[43] S. Gopalakrishnan, Y. E Shchadilova, and E. Demler. Intertwined and vestigial order with ultracold atoms in multiple cavity modes. *Phys. Rev. A* **96**, 063828, 2017.

[44] K. Hepp and E. H. Lieb. Equilibrium statistical mechanics of matter interacting with the quantized radiation field. *Phys. Rev. A* **8**, 2517–2525, Nov 1973.

[45] D. Jaksch, C. Bruder, J. I. Cirac, C. W. Gardiner, and P. Zoller. Cold bosonic atoms in optical lattices. *Phys. Rev. Lett.* **81**, 3108, 1998.

[46] N. Dogra, F. Brennecke, S. D. Huber, and T. Donner. Phase transitions in a bose-hubbard model with cavity-mediated global-range interactions. *Phys. Rev. A* **94**, 023632, 2016.

[47] Y. Chen, Z Yu, and H. Zhai. Quantum phase transitions of the bose-hubbard model inside a cavity. *Phys. Rev. A* **93**, 041601, 2016.

[48] E. R. Chiacchio and A. Nunnenkamp. Tuning the relaxation dynamics of ultracold atoms in a lattice with an optical cavity. *Phys. Rev. A* **97**, 033618, 2018.

[49] D. Nagy, G. Kónya, P. Domokos, and G. Szirmai. Quantum noise in a transversely-pumped-cavity bose-hubbard model. *Phys. Rev. A* **97**, 063602, 2018.

[50] F. Mivehvar, F. Piazza, and H. Ritsch. Disorder-driven density and spin self-ordering of a bose-einstein condensate in a cavity. *Phys. Rev. Lett.* **119**, 063602, 2017.

[51] S. Safaei, Ö. E. Müstecaplıoğlu, and B. Tanatar. Raman superradiance and spin lattice of ultracold atoms in optical cavities. *New J. Phys.* **15**, 083037, 2013.

[52] F. Mivehvar, H. Ritsch, and F. Piazza. Cavity-quantum-electrodynamical toolbox for quantum magnetism. *Phys. Rev. Lett.* **122**, 113603, 2019.

[53] R. M. Kroeze, Y. Guo, V. D. Vaidya, J. Keeling, and B. L. Lev. Spinor self-ordering of a quantum gas in a cavity. *Phys. Rev. Lett.* **121**, 163601, Oct 2018.

[54] E Colella, R Citro, M Barsanti, D Rossini, and M-L Chiofalo. Quantum phases of spinful fermi gases in optical cavities. *Phys. Rev. B* **97**, 134502, 2018.

[55] E. Colella, S. Ostermann, W. Niedenzu, F. Mivehvar, and H. Ritsch. Antiferromagnetic self-ordering of a fermi gas in a ring cavity. *New J. Phys.* **21**, 043019, 2019.

[56] S. Ostermann, H-W Lau, H. Ritsch, and F. Mivehvar. Cavity-induced emergent topological spin textures in a bose–einstein condensate. *New J. Phys.* **21**, 013029, 2019.

[57] S. Gopalakrishnan, B. L. Lev, and P. M. Goldbart. Frustration and glassiness in spin models with cavity-mediated interactions. *Phys. Rev. Lett.* **107**, 277201, 2011.

[58] J. Fan, Z. Yang, Y. Zhang, J. Ma, G. Chen, and S. Jia. Hidden continuous symmetry and nambu-goldstone mode in a two-mode dicke model. *Phys. Rev. A* **89**, 023812, Feb 2014.

[59] S. Gopalakrishnan, B. L. Lev, and P. M. Goldbart. Emergent crystallinity and frustration with bose–einstein condensates in multimode cavities. *Nat. Phys.* **5**, 845–850, 2009.

[60] S. Gopalakrishnan, B. L. Lev, and P. M. Goldbart. Atom-light crystallization of Bose-Einstein condensates in multimode cavities: Nonequilibrium classical and quantum phase transitions, emergent lattices, supersolidity, and frustration. *Phys. Rev. A* **82**, 043612, 2010.

[61] A. J. Kollár, A. T. Papageorge, K. Baumann, M. A. Armen, and B. L. Lev. An adjustable-length cavity and bose–einstein condensate apparatus for multimode cavity qed. *New J. Phys.* **17**, 043012, 2015.

[62] K. E. Ballantine, B. L. Lev, and J. Keeling. Meissner-like effect for a synthetic gauge field in multimode cavity qed. *Phys. Rev. Lett.* **118**, 045302, Jan 2017.

[63] V. D. Vaidya, Y. Guo, R. M. Kroeze, K. E. Ballantine, A. J. Kollár, J. Keeling, and B. L. Lev. Tunable-range, photon-mediated atomic interactions in multimode cavity qed. *Phys. Rev. X* **8**, 011002, Jan 2018.

[64] B. P. Marsh, Y. Guo, R. M. Kroeze, S. Gopalakrishnan, S. Ganguli, J. Keeling, and B. L. Lev. Enhancing associative memory recall and storage capacity using confocal cavity qed. *Phys. Rev. X* **11**, 021048, 2021.

[65] A. E. Siegman. *Lasers*. University Science Books, 1986.

[66] F. R. Karl. *Basics of Laser Physics For Students of Science and Engineering*. Spinger, 2017.

[67] S. Haroche and J-M Raimond. *Exploring the quantum: atoms, cavities, and photons*. Oxford university press, 2006.

[68] A. J. Kollár, A. T. Papageorge, V. D. Vaidya, Y. Guo, J. Keeling, and B. L. Lev. Supermode-density-wave-polariton condensation with a Bose-Einstein condensate in a multimode cavity. *Nat. Commun.* **8**, 14386, jun 2017.

[69] J. J. Hopfield. Neural networks and physical systems with emergent collective computational abilities. *Proc. Natl. Acad. Sci.* **79**, 2554, 1982.

[70] J. J. Hopfield and D. W. Tank. Computing with neural circuits: A model. *Science* **233**, 625–633, 1986.

[71] Y. Nakamura, K. Torii, and T. Munakata. Neural-network model composed of multidimensional spin neurons. *Phys. Rev. E* **51**, 1538–1546, 1995.

[72] F. Barahona. On the computational complexity of ising spin glass models. *J. Phys. A Math. Theor.* **15**, 3241, 1982.

[73] H. Sompolinsky et al. Statistical mechanics of neural networks. *Phys. Today* **41**, 70–80, 1988.

[74] D. L. Stein and C. M. Newman. *Spin glasses and complexity*, volume 4. Princeton University Press, Princeton, 2013.

[75] J. Hertz, A. Krogh, and R. G. Palmer. *Introduction to the theory of neural computation*. CRC Press, 2018.

[76] K. H. Fischer and J. A. Hertz. *Spin glasses*. Cambridge University Press, Cambridge, 1991.

[77] S. Gopalakrishnan, B. L. Lev, and P. M. Goldbart. Exploring models of associative memory via cavity quantum electrodynamics. *Phil. Mag.* **92**, 353–361, 2012.

[78] P. Rotondo, M. Cosentino Lagomarsino, and G. Viola. Dicke simulators with emergent collective quantum computational abilities. *Phys. Rev. Lett.* **114**, 143601, 2015.

[79] V. Torggler, S. Krämer, and H. Ritsch. Quantum annealing with ultracold atoms in a multimode optical resonator. *Phys. Rev. A* **95**, 032310, 2017.

[80] P. Rotondo, M. Marcuzzi, J. P. Garrahan, I. Lesanovsky, and M. Müller. Open quantum generalisation of hopfield neural networks. *J. Phys. A: Math. Theor.* **51**, 115301, 2018.

[81] E. Fiorelli, M. Marcuzzi, P. Rotondo, F. Carollo, and I. Lesanovsky. Signatures of associative memory behavior in a multimode dicke model. *Phys. Rev. Lett.* **125**, 070604, Aug 2020.

[82] D. J. Amit, H. Gutfreund, and H. Sompolinsky. Storing infinite numbers of patterns in a spin-glass model of neural networks. *Phys. Rev. Lett.* **55**, 1530, 1985.

[83] V. Gorini, A. Kossakowski, and E. C. G. Sudarshan. Completely positive dynamical semigroups of n-level systems. *J. Math. Phys.* **17**, 821–825, 1976.

[84] D. F. Walls and G. J. Milburn. *Quantum optics*. Springer Science & Business Media, 2007.

[85] TM Stace, SD Barrett, HS Goan, and GJ Milburn. Parity measurement of one-and two-electron double well systems. *Phys. Rev. B* **70**, 205342, 2004.

[86] SD Barrett and TM Stace. Continuous measurement of a microwave-driven solid state qubit. *Phys. Rev. Lett.* **96**, 017405, 2006.

[87] A. Kolli, B. W. Lovett, S. C. Benjamin, and T. M. Stace. All-optical measurement-based quantum-information processing in quantum dots. *Phys. Rev. Lett.* **97**, 250504, 2006.

[88] S. D. Barrett and T. M. Stace. Two-spin measurements in exchange interaction quantum computers. *Phys. Rev. B* **73**, 075324, 2006.

[89] A. Purkayastha, A. Dhar, and M. Kulkarni. Out-of-equilibrium open quantum systems: A comparison of approximate quantum master equation approaches with exact results. *Phys. Rev. A* **93**, 062114, 2016.

[90] A. G. Redfield. On the Theory of Relaxation Processes. *IBM J. Res. Dev.* **1**, 19–31, jan 1957.

[91] F. Damanet, A. J. Daley, and J. Keeling. Atom-only descriptions of the driven-dissipative Dicke model. *Phys. Rev. A* **99**, 033845, Mar 2019.

[92] J. Jeske, D. Ing, M. B. Plenio, S. F. Huelga, and J. H. Cole. Bloch-Redfield equations for modeling light-harvesting complexes. *J. Chem. Phys* **142**, 064104, aug 2015.

[93] P. R. Eastham, P. Kirton, H. M. Cammack, B. W. Lovett, and J. Keeling. Bath-induced coherence and the secular approximation. *Phys. Rev. A* **94**, 012110, Jul 2016.

[94] H. M. Cammack, P. Kirton, T. M. Stace, P. R. Eastham, J. Keeling, and B. W. Lovett. Coherence protection in coupled quantum systems. *Phys. Rev. A* **97**, 022103, Feb 2018.

[95] A. Dodin, T. Tscherbul, R. Alicki, A. Vutha, and P. Brumer. Secular versus nonsecular Redfield dynamics and Fano coherences in incoherent excitation: An experimental proposal. *Phys. Rev. A* **97**, 013421, 2018.

[96] R. Hartmann and W. T. Strunz. Accuracy assessment of perturbative master equations: Embracing nonpositivity. *Phys. Rev. A* **101**, 012103, Jan 2020.

[97] R. Dümcke and H Spohn. The proper form of the generator in the weak coupling limit. *Z. Physik B* **34**, 419–422, dec 1979.

[98] R. Palacino and J. Keeling. Atom-only theories for u (1) symmetric cavity-qed models. *Phys. Rev. Research* **3**, L032016, 2021.

[99] C. Müller and T. M. Stace. Deriving Lindblad master equations with Keldysh diagrams: Correlated gain and loss in higher order perturbation theory. *Phys. Rev. A* **95**, 013847, Jan 2017.

[100] L. V. Keldysh et al. Diagram technique for nonequilibrium processes. *Sov. Phys. JETP* **20**, 1018–1026, 1965.

[101] B. K. Agarwalla, M. Kulkarni, S. Mukamel, and D. Segal. Tunable photonic cavity coupled to a voltage-biased double quantum dot system: Diagrammatic nonequilibrium green's function approach. *Phys. Rev. B* **94**, 035434, 2016.

[102] H. Schoeller and G. Schön. Mesoscopic quantum transport: Resonant tunneling in the presence of a strong coulomb interaction. *Phys. Rev. B* **50**, 18436, 1994.

[103] M. Marthaler, Y. Utsumi, and D. S. Golubev. Lasing in circuit quantum electrodynamics with strong noise. *Phys. Rev. B* **91**, 184515, 2015.

[104] Y. Makhlin, G. Schön, and A. Shnirman. Dissipation in josephson qubits. In *New Directions in Mesoscopic Physics (Towards Nanoscience)*, pages 197–224. Springer, 2003.

[105] E. G. Dalla Torre, S. Diehl, M. D. Lukin, S. Sachdev, and P. Strack. Keldysh approach for nonequilibrium phase transitions in quantum optics: Beyond the dicke model in optical cavities. *Phys. Rev. A* **87**, 023831, 2013.

[106] P. Schad, B. N. Narozhny, G. Schön, and A. Shnirman. Nonequilibrium spin noise and noise of susceptibility. *Phys. Rev. B* **90**, 205419, 2014.

[107] M. Marthaler and J. Leppäkangas. Diagrammatic description of a system coupled strongly to a bosonic bath. *Phys. Rev. B* **94**, 144301, 2016.

[108] G-C Wick. The evaluation of the collision matrix. *Phys. Rev.* **80**, 268, 1950.

[109] F. Minganti, A. Biella, N. Bartolo, and C. Ciuti. Spectral theory of Liouvillians for dissipative phase transitions. *Phys. Rev. A* **98**, 042118, Oct 2018.

[110] N. Bartolo, F. Minganti, W. Casteels, and C. Ciuti. Exact steady state of a kerr resonator with one-and two-photon driving and dissipation: Controllable wigner-function multimodality and dissipative phase transitions. *Phys. Rev. A* **94**, 033841, 2016.

[111] F. Minganti, A. Miranowicz, R. W. Chhajlany, and F. Nori. Quantum exceptional points of non-hermitian hamiltonians and liouvillians: The effects of quantum jumps. *Phys. Rev. A* **100**, 062131, 2019.

[112] D. Huybrechts, F. Minganti, F. Nori, M. Wouters, and N. Shammah. Validity of mean-field theory in a dissipative critical system: Liouvillian gap, pt-symmetric antigap, and permutational symmetry in the xyz model. *Phys. Rev. B* **101**, 214302, 2020.

[113] F. Minganti, I. Arkhipov, A. Miranowicz, and F. Nori. Continuous dissipative phase transitions with or without symmetry breaking. *New J. Phys.* , 2021.

[114] LD Landau and EM Lifshitz. *Statistical Physics*, volume 5 of *Theoretical Physics*. Butterworth-Heinemann, Oxford, 1980.

[115] P.M. Chaikin and T.C. Lubensky. *Principles of Condensed Matter Physics*. Cambridge University Press, Cambridge, 1995.

[116] S. Sachdev. *Quantum phase transitions*. Cambridge university press, 2011.

[117] H. J. Carmichael. *Statistical methods in quantum optics 1: master equations and Fokker-Planck equations*, volume 1. Springer Science & Business Media, 1999.

[118] C. Gardiner and P. Zoller. *Quantum noise: a handbook of Markovian and non-Markovian quantum stochastic methods with applications to quantum optics*. Springer, Berlin, 2004.

[119] A. Rivas and S. F. Huelga. Quantum markov process: Mathematical structure. In *Open Quantum Systems*, pages 33–48. Springer, 2012.

[120] R Graham and H Haken. Laserlight—first example of a second-order phase transition far away from thermal equilibrium. *Zeitschrift für Physik* **237**, 31–46, 1970.

[121] P. R. Rice and H. Carmichael. Photon statistics of a cavity-qed laser: A comment on the laser–phase-transition analogy. *Phys. Rev. A* **50**, 4318, 1994.

[122] I. Carusotto and C. Ciuti. Quantum fluids of light. *Rev. Mod. Phys.* **85**, 299–366, Feb 2013.

[123] H. J. Eichler, J. Eichler, and O. Lux. *Lasers: basics, advances and applications*, volume 220. Springer, 2018.

[124] E. M. Kessler, G. Giedke, A. Imamoglu, S. F. Yelin, M. D. Lukin, and J. I. Cirac. Dissipative phase transition in a central spin system. *Phys. Rev. A* **86**, 012116, 2012.

[125] B. Horstmann, J. I. Cirac, and G. Giedke. Noise-driven dynamics and phase transitions in fermionic systems. *Phys. Rev. A* **87**, 012108, 2013.

[126] F. Piazza, P. Strack, and W. Zwerger. Bose–einstein condensation versus dicke–hepp–lieb transition in an optical cavity. *Ann. Phys.* **339**, 135–159, 2013.

[127] E. G. Dalla Torre, Y. Shchadilova, E. Y. Wilner, M. D. Lukin, and E. Demler. Dicke phase transition without total spin conservation. *Phys. Rev. A* **94**, 061802, 2016.

[128] J. Lang and F. Piazza. Critical relaxation with overdamped quasiparticles in open quantum systems. *Phys. Rev. A* **94**, 033628, 2016.

[129] R. Kubo. Generalized cumulant expansion method. *J. Phys. Soc. Japan* **17**, 1100–1120, 1962.

[130] M. Kira and S. W. Koch. Cluster-expansion representation in quantum optics. *Phys. Rev. A* **78**, 022102, 2008.

[131] C. Gardiner. *Stochastic methods*. Springer, Berlin, 2009.

[132] M. Kira and S. W. Koch. *Semiconductor quantum optics*. Cambridge University Press, 2011.

[133] M. O. Scully and M. S. Zubairy. Quantum optics, 1999.

[134] H. J. Metcalf and P. van der Straten. Laser cooling and trapping of atoms. *JOSA B* **20**, 887–908, 2003.

[135] M. Sánchez-Barquilla, R. E. F. Silva, and J. Feist. Cumulant expansion for the treatment of light–matter interactions in arbitrary material structures. *J. Chem. Phys.* **152**, 034108, 2020.

[136] J. Jeske, D. Ing, M. B. Plenio, S. F. Huelga, and J. H. Cole. Bloch-Redfield equations for modeling light-harvesting complexes. *J. Chem. Phys* **142**, 064104, aug 2015.

[137] O. Chang. *Goldstone modes and symmetry breaking in open quantum systems*. M. Sc. Thesis, University of St Andrews, 2021.